MULTI-AXIS ESPI INTERFEROMETER FOR 3-D DISPLACEMENT MEASUREMENTS

by

Filipe Zanini Broetto

B.E., Universidade Federal de Santa Catarina, 2015

A THESIS SUBMITTED IN PARTIAL FULFILLMENT OF

THE REQUIREMENTS FOR THE DEGREE OF

MASTER OF APPLIED SCIENCES

in

THE FACULTY OF GRADUATE AND POSTDOCTORAL STUDIES

(Mechanical Engineering)

THE UNIVERSITY OF BRITISH COLUMBIA

(Vancouver)

December 2017

Abstract

Small displacement measurements have several applications in engineering. Deformations ranging from nanometric scale to micrometric scale are very often related to mechanical stresses, materials phase transformations, residual stresses, biological processes, etc. It is common that these deformations occur in three dimensions and are not easily measured with simple equipment. Electronic speckle pattern interferometry (ESPI) systems use interference of light and laser properties to measure such small displacements in a very reliable way. The ESPI technique is a full-field non-contact technique capable of 3D measurements but the arrangement can get very complicated when it comes to number of components, size, cost, assembly complexity and operation. Among the many factors contributing for the complexity, the most important ones are the number of light beams and optical elements, and the laser itself. High quality lasers offer very high coherence – which is a measure of purity of spectrum and therefore allow for very high quality measurements with very low noise – at a very high cost, and usually are bulky, requiring many extra components to split light beams and direct the light to the region of interest. The aim of this project is to use special components to eliminate the need for an expensive laser and simplify the arrangement for a 3D ESPI measurement. The introduction of a dual diffraction grating system makes it possible to replace a high quality laser with a low coherence, compact and cheap laser diode. Moreover, with this new proposed arrangement it is possible to obtain the 3D ESPI information using two in-plane ESPI systems combined in one, reducing complexity and offering up to 6 different measurement possibilities. Based on the fact that only 3 different measurements are required for solving a complete 3D displacement field, the remaining measurements can be used for data averaging and to increase the accuracy and reduce uncertainties. The new design is presented and a portable device is developed. The arrangement is explored to test the robustness against exterior factors such as temperature and ambient light, and the accuracy of the measurement is verified with a controlled sample and finite element analysis/analytical solutions.

Lay Summary

The measurement of displacements in the nanometric to micrometric range is of large importance in engineering. The applications range from mechanical design, material characterization, calibration of microelectromechanical systems (MEMS) to residual stress measurement. In real applications, these displacements occur in three dimensions, and special techniques are used to quantify the complete displacement field. Electronic Speckle Pattern Interferometry (ESPI) is a noncontact and full-field optical technique that uses laser light to measure small surface deformations. While the technique allows the three-dimensional measurement, the typical arrangement used in ESPI systems for this purpose is complicated, using large number of components and sophisticated lasers. A simplified arrangement is proposed in this work. The use of a laser diode and a diffraction grating system reduces the complexity while allowing the measurement of the out-of-plane displacement component by combining two simple in-plane arrangement in different ways.

Preface

This work was first proposed by Dr. Gary Schajer and was conducted at the Renewable Resources Laboratory, in the Mechanical Engineering Department at the University of British Columbia, Vancouver Campus. I developed the concept further and conducted all the steps of this project, including theoretical analysis, equipment design and construction, testing and results validation.

I developed the conceptual design and fabricated most of the components in the student machine shop in the Mechanical Engineering Department. The work was executed by me with aid of Electronics Technician Glenn Jolly and summer Student Charles Karassowitsch.

The final manuscript was written by me with supervision of Dr. Gary Schajer.

Table of Contents

List of Tables

List of Figures

List of Symbols

ω – Angular frequency

$[D_a]$ – Applied displacement matrix

$\overline{d_m}$ – Averaged displacement from multiple measurements

A_a – Average intensity after deformation

A_b – Average intensity before deformation

H – Coherence interval

Δl_c – Coherence length

τ_c – Coherence time

$K_{3\rightarrow 6}$ – Combined sensitivity vectors 3 to 6

γ_{max} – Contrast of interference pattern

d_a – Displacement applied by loading mechanism

d_m – Displacement at the measured region due to sample rotation

u – Displacement component in the X direction

v – Displacement component in the Y direction

w – Displacement component in the Z direction

d_x – Displacement field in X

d_y – Displacement field in Y

d_z – Displacement field in Z

$\{d_i\}$ – Displacement filed vector

L_i – Distance from load application point to measurement region

p – Diffraction grating line spacing

e_x – Efficiency of grating g_x

e_y – Efficiency of grating g_y

E_0 – Electric field amplitude

E – Electric field wave equation

$\tilde{E}$ – Electric field wave complex amplitude

$\vec{E}$ – Electric field wave in complex notation

f_2 – Focal length of convergent lens

f_1 – Focal length of divergent lens

$\Delta\nu$ – Free spectral range

f – Frequency

δ_p – Grating displacement for phase shift

g_x – Grating for the X direction

g_y – Grating for the Y direction

θ_i – Incidence angle of beam i

$I_{dif_{g_x g_y}}$ – Intensity diffracted through g_x and g_y

$I_{dif_{g_x}}$ – Intensity of diffracted beams in g_x

$I_{dif_{g_y}}$ – Intensity of diffracted beams in g_y

I_i – Intensity of i^{th} image in four-step method

$I_{t_{g_x}}$ – Intensity transmitted through g_x

$I_{t_{g_y}}$ – Intensity transmitted through g_y

B_a – Interference term amplitude after deformation

B_b – Interference term amplitude before deformation

$\overline{\Delta\lambda}$ – Laser spectrum bandwidth

$[Q]$ – Least Squares matrix

$\Delta\lambda$ – Longitudinal mode spacing

h -Measurement area width

I_{max} – Maximum intensity of interference

L_m – Measurement region length

$\{\Delta\Theta_m\}$ – Measured phase vector

I_{min} – Minimum intensity of interference

N_f – Number of complete wavelength rigid body displacements

$\mathrm{N_p}$ – Number of pixels

m – Order of diffraction

Θ – Phase difference from two interfering beams

ϕ – Phase of light wave

r – Position vector

δ_i – Path length difference

δ_{pl} – Path length difference across measurement area

$\Delta\Theta$ – Phase difference due to deformation

$\Delta\phi$ – Phase shift due to grating translation

P_s – Pixel size

ϑ – Relative incidence angle of time fronts

$\{K_r\}$ – Residual sensitivity vector

α – Rotation angle

K_x – Sensitivity in X direction

K_y – Sensitivity in Y direction

$[K_m]$ – Sensitivity matrix

K – Sensitivity vector

c – Speed of light in vacuum

e – Total efficiency of grating system

$\overline{\Delta d_m}$ – Uncertainty for the average

Δd_a – Uncertainty on displacement applied

Δd_m – Uncertainty on displacement at the measurement area

ΔL_m – Uncertainty on measurement area length

Δh - Uncertainty on measurement region width

ΔN_p – Uncertainty on number of pixels

ΔP_s – Uncertainty on pixel size

$\hat{x}$ – Unity vector in the X direction

$\hat{y}$ – Unity vector in the Y direction

$\hat{z}$ – Unity vector in the Z direction

V – Visibility ratio

λ – wavelength

T – Wave period

k_x – Wave vector component in the X direction

k_y – Wave vector component in the Y direction

k_z – Wave vector component in the Z direction

List of Abbreviations

CCD – Charged Coupled Device

CMOS – Complementary Metal-Oxide Semiconductor

ESPI – Electronic Speckle Pattern Interferometry

FEA – Finite Element Analysis

PZT – Piezoelectric Transducer

3-D – Three-Dimensional

Acknowledgements

First, I'd like to express my sincere gratitude to my Supervisor – Dr. Gary Schajer – for always being there with his guidance, support and encouragement. Much more than a supervisor, he acted as my dearest friend throughout my stay in Vancouver. His support was not limited to laboratory and research matters, but was also essential to my well-being and happiness while at UBC. He's always taken care of his students as if they're his own children, and I sure consider him as a father. My Sincere thanks, Dr. Schajer, for all you've done for me. I would not have been able to achieve all I achieved without your support!

I'd like to give very special thanks to American Stress Technologies for all the funding support provided for this project and for the Renewable Resources Laboratory.

I want to express my gratitude to the examination committee, Dr. Kirk Madison and Dr. Boris Stoeber, for their patience and comprehension. Their constructive questions and commentaries were very welcome and appreciated.

Also, I'd like to give very special thanks to all my laboratory colleagues: Juuso Heikinnen, Patrick Pan, Harsh Pokarna, Ilan Roetenberg, Noushi Roushi, Anna Tang and Alan Walsh, for all their support and important/creative ideas.

Moreover, I'd like to thank all my friends: Miguel Villalba, Adriana Cabrera, Rodrigo Costa, Marco Galaviz, Cristina Horta, Brenda D'acunha, Claire Gregoire, Manav, Faisal Al-qurooni, Ratul Daz, Alondra Renteria, Kui Pan, Mehretab Getachew Tadesse, Pablo Lacerda Silva, Mike El-Koussefi, Somesh Bathia, Sarah Crosby, for always being here for me, for the good company and for making the experience in Vancouver something I'll never forget.

Special thanks for Glen Jolly for all his support on Electronics and for the very interesting conversations. To Charles Karassowitsch, thanks for your good ideas and support in the making of the equipment!

The most special thanks to my girlfriend Gabriela Nunes Abrantes, the love of my life. Thanks for always being there for me. I know how difficult it has been to you, through almost two and half years, to stand still and keep our relationship alive. I will never forget what you have done for me, all the sacrifice you’ve made and I promise I will compensate all this time that we’ve spent far from each other. My most sincere thanks for being this spectacular person, and for never giving up on me.

Finally, to my parents, Romeu and Vanda. I would not be writing this if it wasn’t for all your sacrifice. You gave me everything I have. My character, I owe to you both! My education, my values, everything, I owe everything to you! Thank you for always supporting me on my decisions, and I hope I’ve made you proud!

Dedication

To my parents, my girlfriend and my friends.

Chapter 1: Introduction

1.1 Displacement measurement and related techniques

Measurement of small displacements is of great importance in many engineering applications. These small displacements fall in the nanometer to micrometer range and demand high precision systems for accurate measurement. Applications that require such displacement measurements are usually found in material testing and characterization [1], residual stress measurement [2][3] and failure identification and investigation [4]. Further applications can be found in design and product development [5] and calibration and testing of microelectromechanical systems (MEMS) [6]. Recently, new applications are also found in the biological field as in characterization of biomechanical components and materials [7] and biological tissue [8] among several others.

The methods used for measuring small deformations are divided into contact and non-contact methods. Furthermore, they can be classified as local or full-field methods, using a wide range of measurement principles. When selecting a method for a specific application such as static or dynamic measurements, there are several important aspects to be considered. Among important factors are accuracy, measurement range and sensitivity, robustness and preparation time.

Other strain measurement techniques such as photoelasticity [9] and bonded wire strain gages [10] have their particular applications. The use of photoelasticity is restricted to optically transparent models while strain gages provide only local measurements and the preparation time is long. Developments in optical techniques such as Geometric Moiré [11] and Moiré Interferometry [12] made it possible to measure full-field displacements and strains in generic surfaces, with measurements sensitivity ranging from a few to several micrometers.

In the 1940's, the work of Dennis Gabor [13] in electron microscopy culminated with the invention of holography. This technique opened possibilities for recording a 3D representation of the object of interest by means of diffraction and interference of light. The holograms recorded contained complete information of the object, meaning that both intensity and phase could be recorded in the same photographic film. Later, with the introduction of highly coherent monochromatic lasers, holographic Interferometry [14] made full-field displacement measurements possible by interfering a hologram of an object's reference state with a hologram of the same object in its deformed state.

A simpler technique, based on the speckle phenomenon seen with laser light, called Electronic Speckle Pattern Interferometry (ESPI), had its first steps in the 1970's with the work of Leendertz [15] followed by Ennos, Archbold and Burch [16]. The speckle pattern, which is illustrated in the Figure 1-1, is observed when laser light illuminates an optically rough surface. It remains unaltered if the optical arrangement is stable, notably the laser itself, the optical elements and the illuminated surface. Any movement of the surface causes a change in the speckle pattern due to relative path length variations. The introduction of phase stepping methods [17] and digital recording elements such as CCDs [18] substantially widened the range of applications of the technique.

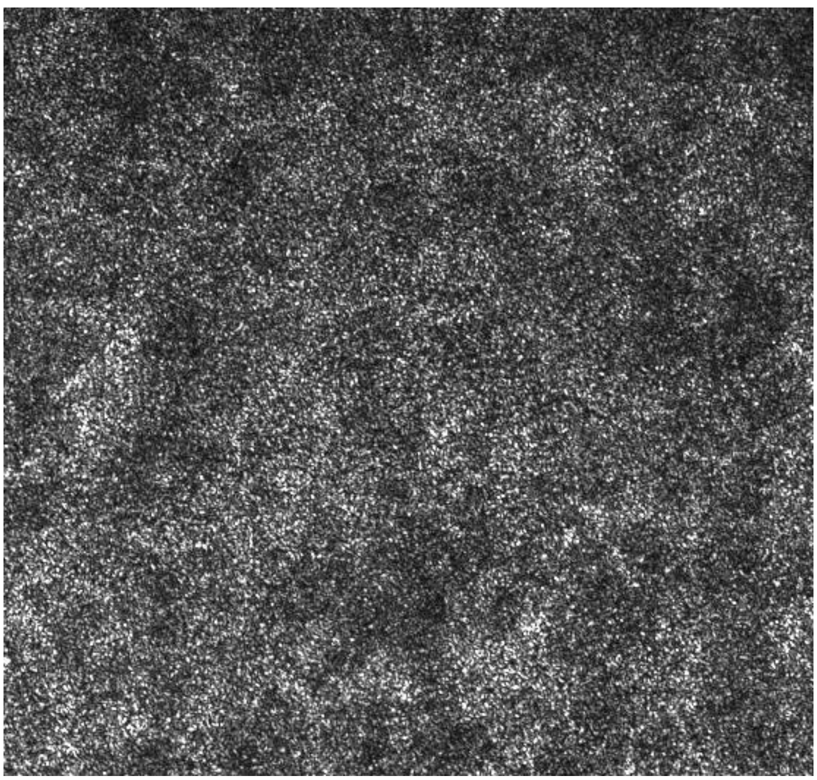

Figure 1-1. Image of a speckle pattern due to laser light scattering on an optically rough surface.

1.2 The ESPI Technique

The ESPI technique is based on the wave properties of light. When two light waves with intensity I_1 and I_2 interfere, the intensity of the resultant wave is described by

$$\mathbf{I = I_1 + I_2 + 2\sqrt{I_1 I_2}\cos\Theta} \tag{1-1}$$

where Θ is the phase difference between the two original waves. The first part of the equation, the sum of intensities, is always constant while second part is modulated by Θ. A speckle pattern has a random spatial distribution, so each point has independent I_1, I_2 and Θ quantities that locally obey Equation 1-1. Surface movement changes the relative path lengths of the two beams at each point and this changes the relative phase term Θ and hence the resultant intensity I. Recording and analysis of this intensity modulation allows the measurement of relative displacements, i.e., the difference between the states before and after deformation.

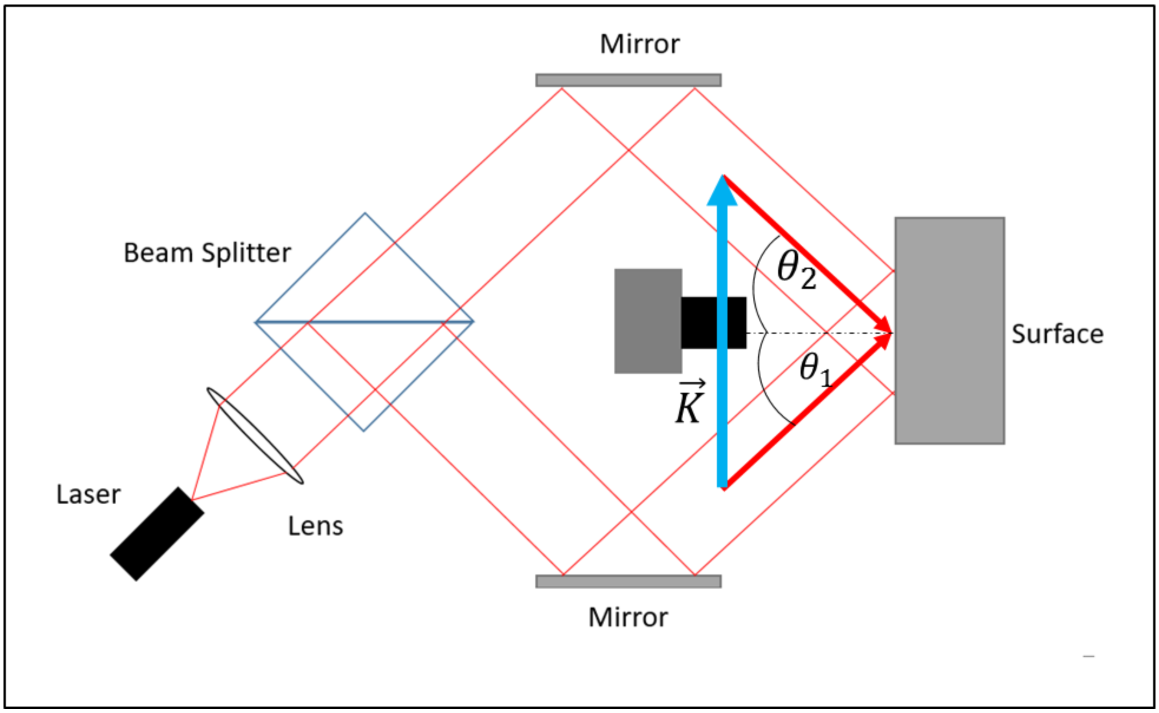

Figure 1-2. Typical in-plane ESPI arrangement. The red arrows represent the incident direction of light onto the surface and the blue arrow represents the sensitivity direction of this configuration.

Figure 1-2 shows a commonly used arrangement for ESPI, based on a Mach-Zehnder interferometer [19]. It consists of a laser light source, a collimating lens, a beam splitter, mirrors, one of which is equipped with a piezo phase shift, and a digital camera (usually CCD or CMOS).

The sensitivity direction of the arrangement is given by the vector difference between the incident waves. In this case the resultant is parallel to the specimen surface, so the arrangement in Figure 1-2 has in-plane sensitivity.

1.3 ESPI for 3D displacement measurement

Many ESPI systems are available for different applications. These systems can be categorized as pure in-plane sensitivity, pure out-of-plane sensitivity and hybrid systems. Hybrid systems are capable of measuring 3D displacements using combinations of in-plane and out-of-plane sensitivity arrangements.

Examples of pure in-plane systems can be found in many applications, especially for residual stress measurement, as the radial in-plane system developed by Albertazzi and Viotti [20] (measures in polar coordinates), the dual-axis in plane systems developed by Schajer and An [21] and Melamed [22] (both measure separately the u and v components of displacement, corresponding to the X and Y direction respectively).

For the 3D measurement, a three out-of-plane sensitivity vector system was first proposed by Shibayama and Uchiyama in 1971 in an holographic system [23] and could be also extended to ESPI. Essentially it comprised three independent out-of-plane interferometers placed with specific orientations so that they could measure combinations of u, v and w. Subsequent mathematical processing of the three different measurements provided the three displacement components separately. A subsequent system, developed by Dantec Dynamics, uses the combination of four built-in interferometers in the same optical head, as shown schematically in Figure 1-3b. In this system, the four different configurations S1, S2, S3 and S4 have each an in-plane and out-of-plane component and the combination of all of them gives the 3D measurement. The sample is placed at the intersection of the white lines.

The main disadvantage of the above-mentioned systems is that they do not offer the possibility of measuring any of the three components of displacement separately. In addition, the optical arrangements are quite complex due to the large number of additional elements such as mirrors, lenses, lasers, beam splitters, optical fiber assemblies, etc. The oblique incidence of the light also makes a requirement for high coherence sources due to large path length differences at the measuring surface, and therefore more complex, bulky and more expensive lasers.

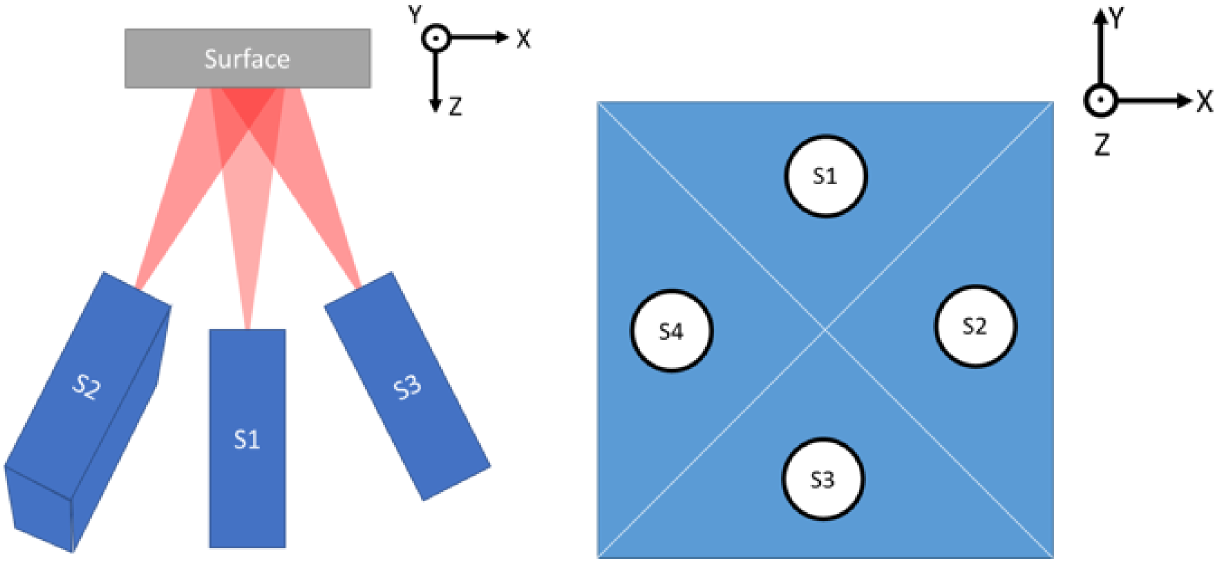

Figure 1-3. (a) Schematic view of a three-channel system for 3D ESPI. (b) Schematic view of the four out-of-plane arrangement for 3D ESPI.

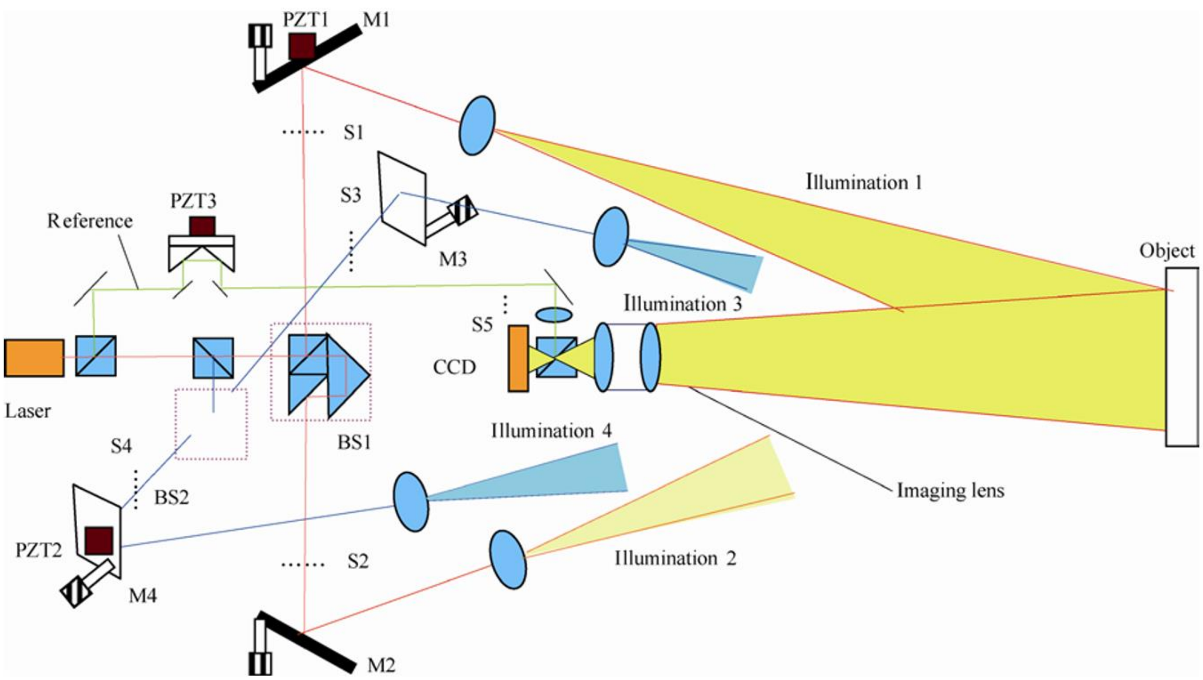

Figure 1-4. ESPI arrangement that combines in-plane and out-of-plane sensitivity for measuring 3D displacements.

Figure 1-4 shows a different type of system proposed by Martinéz et.al. [24][25] that uses a combination of two in-plane sensitivity branches and one out-of-plane sensitivity branch to reduce the problem of having always coupled measurements. In this system, there are two in-plane sensitivity arrangements, illumination 1 and 2 and illumination 3 and 4, respectively. The beams can be switched off to have only two beams at a time interfering at the surface. A fifth beam is directed straight to the CCD. The fifth beam is required for the out-of-plane measurement and is used combined with either beam 3 or 4. Thus, a total of three measurements is required to obtain the complete displacement field with the advantage of two direct measurements for in-plane displacements. The sensitivity in this proposed arrangement varies with the observation direction due to the beams not being collimated. The complexity is noticeable due to the need to split the beam several times and the arrangement requires high quality lasers to work.

1.4 Proposed new system arrangement and objectives

The main objective of this research is to develop a simplified interferometer capable of measuring the 3 components of displacement, u, v and w.

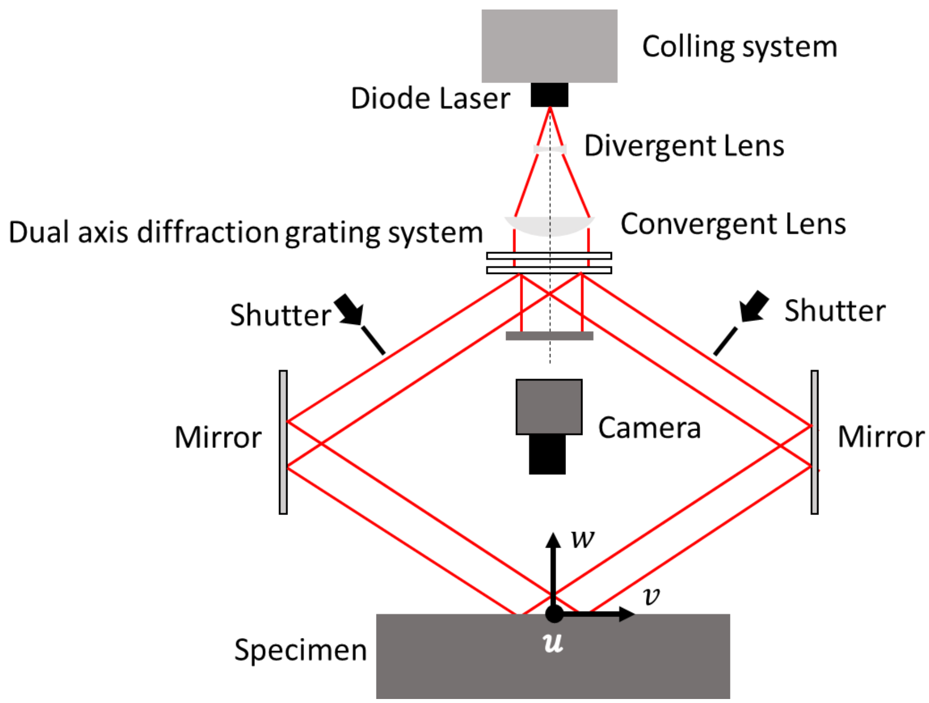

Figure 1-5. Concept of proposed arrangement showing one of the in-plane branches.

The proposed system uses a laser diode as light source in combination with a diffraction grating assembly. The dual grating assembly allows the use of two in-plane arrangements to measure u and v directly and independently. They two arrangements have different sensitivity magnitudes, i.e., the beams in X and in Y have different incidence angles. The combination of beams from the X arrangement with beams form the Y arrangement creates a system capable of measuring 3D displacements, with reduced number of components. By combining crossed beams, i.e., a beam from one in-plane arrangement with a beam from the other, the resulting sensitivity vector has out-of-plane component which then enables measurement of w.

The proposed design is capable of measurements in up to six different sensitivity directions. A minimum of three measurements are necessary to obtain the complete 3D displacement map. This feature offers the possibility of redundant measurements that can be used for data averaging and to reduce uncertainty and increase accuracy.

The main objectives of this research work can be summarized as to:

- Develop a practical optical arrangement capable of multi-axis sensitivity for 3D displacement measurement;
- Transform the experimental arrangement into a portable, robust and easy to operate system.
- Test the effectiveness of the system for 3D displacement measurement regarding sensitivity, noise levels, robustness, stability.
- Investigate the performance of a laser diode as a light source for both in-plane and out-of-plane measurements.
- Study and explore the limits of the system regarding coherence requirements, environment influence, thermal stability, stiffness, etc.

The main questions answered with this work are:

- Can a laser diode with very limited coherence length be used effectively for both in-plane and out-of-plane displacement measurements?
- What are the limitations of sensitivity and accuracy that are inherent to the arrangement proposed?
- How does the data redundancy affect the measurement quality?
- What are the potential advantages or disadvantages of the proposed arrangement when compared to already existing systems?

In the following chapters, the necessary developments for understanding the ESPI technique and the proposed arrangement will be given. Chapter 2 presents a brief review of optical concepts such as the nature of light, interference, lasers and speckle formation.

Chapter 3 introduces the ESPI technique in more detail. The commonly used sensitivity arrangements for in-plane and out-of-plane measurement is presented and the technique of phase shifting is introduced. The concept of visibility and effect of coherence in the measurement quality are presented.

In Chapter 4, the diffraction grating based interferometer is presented. The phase shifting technique is adapted to the grating interferometer and the procedure is explored. The system's proposed layout is introduced and the features enabling in-plane and out-of-plane measurements are presented. Coherence and alignment aspects are discussed. The design and construction steps of a portable device for 3D measurements are shown in detail.

Chapter 5 discusses some performance aspects of the device, such as stability, robustness, sensitivity and accuracy. A designed sample is used to test the functionality of the system for measuring 3D displacements. Validation though FEA is presented. The data averaging method is applied and its effects on accuracy and uncertainty are discussed.

Chapter 7 discusses the results, with focus on accuracy, robustness and quality of the measurements. An analysis of the advantages of multiple measurements and their effect on overall performance is included. At the end, the chapter presents concluding remarks and comments on the scope for future work.

Chapter 2: Optics Review

2.1 Light and its properties

There are several ways to treat light. The most common understanding is that light propagates as rays in a straight line, which is referred to as ray optics or geometrical optics. A more refined approach treats light as a wave, with amplitude and phase, and offers explanation to the phenomenon of interference and diffraction. A more rigorous description of light is given by the electromagnetic theory, the foundation of which rests on James Clark Maxwell's work [26] and by quantum theory, which treats light as photons, or small packets of light with well-defined energy and frequency [27]. The two later theories are used to explain phenomena such as interference and diffraction and also give foundations to engineering applications such as lasers.

From the electromagnetic theory, light is a wave composed of an electric field and a magnetic field, oscillating orthogonally to the propagation direction. Light waves do not require a medium of propagation and in free space, travel at a speed $c \cong 3 \times 10^8 m/s$ in vacuum. Important characteristics of electromagnetic waves are the wavelength λ, which relates directly to wave's frequency $f = c/\lambda$, amplitude, phase, polarization and direction of propagation. Figure 2-1 shows schematics of an electromagnetic wave, with the electric and magnetic fields, direction of propagation and wavelength indicated.

The equation describing a generic plane wave – in terms of electric field - travelling in the x direction in free space is given below:

$$\mathbf{E} = \mathbf{E_0} \cos(\mathbf{k_x}.\mathbf{x} - \boldsymbol{\omega}.\mathbf{t} - \boldsymbol{\phi})\,\hat{\mathbf{y}} \qquad (2\text{-}1)$$

where the component E_0 refers to the amplitude of the electric field, which is oscillating in the y direction as indicated by $\hat{y}$. The quantity k_x is the wave number and has absolute value of $2\pi/\lambda$. $\omega = 2\pi f$ is the angular frequency and ϕ is the initial phase of the wave.

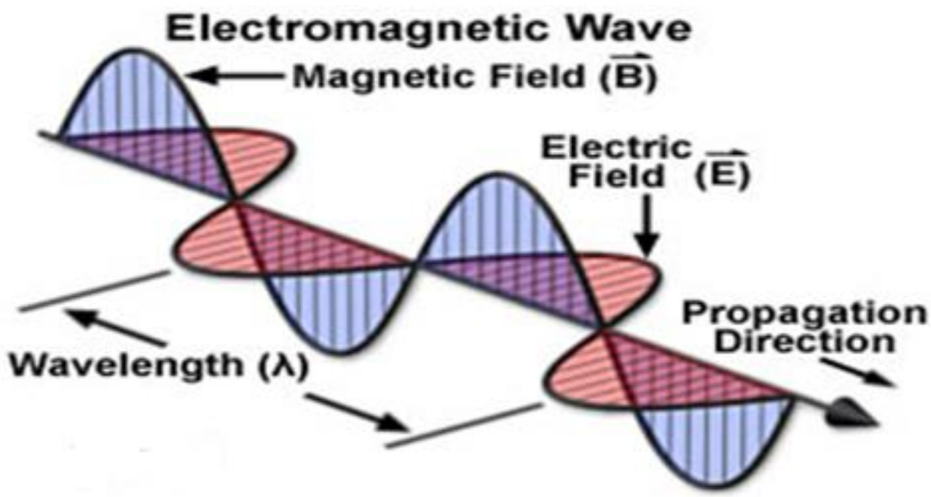

Figure 2-1. Schematics of an electromagnetic wave. The electric (red) and magnetic (blue) are shown oscillating orthogonally to each other and to the propagation direction.
[Source: https://www.quora.com/What-is-the-source-of-energy-of-electromagnetic-waves].

The solution given by Equation 2-1 can also be presented in complex notation, which simplifies the mathematical treatment

$$\vec{\mathbf{E}} = \tilde{\mathbf{E}}\mathbf{e}^{-\mathbf{i\omega t}} \tag{2-2}$$

where

$$\tilde{\mathbf{E}} = \mathbf{E_0}\mathbf{e}^{\mathbf{i(k_x.x-\phi)}}\hat{\mathbf{y}} \tag{2-3}$$

is called the complex amplitude.

It is convenient to treat light in terms of the electric field. The plane of oscillation, called the polarization plane, is important in phenomena such as reflection and interference. In engineering, treating light in terms of intensity is more practical. The intensity can be defined as a time average of the square of the electric field over a period much larger than the wave's period $T = 1/f$. Therefore, the intensity is defined as

$$\mathbf{I} \propto \langle \mathbf{E^2} \rangle \tag{2-4}$$

2.2 Interference

The interference phenomenon regards the interaction between two or more fields in which they superpose to give form to a new field. Interference is also observed in vectorial fields such as electromagnetic waves. For example, in Figure 2-2. there are two electric waves of same frequency but with different amplitudes E_1 and E_2. The plot on top shows the waves in phase where the resultant interference is constructive. In the plot at the center, the wave 2 (blue dotted line) is with a phase difference of 60° in relation to the wave 1(red solid line), and the amplitude and phase of the interference (green dashed line) are affected. In the bottom plot, the waves are out-of-phase and the resulting interference is destructive, with a consequent non-zero amplitude (green dashed line) due to the fact that wave 1 and wave 2 have different amplitudes

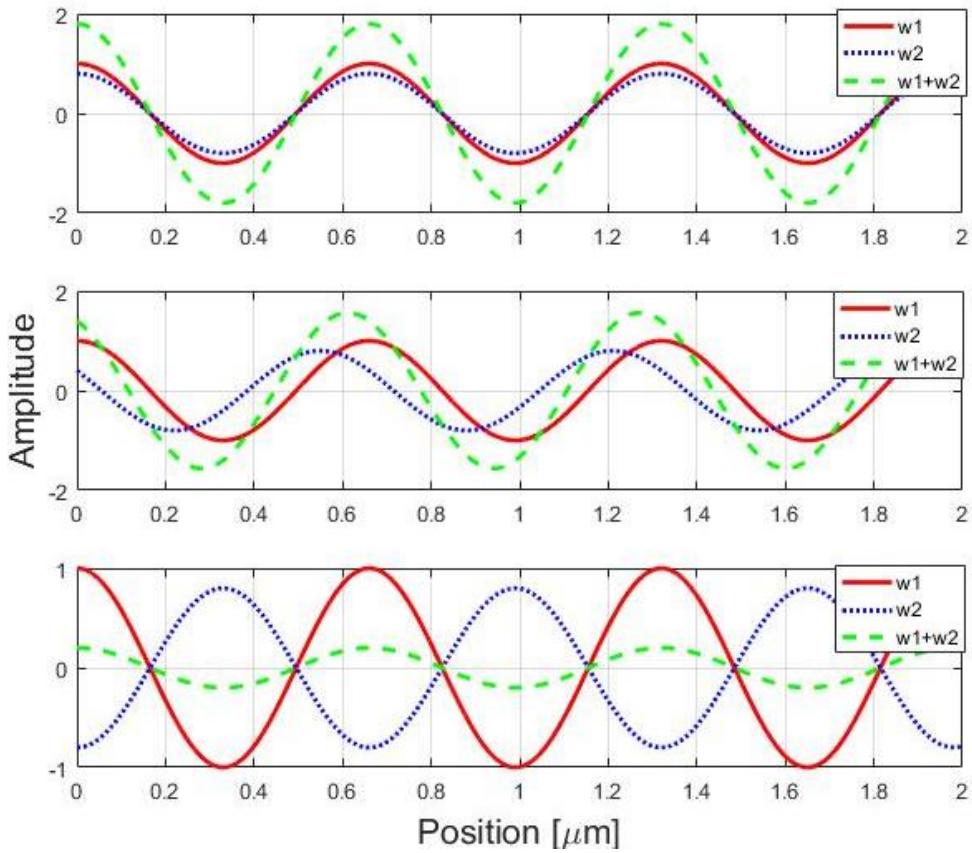

Figure 2-2. Top: wave 1 and wave 2 are in phase and the interference is constructive. Center: wave 2 is 60 degrees delayed in respect to wave 1 and the interference is partially constructive. Bottom: wave 1 and wave 2 are out of phase and interference is destructive with a consequent non-zero amplitude since the waves have different amplitudes.

Mathematically, optical interference is just a linear superposition of the electromagnetic fields. In terms of intensity, the relation is less intuitive. Let the waves be described by $\vec{E}_1 = \tilde{E}_1 e^{-i\omega t}$ and $\vec{E}_2 = \tilde{E}_2 e^{-i\omega t}$. In this case, where the waves are plane and travelling in an arbitrary direction, their complex amplitudes can be written as $\tilde{E}_1 = E_1 e^{i(k_1 r - \phi_1)}$ and $\tilde{E}_2 = e^{i(k_2 r - \phi_2)}$. The vectors k_1 and k_2 are in the respective propagation directions of the two waves and the vector r is a position vector. The interference is then

$$\vec{\mathbf{E}} = \vec{\mathbf{E}}_\mathbf{1} + \vec{\mathbf{E}}_\mathbf{2} \tag{2-5}$$

The resultant intensity is of the form

$$\mathbf{I} = \langle \vec{\mathbf{E}}^\mathbf{2} \rangle = \langle \left(\vec{\mathbf{E}}_\mathbf{1} + \vec{\mathbf{E}}_\mathbf{2}\right)^\mathbf{2} \rangle = \langle \vec{\mathbf{E}}_\mathbf{1}^\mathbf{2} + \vec{\mathbf{E}}_\mathbf{2}^\mathbf{2} + \vec{\mathbf{E}}_\mathbf{1}\vec{\mathbf{E}}_\mathbf{2}^* + \vec{\mathbf{E}}_\mathbf{1}^*\vec{\mathbf{E}}_\mathbf{2} \rangle \tag{2-6}$$

The terms with * in Equation 2-6 are complex conjugates. Notice that in the products, waves with different polarization would result in a null product. The implication is that waves with different polarization cannot interfere. After some algebra and using complex number identities, Equation 2-6 yields

$$\mathbf{I} = \mathbf{I}_\mathbf{1} + \mathbf{I}_\mathbf{2} + \mathbf{2}\sqrt{\mathbf{I}_\mathbf{1}\mathbf{I}_\mathbf{2}}\,\mathbf{cos}\boldsymbol{\Theta} \tag{2-7}$$

Equation 2-7, called interference equation, shows the resulting intensity of the interference pattern. It is composed of a constant part, which is the sum of the individual intensities, and of a second part that depends on Θ. The phase term in Equation 2-7 is

$$\boldsymbol{\Theta} = (\mathbf{k}_\mathbf{1} - \mathbf{k}_\mathbf{2}).\,\mathbf{r} - (\boldsymbol{\phi}_\mathbf{1} - \boldsymbol{\phi}_\mathbf{2}) \tag{2-8}$$

and represent the relative phase between the two incident waves. The vector product $(k_1 - k_2).r$ represents a phase difference dependent on the incidence of the two waves and in a position vector r. Any change in r will cause a proportional change in phase.

2.3 Diffraction

Diffraction is a phenomenon related to the wave characteristics of light and its interaction with objects around it or in its way. The concept of diffraction can be found in more details in [28]. A diffraction grating is a well-known component that is capable of interacting with light and splitting it according to the wavelength.

A transmission diffraction grating is usually made of a glass substrate with periodic structures carved into the surface or added holographically. The grooves in the diffraction grating, which act like the slits in Young's experiment [29], absorb and transmit the light, producing a periodic intensity pattern that results in new waves, which exit the grating at very well defined angles.

The relation between the grating spacing, the order of diffraction, the wavelength and the angle of diffraction is given by the Bragg equation

$$\mathbf{p}\sin\boldsymbol{\theta} = \pm \mathbf{m}\boldsymbol{\lambda} \tag{2-9}$$

where m is an integer representing the diffraction order.

White light incident in a grating has its spectrum revealed since for every different wavelength the diffraction angle is different. The result is the colors of the rainbow. When monochromatic light, such as that of a laser, is passed through a diffraction grating, the light is also diffracted according to Equation 2-9. On Figure 2-3, a cross section of a diffraction grating is shown with the black dots representing the grooves. A plane wave with wavelength λ incident to the grating has its wavefront, a set of points with the same phase, deflected according to the spacing p and λ.

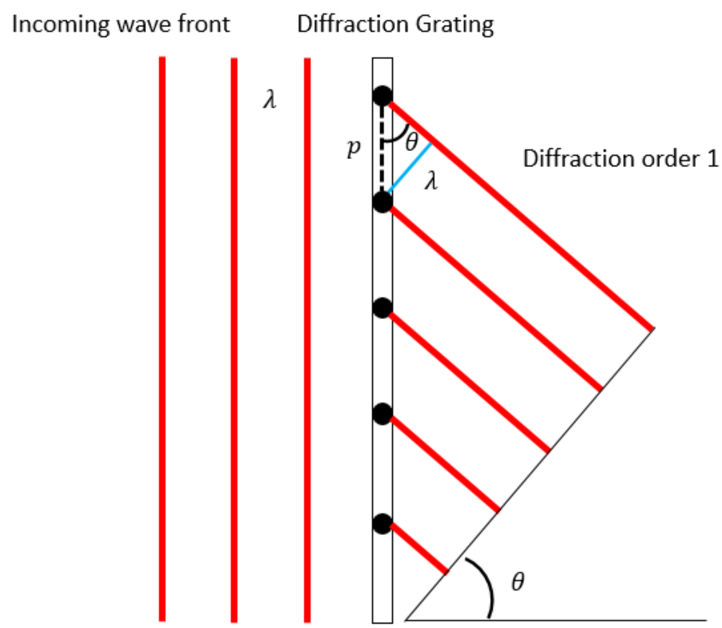

Figure 2-3. Schematics of a diffraction grating with a monochromatic wave. The diffraction order 1 is seen and the relation between λ, p and θ is given by the Bragg Equation (2-9).

The use of diffraction gratings with lasers has many applications in interferometry, especially for ESPI.

2.4 Lasers

LASER, acronym for Light Amplification by Stimulated Emission of Radiation, is an important light source used in engineering. Laser light has properties such as high brightness and coherence, which are very important for metrological applications.

The theoretical aspects of lasers are described in details in [30] and in [31]. The essential elements of a laser are the gain medium, the resonant cavity, which provides optical feedback, and an energy pumping mechanism.

The gain medium can be a crystal, a gas or gas mixture, a liquid, a semiconductor, or even a glass fiber. The atoms in the gain medium are excited by the energy pumped into the system and its electrons ascend to higher energy levels. The electrons decay spontaneously to lower energy levels emitting photons in a process called spontaneous emission. While there is spontaneous emission, energy is still being pumped into the system and more atoms are raised to higher levels of energy to create a state known as population inversion. The emitted photons interact with excited atoms, stimulating electrons to decay and emit a photon with the same phase and frequency of the photon responsible for the emission. This process is known as stimulated emission. The presence of mirrors at both ends of the cavity allows a build-up of energy inside the cavity as photons are reflected back into the gain medium increasing the stimulated emission rate. Part of the light, usually a few percent, is transmitted through the partial mirror in one end of the cavity as the output.

Optical feedback combined with stimulated emission cause the generated light to have very high monochromaticity. What makes laser light special is the fact that the photons generated inside the cavity all have similar phase and frequency for each longitudinal mode allowed to oscillate. The factors that dictate which longitudinal modes can oscillate and be amplified are: cavity length characteristics and gain medium characteristics.

The cavity length dictates the frequencies or wavelengths allowed to oscillate. There must be an integer number of wavelengths in the round trip inside the cavity and the longitudinal modes oscillate as standing waves. The frequency spacing between the modes, also known as spectral range, is given by

$$\boldsymbol{\Delta\nu = \frac{c}{2L}} \tag{2-10}$$

The gain medium has usually a bandwidth ranging from a few MHz to a few hundreds of GHz, which is very narrow compared to usual hundreds of THz for light frequencies. This way, in general, only a few longitudinal modes can oscillate and be amplified. The high degree of monochromaticity leads to the property called coherence.

Coherence is a measure of phase correlation within the same wave and can be classified as temporal and spatial coherence. Temporal coherence of a wave refers to the degree of correlation of phase at a time t with its phase at a time $t + \tau$. If it is possible to correlate the phase at time t with the phase at the time $t + \tau$, and $0 \leq \tau \leq \tau_c$, τ_c is called coherence time. The coherence length is defined as $\Delta_c = c\tau_c$. On the other hand, spatial coherence regards the correlation of a wave's phase at point P_1 with its phase at point P_2, in the same wavefront, as a function of time [32].

While there are several ways of producing laser light, perhaps one of the most important in engineering applications is by using semiconductors. Semiconductor lasers, or simply diode lasers, as the name suggests, are composed of a diode-like structure that acts as a gain medium. When it is pumped electrically by a current in the forward direction, the passage of current from one terminal to the other induces the population inversion, stimulating the atoms in the gain medium to emit light with frequencies that fall within the gain medium bandwidth. At both ends of the semiconductor structure, usually composed of elements like Al, Ga, As, In, P among others, high quality surfaces with high indexes of refraction act as partial mirrors to provide optical feedback.

Usually, the bandwidth of the gain medium in a laser diode is large so that more than one longitudinal mode can be stimulated at the same time. On Figure 2-4, it is possible to see an example of that, in which the main envelope represents the gain medium of a laser diode and the narrow peaks within it represent the simultaneous oscillating modes.

The characteristics shown on Figure 2-4 are very important from the point of view of coherence in a laser diode. The spacing between the longitudinal modes is given by Equation 2-10.

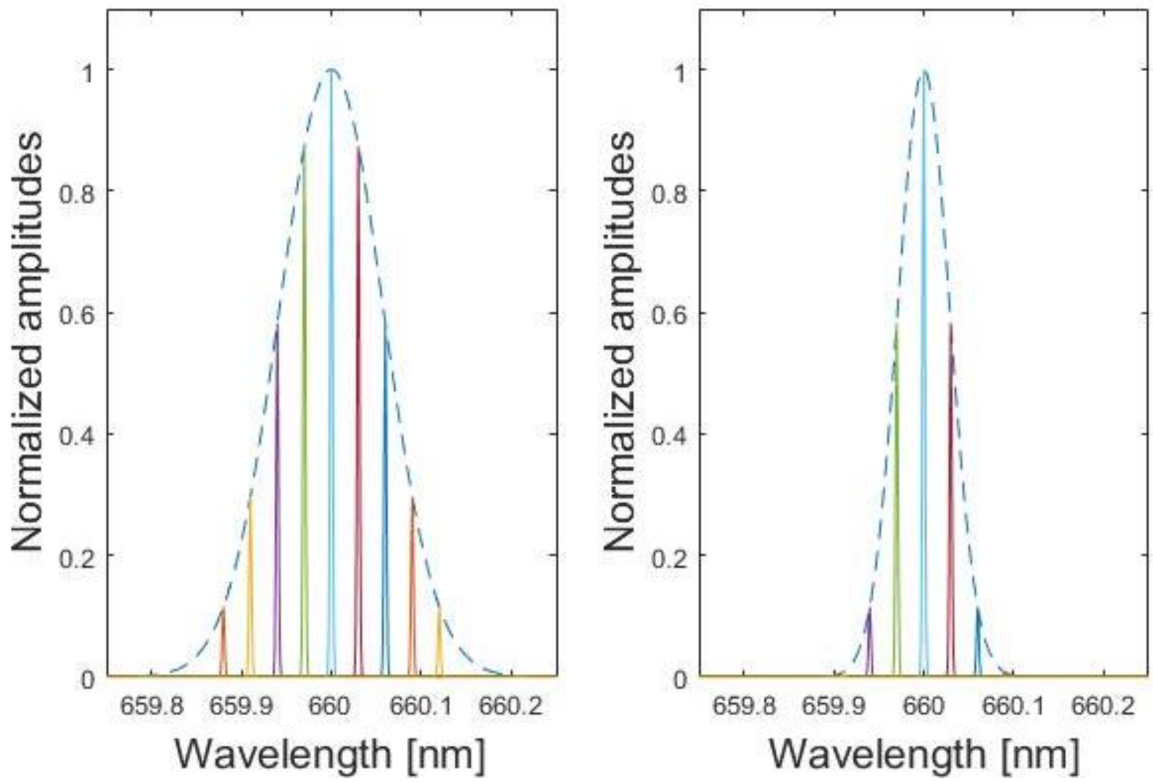

Figure 2-4. Characteristic spectrum of a diode laser. Left: Broad gain medium with several longitudinal modes within the gain medium. Right: A narrower gain medium reduces the amount of simultaneous longitudinal modes that are amplified in the cavity.

The presence of more than one longitudinal mode leads to repeated intervals of coherence [33]. In fact, if the wavelength difference between one mode and the next is $\Delta\lambda$, it can be shown that the interval of coherence is

$$\mathbf{H} = \frac{\boldsymbol{\lambda}^{2}}{\boldsymbol{\Delta\lambda}} \tag{2-11}$$

On the other hand, the bandwidth of the gain medium, which determines how many modes can oscillate at the same time, drives the coherence length in a diode laser. The relation between coherence length and bandwidth is like the one shown in Equation 2-11

$$\boldsymbol{\Delta l_c} = \frac{\boldsymbol{\lambda}^{2}}{\overline{\boldsymbol{\Delta\lambda}}} \tag{2-12}$$

where $\overline{\Delta\lambda}$ is the gain medium bandwidth at FWHM [30].

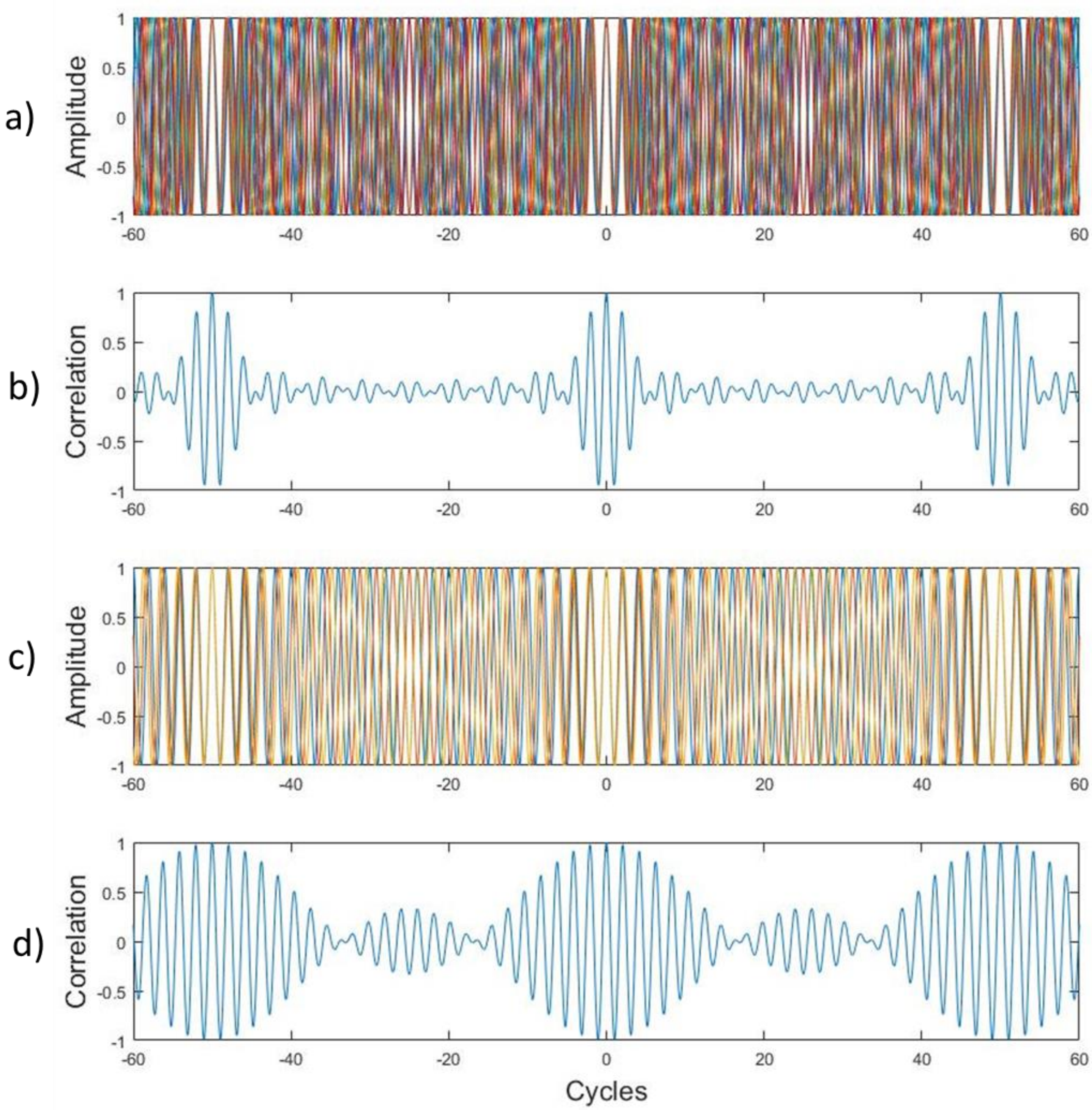

Figure 2-5.(a) Total of nine modes with wavelengths around two units of length shown in the same diagram. The repeating interval of good correlation is fifty cycles. (b) Measure of correlation of the waves seen in (a). The correlation length, equivalent to coherence length, is very sharp due to the high number of modes oscillating at the same time. (c) Total of three modes oscillating at the same time. The interval for good correlation is not altered. (d) Correlation plot showing that a reduced amount of modes, equivalent of reducing the gain medium bandwidth, increases the correlation length when compared to (b).

Figure 2-4 shows an example of how reducing the gain medium bandwidth influences the number of modes oscillating in the cavity. On Figure 2-5, schematics show in practice how the repeated coherence intervals occur. For simplicity, a wavelength of 2 units of length was chosen with a coherence interval of 50 cycles. On Figure 2-5(a), a total of 9 waves with slightly different wavelengths are shown. It is possible to see that the correlation is good close to zero, close to -50 and 50. On Figure 2-5(b), the normalized addition of all the waves give an idea of the length of correlation, i.e., the length to which the waves are relatively in phase with each other. Figure 2-5(c) shows a case in which the number of modes interacting is reduced to 3. The equivalent of this can be seen on Figure 2-4 (right) where the gain medium bandwidth is reduced. The correlation range is increased per Figure 2-5(d). The coherence interval remains the same as can be seen in both Figure 2-5(c) and Figure 2-5(d), since the spectral range is the same as in Figure 2-5(a).

2.5 Speckles

Speckle is an important phenomenon that occurs with coherent light such as laser light. When a laser illuminates an optically diffuse surface, i.e., a surface in which the irregularities are of the wavelength scale, the waves are scattered. The original wave is decomposed in several wavelets propagating in random direction with random spatial phase distribution due to the surface's irregularities. The high degree of coherence enables an interference pattern to form in space and to be imaged into an observer's eyes or onto a digital camera CCD, as exemplified in Figure 2-6.

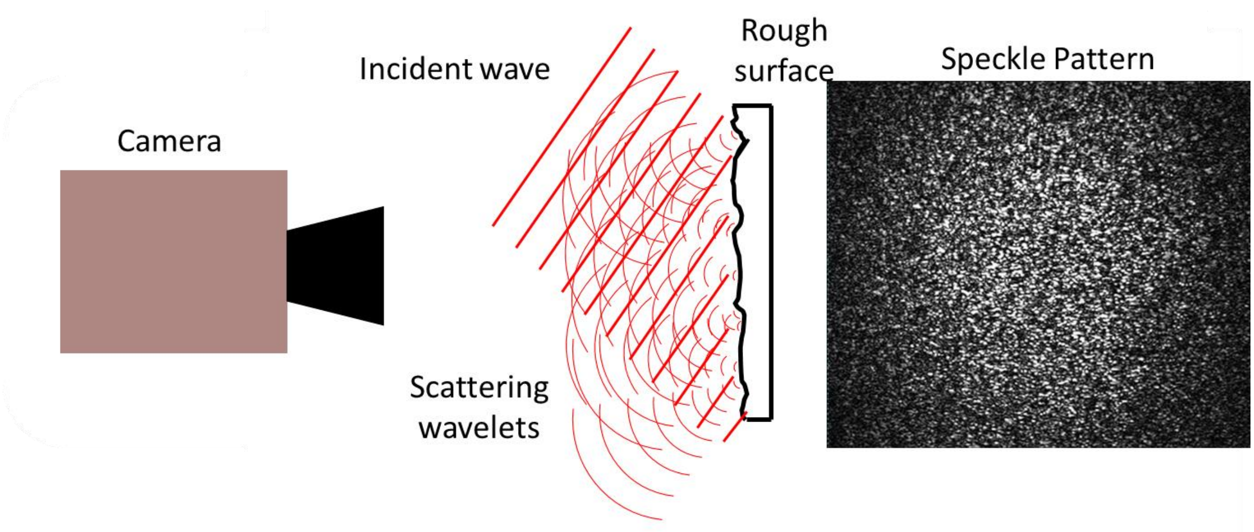

Figure 2-6. Left: Schematics of scattering process due to incidence of coherent light into a rough surface. The speckle pattern is imaged by an observer, in this case a camera. Right: Image of laser speckle pattern.

The dark and bright spots in the speckle pattern correspond to destructive and constructive interference, respectively. Equation 2-7 still applies in this case, therefore the intensity at any point depends on the relative phase between the interfering wavelets. A detailed study of speckle statistics shows that the phase distribution across the pattern is random [34]. However, locally, the phase varies smoothly as a function of surface movement, which causes a change in relative path length and therefore an intensity modulation.

The speckle properties are very interesting from the point of view of metrology and are used in ESPI. The next chapter presents the ESPI technique in more details. Concepts explored in this chapter, such as phase, intensity, interference and coherence, will contribute for the understanding of the technique.

Chapter 3: ESPI Technique

3.1 Sensitivity arrangements

Electronic Speckle Pattern Interferometry (ESPI) is a measurement technique where the phase of speckles is monitored to obtain information about the surface movement or deformation. Various optical arrangements are available to track different deformation types.

An ESPI interferometer is typically composed of a laser source, a lens system to shape the laser beam, a beam splitter to create two light beams from the same source, sets of mirrors, at least one equipped with a transducer, usually a piezoelectric actuator (PZT), to provide phase shift, and a digital camera for recording the speckles formed by interference at the specimen's surface or at the CCD. The most used optical arrangements for ESPI are the in-plane arrangement and combinations of out-of-plane arrangements

Figure 3-1(a) shows an example of an in-plane arrangement. The illumination angle θ is the same for both incident beams. The wavevectors k_1 and k_2 are

$$\mathbf{k_1} = \frac{2\pi}{\lambda}(\sin\theta\hat{\mathbf{x}} - \cos\theta\hat{\mathbf{z}}) \tag{3-1}$$

$$\mathbf{k_2} = \frac{2\pi}{\lambda}(-\sin\theta\hat{\mathbf{x}} - \cos\theta\hat{\mathbf{z}}) \tag{3-2}$$

The sensitivity vector K is given by the subtraction

$$\mathbf{K} = \mathbf{k_1} - \mathbf{k_2} = \frac{4\pi\sin\theta}{\lambda}\hat{\mathbf{x}} \tag{3-3}$$

The result shown in Equation 3-3 comes directly from the interference formulation. Recalling Equation 2-8, the vector K appears in a scalar product with the position vector r, which results in a phase term dependent on position. A variation in r, in the direction of K, causes a proportional phase change. From Figure 3-1(a), a displacement in the direction of K, i.e., to the right, induces a path length change for both beams 1 and 2. Beam 1 has its path slightly increased while beam 2 has its path decreased. The change in path length is what causes the relative phase change, which in turn causes a variation of intensity in the speckle pattern.

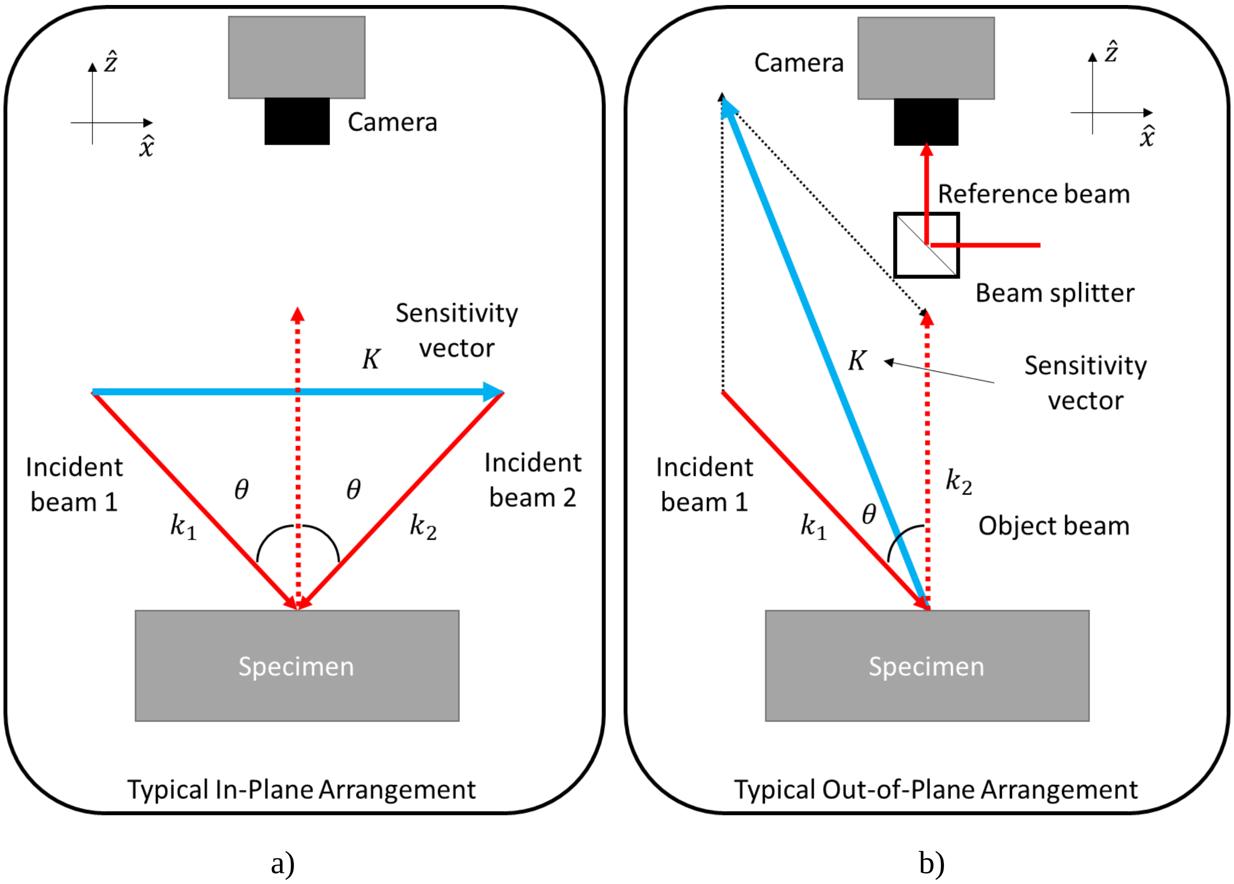

Figure 3-1.(a) In-plane arrangement for ESPI. The incidence angles are symmetric and the subtraction of the wave vectors results in a fully in-plane sensitivity vector. b) Typical out-of-plane arrangement. Only one illumination beam is used at the surface and the interference happens at the recording plane with a reference beam. The orientation of the camera and the illumination beam determine the sensitivity direction.

Figure 3-1(b) shows a different arrangement. There is only one beam incident to the surface. A reference beam is directed directly to the CCD. The sensitivity vector K in this case is given by

$$\mathbf{K} = \mathbf{k_2} - \mathbf{k_1} = \frac{2\pi}{\lambda}(-\mathbf{sin\theta}\hat{\mathbf{x}} + (\mathbf{1} + \mathbf{cos\theta})\hat{\mathbf{z}}) \tag{3-4}$$

where the object vector k_2 is in the direction of the reference beam [35].

Notice that the position of the camera changes the direction of k_2, and therefore the sensitivity of the arrangement is dependent on both the incident beam and camera orientation.

The out-of-plane sensitivity arrangement shown in Figure 3-1(b) is a combination of in-plane and out-of-plane sensitivity. It is therefore impossible to determine both displacements u

and w with a single measurement. On the other hand, it is possible to obtain pure out-of-plane sensitivity by arranging the observation angle to be symmetric with the illumination angle [35].

3.2 The Four-step method for static measurements

The ESPI technique that tracks displacements by measuring relative phase changes of the speckles. While a camera or even an observer's eyes cannot record phase variations due to light's extremely high frequencies – order of hundreds of THz – the intensity, which is a time averaged quantity, can be recorded. Equation 2-7 shows that a relative phase change between two light beams causes an intensity modulation. The same equation applies for intensity in a speckle pattern. While the spatial phase distribution in a speckle pattern is random, the variations of phase in every point obey the interference equation.

A key factor in ESPI is how to use the intensity information to retrieve the phase. The method of phase-shifting, first introduced in 1985 by Creath [17], is a practical technique that allows quick phase calculation based on the speckle pattern modulation. The method consists of taking a series of images where a known phase shift is made from one image to the next. The phase is shifted by means of moving one of the mirrors in the arrangement using a piezoelectric transducer (PZT). While a minimum of three pictures are necessary for the phase shift technique, usually four pictures are taken – the so called four-step method - to simplify the calculation and increase accuracy.

Figure 3-2. Top: Conventional ESPI arrangement for in-plane measurement. There is an intrinsic path length difference between the two beams when they meet at the surface. Bottom: The movement of the PZT mirror causes a lateral shift on the inferior beam, and a different ray (green) interferes with the original (red) ray from the superior arm. The path length difference is changed as can be noticed with $\boldsymbol{\delta}1$ and $\boldsymbol{\delta_2}$.Figure 3-2 shows in more detail a typical in-plane interferometer used for ESPI. The light produced by the laser is first collimated by a lens and then split by a beam splitter. Two mirrors direct the light onto the specimen surface and the resulting speckle pattern is recorded by a digital camera. The displacement of the PZT mirror causes a path length change in the lower beam which changes the relative phase of the two beams. This change in path length is exemplified on Figure 3-2 by the solid and dotted lines δ_1 and δ_2. The displacement required for such a phase shift is usually of the order of fractions of the wavelength, so there is no apparent change in the illuminated area.

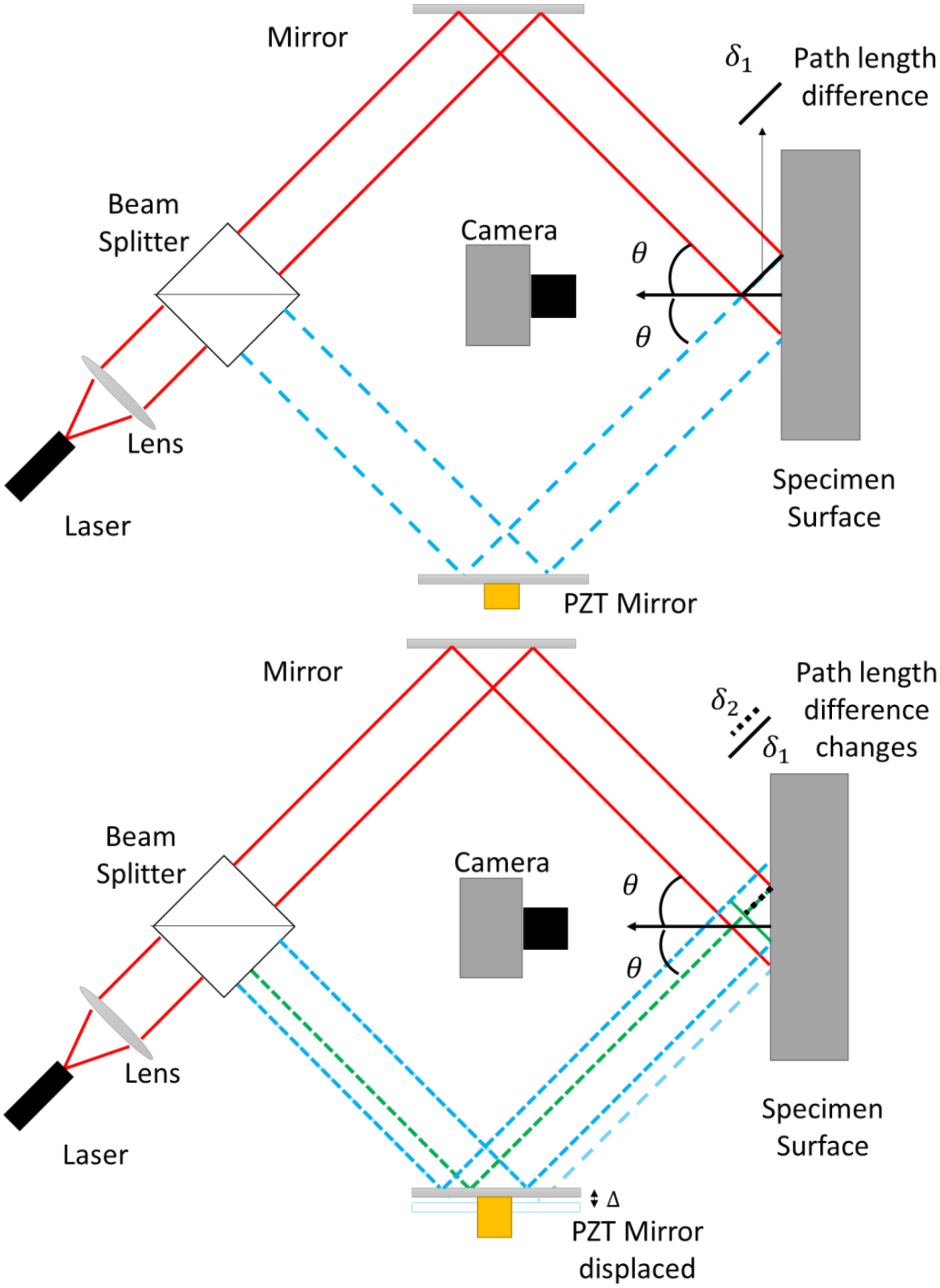

Figure 3-2. Top: Conventional ESPI arrangement for in-plane measurement. There is an intrinsic path length difference between the two beams when they meet at the surface. Bottom: The movement of the PZT mirror causes a lateral shift on the inferior beam, and a different ray (green) interferes with the original (red) ray from the superior arm. The path length difference is changed as can be noticed with δ1 and δ_2.

The process used in the four-step method is straightforward. Let I_i be the intensity of the ith image recorded before deformation. The sum of intensities from Equation 2-7 is replaced by $\mathrm{A_b}$ and the interference term amplitude by B_b, for simplicity. The phase term $\Theta_b$is the quantity of interest. The intensity at every point in the illuminated area for the first image is

$$\mathbf{I_1 = A_b + B_b cos\Theta_b} \tag{3-5}$$

The second picture is captured after the introduction of a $\frac{\pi}{2}$ phase shift in one of the beams. The intensity now is

$$\mathbf{I_2 = A_b + B_b cos\left(\Theta_b + \frac{\pi}{2}\right) = A_b - B_b sin\Theta_b} \tag{3-6}$$

Similarly, for the next two pictures

$$\mathbf{I_3 = A_b + B_b cos(\Theta_b + \pi) = A_b - B_b cos\Theta_b} \tag{3-7}$$

$$\mathbf{I_4 = A_b + B_b cos\left(\Theta_b + \frac{3\pi}{2}\right) = A_b + B_b sin\Theta_b} \tag{3-8}$$

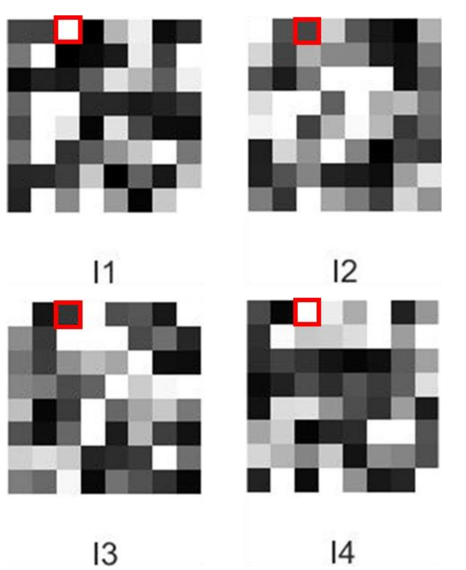

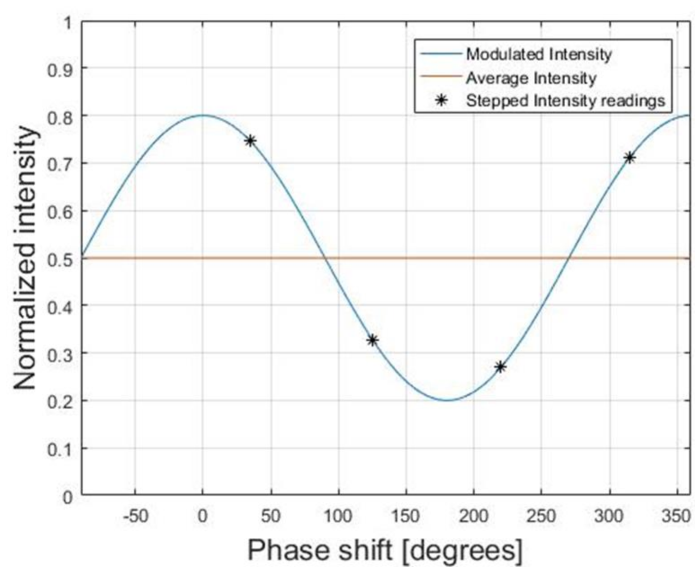

a) **b)**

Figure 3-3.(a) Example phase stepped speckle patterns. The addition of phase when using the phase shift technique modulates the intensity as per Equation 2-7. The intensity information of all pictures is processed by digital subtraction to obtain the phase in every pixel. b) Sinusoidal interpolation of the intensity variation of the example pixel show in in red in (a).

Figure 3-3(a) illustrates the modulation of intensity caused by the phase shift. The intensity modulation of one pixel, highlighted in red, is shown in Figure 3-3(b). The blue curve is the intensity modulation given by Equation 2-7 while the red curve is the average intensity. The dark dots represent intensity values captured for the highlighted pixel after each 90° phase step. These recorded intensities are processed digitally to obtain the phase term. Observe that, from Equations 3-5 - 3-8, $I_4 - I_2 = 2B_b sin\Theta_b$ and that $I_1 - I_3 = 2B_b cos\Theta_b$. The average intensity A_b is eliminated in the process. In practice, the subtraction is done digitally in the computer. The phase of the reference state can be determined by

$$\boldsymbol{\Theta_b = \text{atan}\left(\frac{I_4 - I_2}{I_1 - I_3}\right)} \tag{3-9}$$

Even though it is possible to calculate the phase in each state separately, it is more practical to obtain the phase difference directly. Before calculating the phase difference, the same procedure of phase shifting has to be used for the deformed surface. Let the set of pictures of the deformed state be called J_i. The sequence of pictures is taken similarly as for the reference state.

$$\boldsymbol{J_i = A_a + B_a \cos(\Theta_a + \frac{(i-1)\pi}{2})} \tag{3-10}$$

where A_a, B_a and Θ_a are the intensity sum, the cross-interference term and the phase after deformation, respectively. By labelling $I_4 - I_2 = I_n$, $I_1 - I_3 = I_d$, $J_4 - J_2 = J_n$ and $J_1 - J_3 = J_d$ and using the identity

$$\boldsymbol{\tan(\Theta_a - \Theta_b) = \frac{\tan\Theta_a - \tan\Theta_b}{1 + \tan\Theta_a \tan\Theta_b}} \tag{3-11}$$

we have that the phase difference $\Delta\Theta$ is

$$\boldsymbol{\Delta\Theta = \Theta_a - \Theta_b = \text{atan}\left(\frac{J_n I_d - I_n J_d}{I_d J_d + I_n J_n}\right)} \tag{3-12}$$

The phase map resulting from Equation 3-12 contains information regarding the displacement or deformation map. Because of the cyclic nature of the arctangent function, the angle $\Delta\Theta$ is determined only within a 2π range, with repetitions at 2π intervals for angles outside that range. The computed angle $\Delta\Theta$ is said to be wrapped. Because of this phenomenon, ESPI is only capable of measuring absolute displacements if there is a fixed point (zero displacement) within the measurement field of view, or if the displacements measured are smaller or equal one wavelength. In some cases, when the displacement progression with time can be observed with a sufficiently large sampling rate, absolute displacements can also be quantified. In general, the standard ESPI is only capable of relative measurements. Rigid body motions such as pure translations that occur in between the acquisition of the reference and deformed states, can't be identified. Rigid body motions also cause phase changes, but they modulate the phase uniformly across the measured region.

For the case of an in-plane ESPI set up, Equation 3-3 shows that the necessary displacement to cause a full 2π phase change is $d = \frac{\lambda}{2\sin\theta}$. Any pure translation in the direction of sensitivity that is larger than the value mentioned will cause the phase to modulate and the total phase change will be

$$\boldsymbol{\Delta\Theta = N_f 2\pi + \frac{4\pi\sin\theta}{\lambda}\left(\frac{n\lambda}{2\sin\theta}\right) = N_f 2\pi + n2\pi} \tag{3-13}$$

where N_f is an integer and $0 \leq n \leq 1$. The only visible phase, or measurable phase in this case, is the phase term correspondent to the term $n2\pi$. Exceptions occur when the sampling rate is fast enough to keep track of the pure translations or when there is really a zero displacement point in the measured region. The main conclusion is that ESPI is a technique that enables differential displacement measurement, such as rotations or deformations where there is a relative displacement point to point in the measured area. Such measurements are important for strain and stress calculation, for example.

Figure 3-4(a) shows the phase map for the reference state of a sample under rotation in the XY plane around the axis Z. The sensitivity direction is in the horizontal pointing to the right. Figure 3-4(b) shows the phase map for the deformed state. It is possible to see that both phase maps before and after deformation present random distribution. On Figure 3-4(c), the phase difference obtained using Equation 3-12 is shown. The fringes represent points of equal displacement in the surface, in this case, horizontal displacement to the right. Points at the top moved to the right relative to points at the bottom, which is characteristic of clockwise rotation.

The saw-tooth characteristic of the phase map is due to the arctangent operation used to retrieve the phase. To obtain a useful phase map, proportional to the displacement map, a process called unwrapping is used. The unwrapping process identifies the phase jumps and either adds or subtracts a multiple of 2π so that the phase map becomes continuous. The unwrapped phase map can be referenced to any point within the measurement because the measurement is relative. This displacement map can then be analyzed or used for subsequent strain-stress calculations.

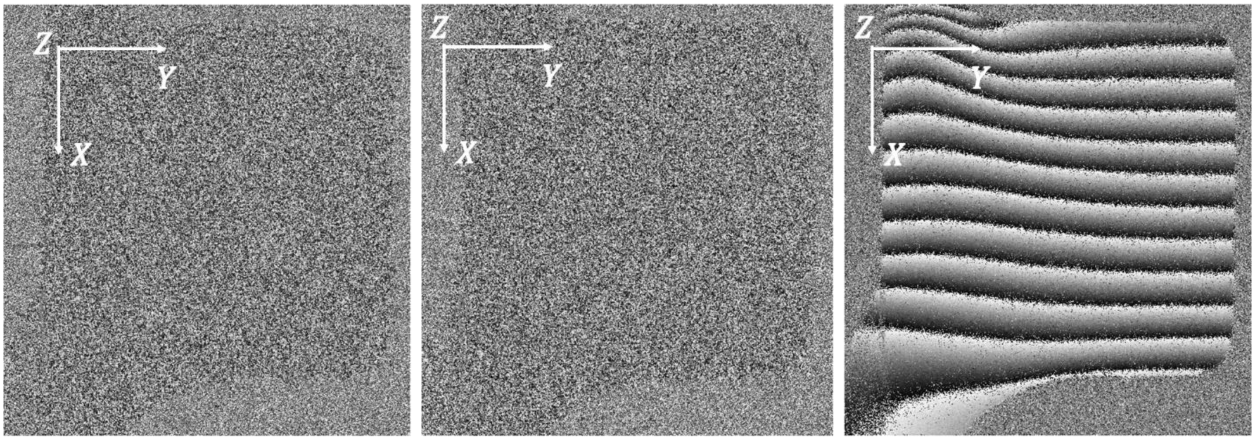

a) Phase before deformation b) Phase after deformation c) Phase difference

Figure 3-4.(a) Phase map measured in the reference state, before deformation. b) Phase map measured after deformation. (c) Phase difference between states before and after deformation.

3.3 Measurement quality influencing factors

There are several factors that affect the quality of a ESPI measurement. The most significant factors relate to the coherence of the light source, the phase stepping accuracy and the visibility of the speckle pattern. External factors such as temperature variations, air currents and vibrations can also introduce noise and artifacts in the measurement.

Lack of coherence is one of the main problems affecting ESPI measurement quality. This problem becomes more evident when the light source has limited coherence length, as in the case of a laser diode. Recalling Equations 2-7 and 2-8, it is clear that the intensity modulation of an interference pattern depends on the relative phase difference between the interfering waves. Furthermore, the phase difference Θ depends on the individual phases of the two waves, ϕ_1 and ϕ_2. From the definition of coherence [32], if the waves interfere with poor phase correlation, i.e., low coherence, the term $\phi_1 - \phi_2$ is not constant with time. There is no good correlation between the individual phases and the phase difference term Θ varies randomly at very high frequencies, independent of the surface motion. The intensity described by Equation 2-7 has its modulation decreased as the interfering term tend to average towards zero due to the fast and random changes of phase, and the average intensity term dominantes over the interference term.

Figure 3-5 shows examples of the variation of light intensity measured at a point or pixel caused by relative phase change between the two beams within an interferometer. Figure 3-5(a) shows the consequence of poor coherence of the beams such that relative phase changes cause very little variation in measured intensity. Figure 3-5(b) shows a different example where the beam coherence was much higher, leading to a much greater variation in measured intensity.

The modulation of a speckle pattern can be evaluated by the concept of visibility [36]. This is the ratio of the amplitude of the sinusoidal intensity variation in Figure 3-5 to the mean intensity. For a set of four $\frac{\pi}{2}$ stepped images, the visibility may be calculated using

$$\mathbf{V} = \frac{2\sqrt{(\mathbf{I_4}-\mathbf{I_2})^2+(\mathbf{I_1}-\mathbf{I_3})^2}}{(\mathbf{I_1}+\mathbf{I_2}+\mathbf{I_3}+\mathbf{I_4})} \tag{3-14}$$

A maximum visibility corresponds to a value $\mathrm{V} = 1$ and a minimum of $\mathrm{V} = 0$. In practice, visibility values above $\mathrm{V} = 0.1$ are minimally sufficient for phase measurement. Figure 3-5(a) shows examples of low visibility - $\mathrm{V} = 0.08$ – and Figure 3-5(b) shows examples of high visibility - $\mathrm{V} = 0.4$. The blue dashed line is the intensity modulation given by Equation 2-7, while the red solid line is the average intensity. The black dots are the intensities as captured when acquiring the images after phase stepping.

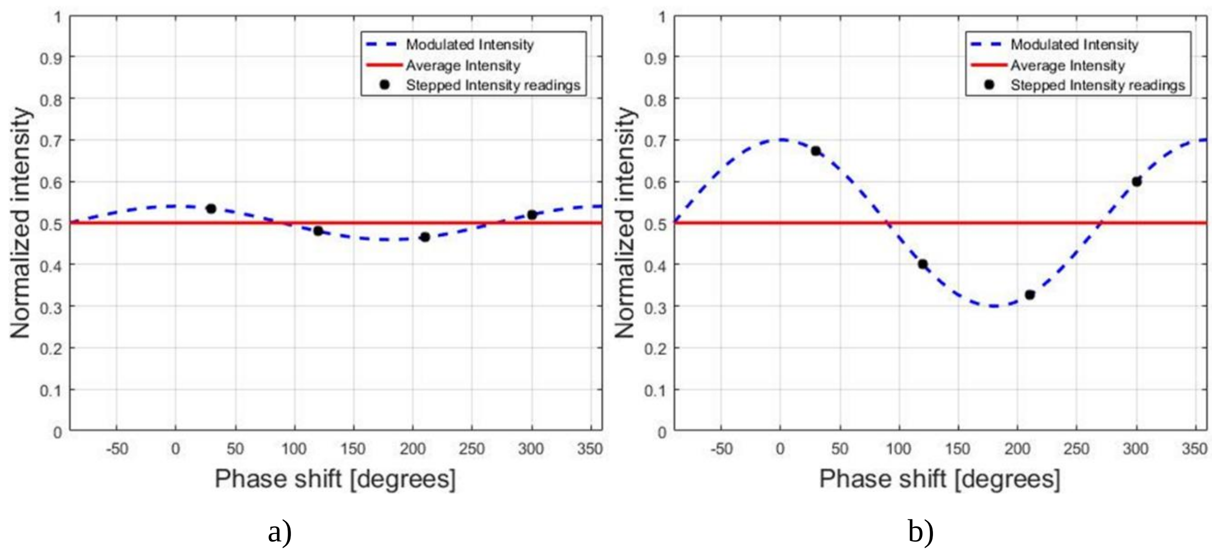

Figure 3-5. Left: Intensity modulation plot of a interference pattern with visibility equivalent to V=0.4. Right: Intensity modulation plot of an interference pattern with visibility equivalent to V=0.08.

Ideally, i.e., without any measurement noise and with perfect phase stepping, both visibilities would be enough to retrieve the phase of every pixel. In reality, the phase stepping is not perfect and the image acquisition is prone to noise – CCD instabilities and inherent noise, vibrations, index of refraction changes, temperature variations. Phase angle evaluation derives from the varying part of the curves in Figure 3-5, the mean amplitude contributes nothing. Thus, for best noise immunity it is desirable to have large sinusoidal amplitude, thus high visibility.

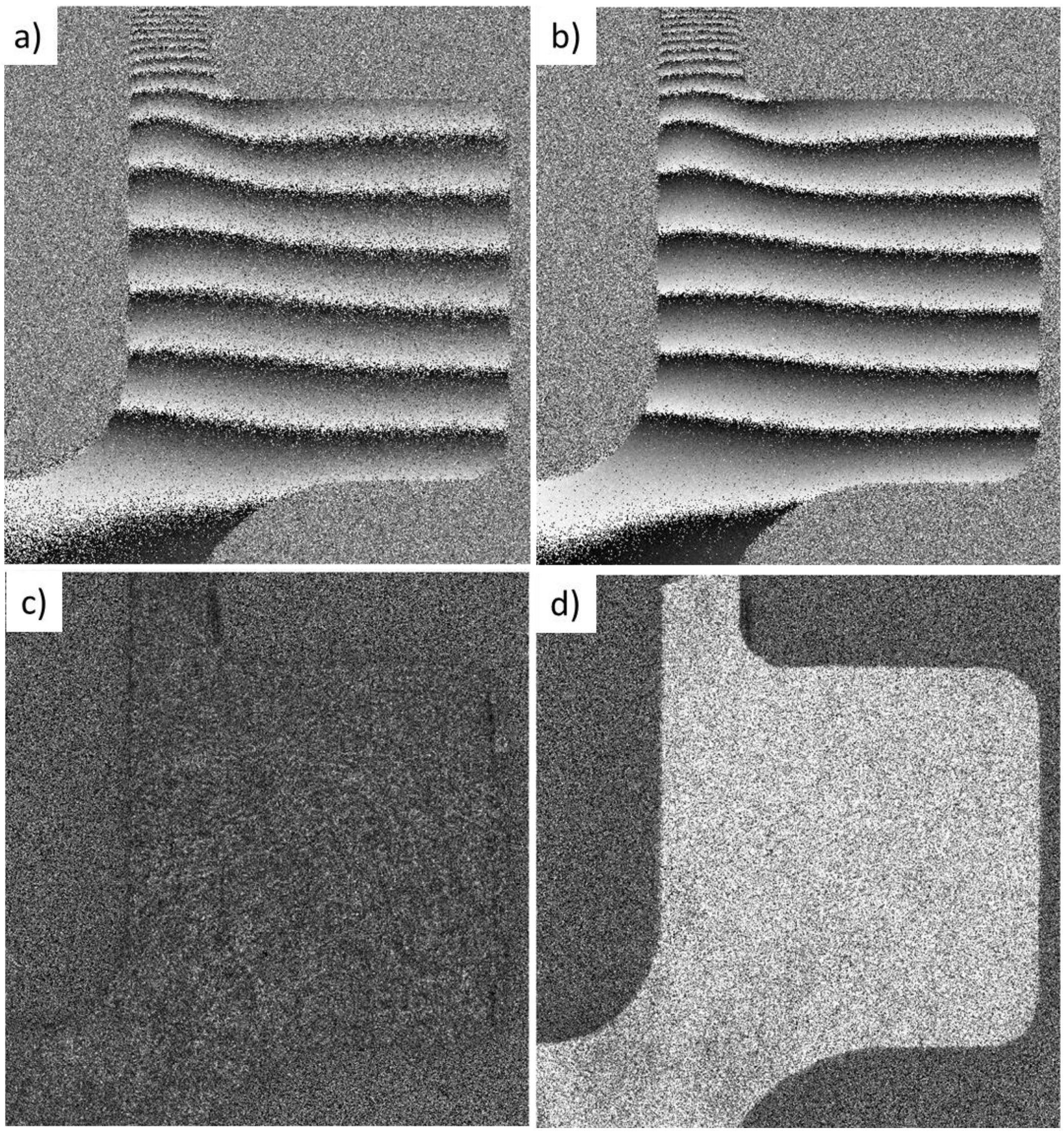

Figure 3-6.(a) Lower visibility ($V \leq 0.2$) phase map. b) Phase map with visibility $V \geq 0.4$. (c)Visibility map of phase map shown in a). (d) Visibility map of phase map shown in b). Dark spots on c) and d) represent points of visibility lower than $V = 0.1$.

Figure 3-6(a) shows an example of a low visibility phase map, as is seen by the graininess within the fringes. Figure 3-6(c) shows a grayscale map of visibility of the phase map seen on Figure 3-6(a), with black corresponding to $V = 0$ and white $V \geq 0.5$. The overall dark grey color indicates a generally low visibility. In comparison, the phase map in Figure 3-6(b) has a much higher visibility, thus having much less grainy fringes and much whiter visibility map, as seen on Figure 3-6(d).

Other problems such as pixel saturation – when the intensity of a pixel is too high and the value recorded by the digital camera is saturated at its maximum possible value independent of phase changes – and speckle size also may affect the overall noise levels and measurement quality. In the case of speckle size – which is driven by the numerical aperture of the lens and the wavelength of the light, the desired size is of one speckle per pixel. Too big speckles reduce the spatial resolution as the calculated phase on reference and deformed states is the same over several pixels. To small speckles, i.e., several speckles within one single pixel, may result in modulation problems as the intensity modulations are averaged out. The optimal condition is when the speckle size matches the pixel size. The pixel size, i.e., the area in the measured field that is represented in the image by one pixel, is given by the camera lens magnification. The pixel size can be measured using features in the image with a known size. The aperture used for speckle size matching depends on the pixel size, and for a pixel of length/width of $45\mu m$, the aperture used is F8.

Chapter 4: Diffraction Grating Interferometer for 3D ESPI Measurements

The standard configuration used in ESPI splits the light from a coherent source into two or more beams to make them interfere two at the time, at the specimen surface or at the CCD. Phase information can be obtained regarding the surface state. The usual way of splitting the light is by a beam splitter.

In Chapter 3, the ESPI configuration presented used a cubic beam splitter. Part of the beam was transmitted and part was deflected at 90°. Two mirrors were then used to join the beams at the surface, with incidence angles of 45°, resulting in an in-plane sensitivity arrangement.

While being simple components, beam splitters are usually bulky and their use in a double illumination interferometer with in-plane sensitivity arrangement may pose some problems related to coherence because of the associated path length differences. In addition, the use of a beam splitter requires the phase shifting to be performed at one of the mirrors in the arrangement. For a multi-axis configuration, there would be a need for stepping more than one mirror, which increases the number of actuators and complexity of the assembly.

Diffraction gratings are a practical alternative to beam splitters. They have the advantage of being compact and simple while solving the problem of coherence mentioned before. To explain the advantages of diffraction gratings over beam splitters, the concepts of wavefronts and time fronts is presented in the next section.

4.1 Wavefronts and time fronts

The light emitting from a coherent source such as a laser has a consistent phase. The name wavefront is given to the set of points that share the same phase within the beam. The wavefront propagates at the speed of light in the medium, in the direction of the wavevector k, and can be diffracted, refracted or reflected.

Time front is the name given to a set of points in the light beam that were generated at the same time. They propagate the same optical distance in a time δt.

Time fronts and wavefronts are coincident at the origin or source. They propagate through a homogenous medium and are reflected and refracted under the same rules. In the case of a beam splitter, both wavefronts and time fronts are transmitted and reflected with the same angles. The implications of the interaction of time fronts and wavefronts with splitting elements such as beam splitters and diffraction gratings enables a discussion of equal path length and unequal path length interferometers.

4.2 Equal path length and unequal path length interferometers

Figure 4-1 shows an example of time fronts and wavefronts propagation though a beam splitter. Looking at both boundaries of the beam, rays A and B, it is possible to see that both rays are transmitted unaltered though the beam splitter, becoming a1 and b1, and the corresponding beams a2 and b2 are reflected at the partial mirror within the splitter. After mirrors 1 and 2, the beams meet again at the specimen's surface. Notice that there is a geometric inversion of the rays, since the lower arm has experienced two reflections while the upper arm experienced only one reflection at mirror 1. Therefore, ray a1 interferes with ray b2, and ray b1 with ray a2.

The time fronts and wavefronts, represented by the green dotted line and the purple dashed line respectively, are transmitted and reflected in the same way. In addition to the inversion, there is a path length difference across the overlapping region

$$\mathbf{-hsin\theta \leq \delta_{pl} \geq hsin\theta} \tag{4-1}$$

where θ is the illumination angle and h is the width of the illumination area. The path length difference δ_{pl} varies linearly with h and is zero for $\mathrm{h}/2$ as seen in Figure 4-2. The cause for this path length difference is the fact that the time fronts arrive at the surface with relative angle

$$\boldsymbol{\vartheta = 2\theta} \tag{4-2}$$

Figure 4-1 shows an example of an unequal path length interferometer. The implications are drastic if the laser lacks the necessary coherence length. In the case of a laser diode, which has very limited coherence length of just a few millimeters and presents repeated coherence bands, there will be regions of high coherence and low coherence within the illuminated area.

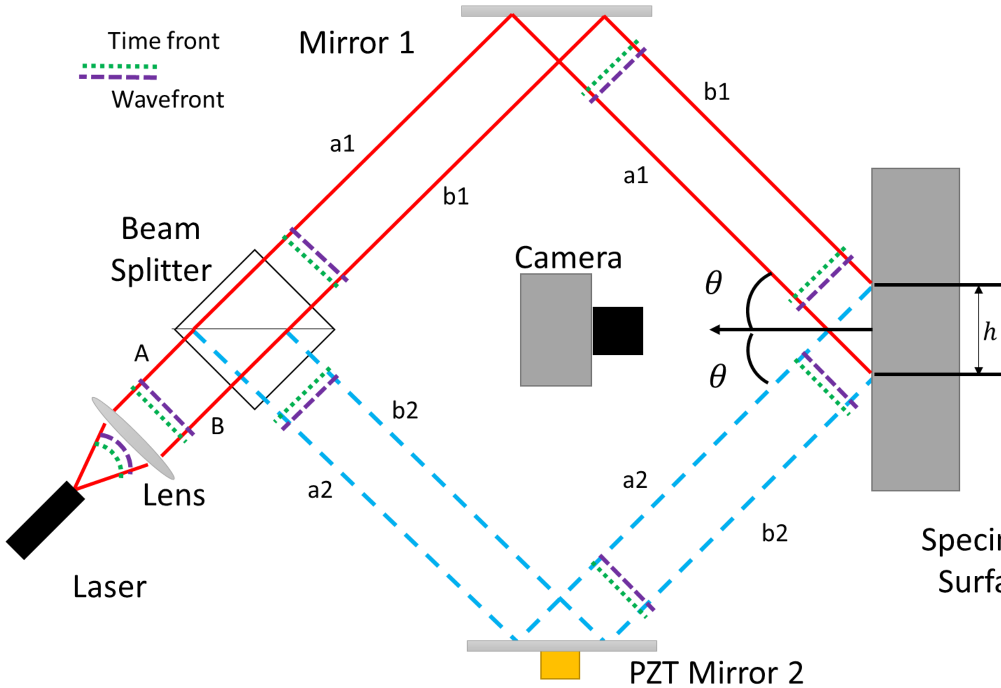

Figure 4-1. ESPI configuration with a cubic beam splitter. The time fronts and wavefronts are shown separate for convenience. The extra reflection on the lower arm of the interferometer causes an inversion of the rays and the relative angle of the time fronts from the two arms is responsible for a path length difference at the illuminated area.

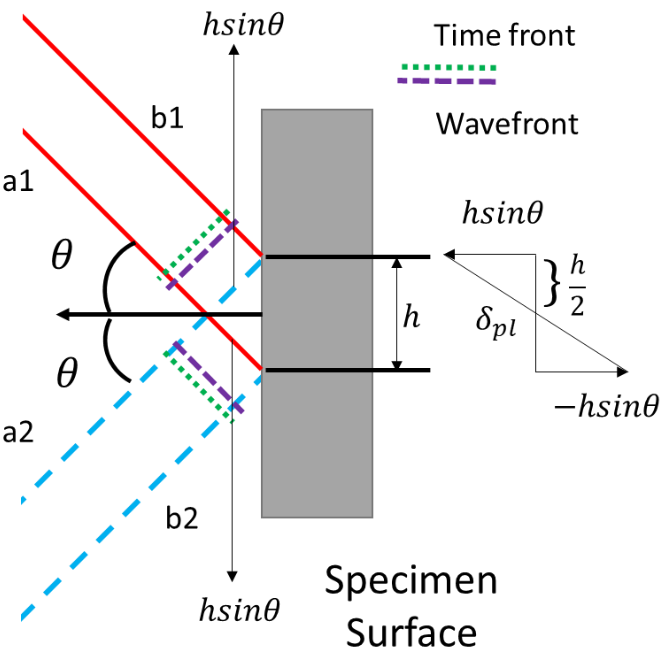

Figure 4-2. Time fronts arrive at the surface with a relative angle and cause a differential path length difference in the illuminated area.

The effect of the path length difference can be seen in terms of visibility, as shown in Figure 4-3(a). for the case of a sample measured under compression using an in-plane ESPI arrangement. From previous discussions, it was stated that lower visibility affects the measurement quality, which can also be seen in Figure 4-3(b). In the case of Figure 4-3, the light source used is a laser diode with coherence length of 1.5mm and the ESPI arrangement had a beam splitter as splitting element.

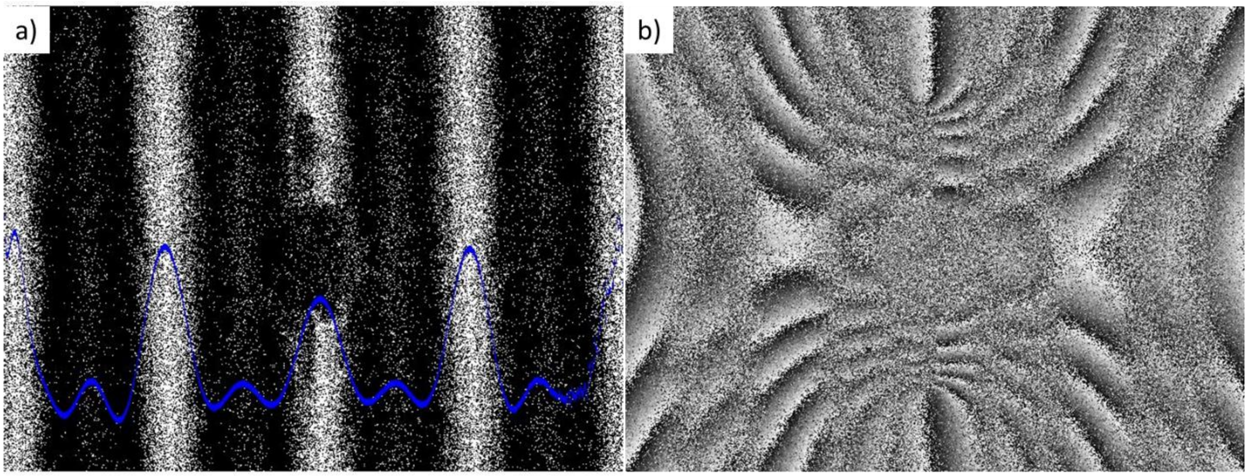

Figure 4-3.(a) Visibility map of a sample measured under deformation measured with an in-plane ESPI arrangement using beam splitter. White pixels have visibility values higher then 0.1. The blue line is the column average of visibility for the image. b) Phase map of the deformed surface and the effect of low visibility due to the path length difference problem. (Data courtesy of J. Heikinnen)

Unlike a beam splitter, which reflects and transmits the original wavefront and time fronts in the same manner, a diffraction generates new wavefronts by superposition of intensity patterns, but does nothing to the time fronts. This effect can be seen in more detail on Figure 4-4. The beam splitter is replaced by the diffraction grating and the diffraction orders 1 and -1 are used for interference at the surface. The order zero is just blocked and not used, so for simplicity is not shown. The angle of diffraction is defined by Equation 2-9 and corresponds to the rotation of the wavefronts. On the other hand, the time fronts remain parallel to the original time front prior the diffraction grating. It is easy to see that the distance δl that the rays a1 and b1 travel is the same, and the time front remains unaltered. The same is true for the time fronts of the lower arm.

Both wavefronts and time fronts are propagated and reflected at mirrors 1 and 2 under the same circumstances. The time fronts arrive parallel at the surface, eliminating the path length difference. In addition, ray A is split into rays a1 and a2, which subsequently interfere at the surface while having travelled the same optical distance. The same occurs with ray B and diffracted rays b1 and b2. This configuration is called equal path length arrangement and has the advantage of reducing the need for a high coherence source. Yet on Figure 4-4, the PZT appears at the grating. One of the interesting features enabled by the grating is the phase stepping by grating translation. This concept is explored in the next section.

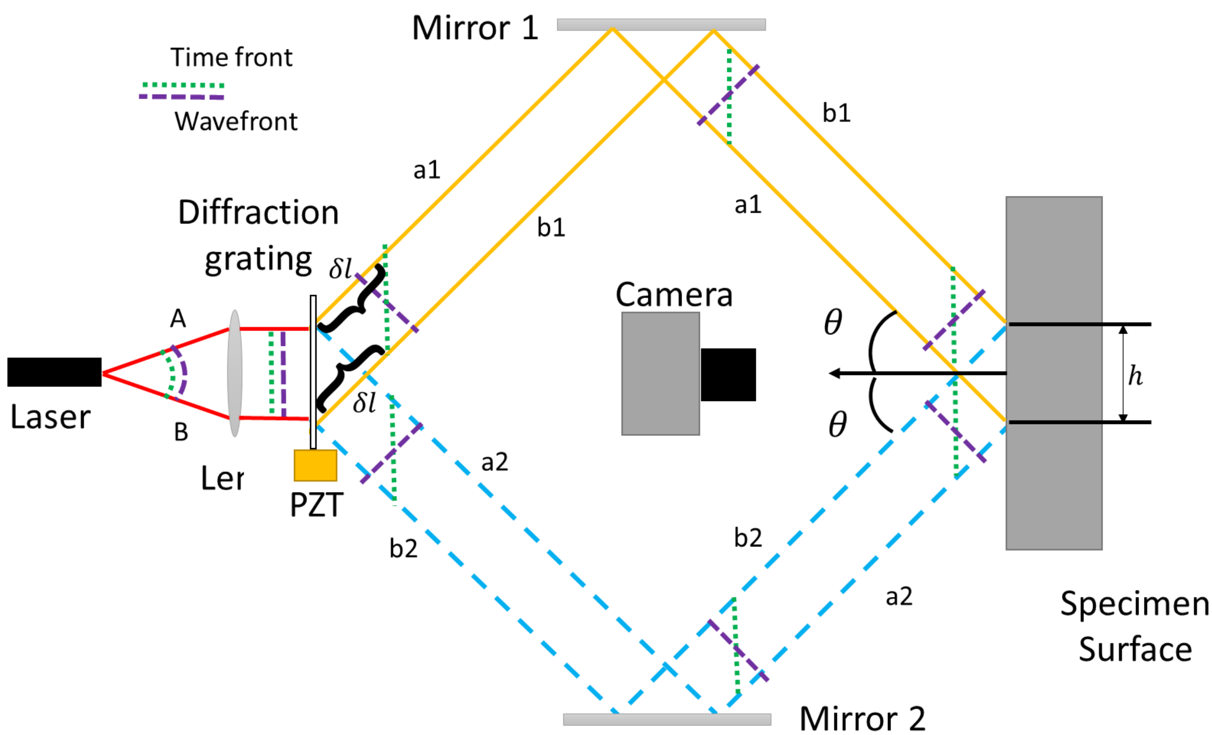

Figure 4-4. Diffraction grating ESPI arrangement for in-plane sensitivity. The time fronts and wavefronts are shown. The time fronts arrive parallel to each other at the surface.

4.3 Grating based phase stepping

The next advantage of diffraction gratings over beam splitters is the possibility of design simplification when splitting the original beam more than once. There is also a possibility of reducing the number of actuators necessary for phase stepping.

Splitting a light beam twice using beam splitters, for example, might require several mirrors and beam splitters, which increases the complexity of the whole assembly. For a dual-axis configuration, i.e., with two independent in-plane sensitivity arrangements, there is also the necessity of 4 mirrors – if the arrangement is based on the Mach-Zehnder configuration – for directing the beams to the surface, 2 of which need to be equipped with PZTs for phase shifting. Usually, the mirrors are large and require 4 PZTs, one at each corner, to achieve a smooth and uniform motion. In the case of the configuration proposed in this work, it would be necessary to have at least 3 of the 4 mirrors equipped with PZTs, for a total of 12 actuators.

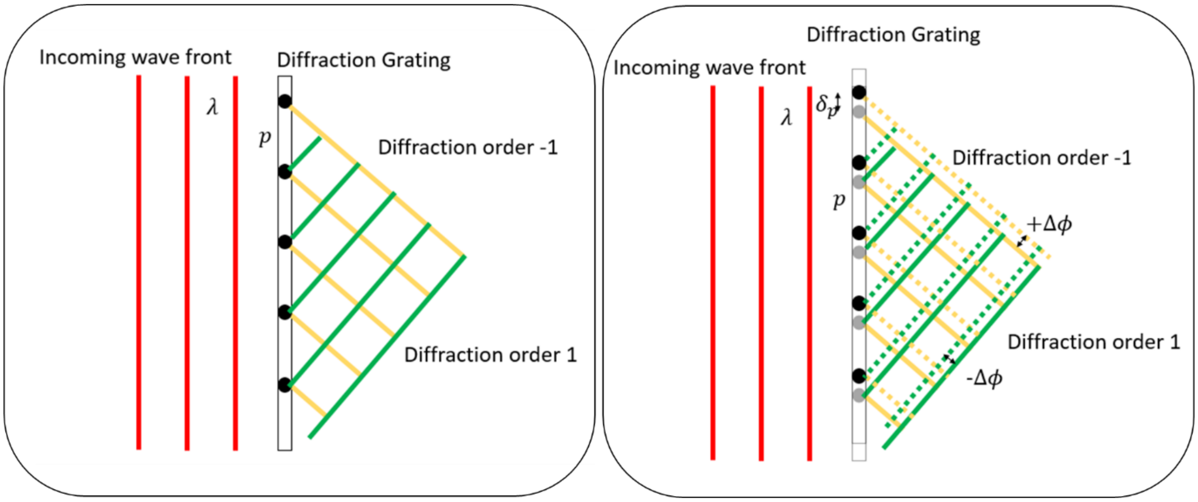

Figure 4-5. Left: Diffraction grating cross section showing incident and diffracted waves. Right: Upwards translation of the grating induces a phase shift in both beams. Order -1 has its phase advanced while order 1 has its phase delayed.

Instead of moving the mirrors back and forth, translating the grating can be a more convenient way of introducing a phase shift. Figure 4-5(a) shows a cross section of a diffraction grating with spacing p and an incoming beam of wavelength λ. The wavefronts are shown as straight lines. Past the grating, the orders of diffraction 1 (green) and -1 (yellow) are shown. The order zero is hidden for simplicity. Figure 4-5(b) shows the same grating displaced upwards by an amount δ_p. It is possible to see that the order -1 has its phase advanced, which is represented by the yellow dashed line, while the order of diffraction 1 has its phase delayed, the dashed green line. The amount of displacement necessary for a complete 360° phase shift in a specific beam is $\delta_{360} = p$. Therefore, for a 90° phase shift, the necessary translation is of the order of $\delta_{90} = \frac{p}{8}$ since one beam will be advanced by 45° while the other one is advanced by -45°.

The relation of motion and phase shift is linear as shown below

$$\boldsymbol{\Delta\phi = \frac{2\pi\delta_p}{p}} \qquad (4\text{-}3)$$

where p is the grating line spacing. Notice that the phase stepping is completely independent of the wavelength of light.

4.4 Dual Diffraction Grating Assembly for Multi-Axis 3D Interferometer

The usual approach for an ESPI interferometer capable of 3D measurements is to use multiple out-of-plane arrangements [37] or to combine in-plane arrangements with a separate reference beam [24] to create the out-of-plane sensitivity. These arrangements can get very complicated.

The arrangement proposed in this work uses a dual-grating based system. The gratings have different line spacings and can be stacked one on top of the other to split the original beam into 2 pairs of beams with different diffraction angles. Each pair of beams is then used in an in-plane arrangement with different sensitivity. A convenient combination of the beams from the in-plane arrangements yield up to 4 extra sensitivity vectors with a mix of in-plane and out-of-plane components.

For case of analysis, the following Cartesian coordinates are defined as a reference. The four incident beams are shown as blue and red arrows in Figure 4-6.

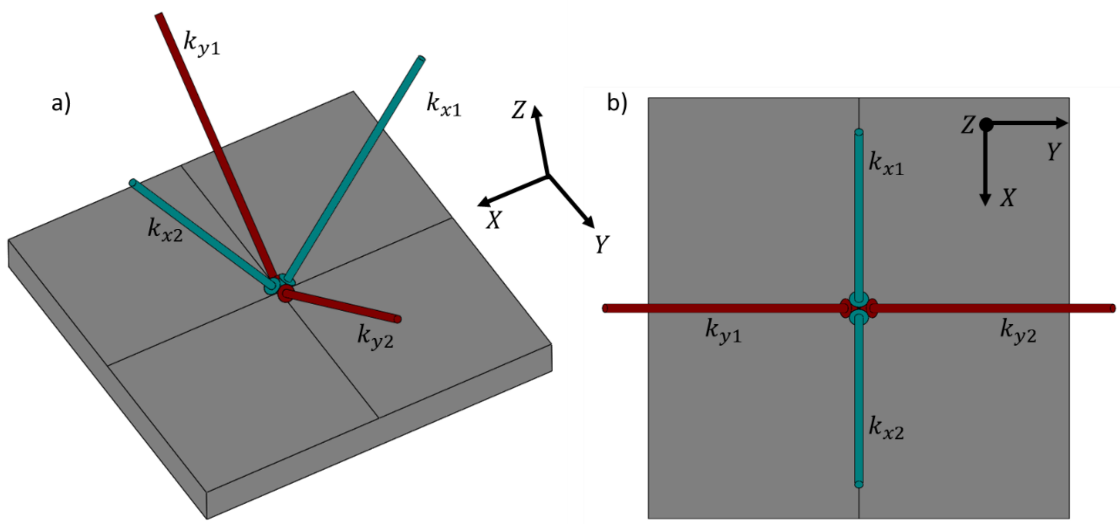

Figure 4-6.(a) Perspective view of the incident beams. b) Top view of the incident beams. The incident beams are represented by their wavevectors and labeled according to the plane of incidence. Beams with index 1 are incident in the positive direction of the respective axis.

4.4.1 In-plane Configuration 1– Sensitivity in X Direction

For the arrangement with sensitivity in the X direction, a grating with 830lines/mm and spacing $p_x = 1.2\mu m$, was chosen. The angles of diffraction are given by Equation 2-9 and for a wavelength of $\lambda = 0.66\mu m$, $\theta_1 \cong 33.2°$.

The sensitivity has a magnitude and direction given by the equation

$$\mathbf{K_x} = \mathbf{k_{x1}} - \mathbf{k_{x2}} = \frac{4\pi\sin\theta_1}{\lambda}\hat{\mathbf{x}} = \frac{4\pi}{p_x}\hat{\mathbf{x}} \tag{4-4}$$

where $\hat{x}$ is a unitary vector pointing in the direction of positive X. Equation 4-4 indicates that the arrangement is independent of the wavelength λ. The magnitude of the sensitivity vector is $|K_x| \cong 10.5 rad/\mu m$. This magnitude produces one fringe in the phase map for every $0.6\mu m$ of displacement in the X direction.

4.4.2 In-plane Configuration 2 – Sensitivity in Y Direction

The arrangement with sensitivity in the Y direction uses a diffraction grating of 1200lines/mm (spacing $p_y = 0.833\mu m$). The diffraction angle, as per Equation 2-9, is shown to be $\theta_2 \cong 52.4°$ for $\lambda = 0.66\mu m$. The sensitivity vector in the Y direction has the form

$$\mathbf{K_y} = \mathbf{k_{y1}} - \mathbf{k_{y2}} = \frac{4\pi\sin\theta_2}{\lambda}\hat{\mathbf{y}} = \frac{4\pi}{p_y}\hat{\mathbf{y}} \tag{4-5}$$

where $\hat{y}$ is a unit vector pointing to the direction of positive Y. This arrangement has larger sensitivity compared to the one in X as $p_y < p_x$. The modulus of the vector is $|K_y| \cong 15.1 rad/\mu m$, equivalent to two fringes for every $0.833\mu m$ of relative displacement in the Y direction.

Figure 4-7(a) shows an isometric view of both in-plane sensitivity vectors. Figure 4-7(b) andFigure *4-7*(c) show the same vectors, but with a frontal view. Notice that the wavevectors have the same magnitude for both axes but the incidence angle makes K_y larger than K_x. The difference in angles of incidence of both X and Y in-plane arrangements is the key factor required to obtain the out-of-plane measurements, as it will be shown in future sections.

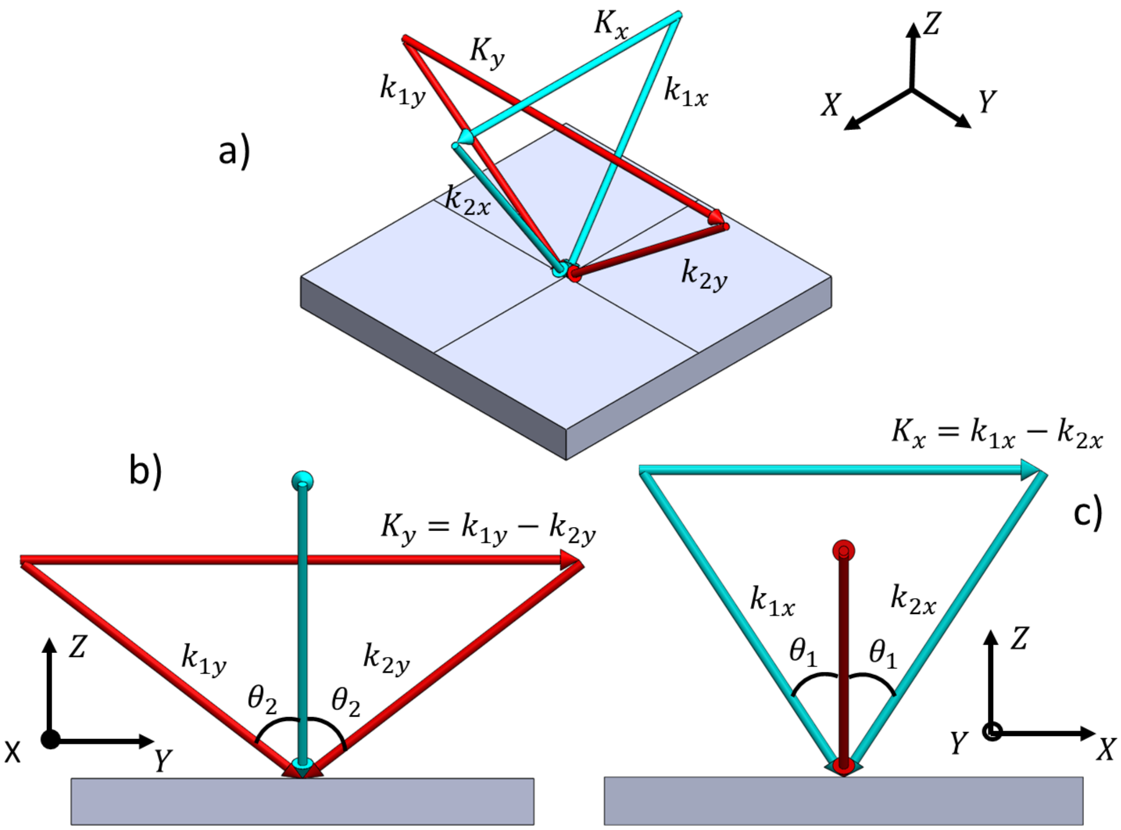

Figure 4-7.(a) Isometric view showing the incoming wavevectors, represented by red and blue arrows. The sensitivity vectors are parallel to the surface plane and result from vectorial subtraction. b) Frontal view of the sensitivity vector in Y. (c) Frontal view of the sensitivity vector in X.

4.4.3 Out-of-Plane Arrangements – Cross Combination of In-Plane Arrangements

The two diffraction gratings were chosen to be different so the in-plane sensitivities in X and Y are also different as per Equations 4-4 and 4-5. When a beam of the X in-plane arrangement is combined with a beam of the Y in-plane arrangement, the resultant sensitivity is in the diagonal in-plane with a component that is out-of-plane, pointing down or up in the Z direction, due to the different incidence angles of the beams.

Consider beam k_{x1} from the X direction interfering with beam k_{y2} of the Y direction. The sensitivity vector for this arrangement is as shown below and labeled as K_4 for simplicity

$$\mathbf{K_{x1\rightarrow y2}} = \mathbf{K_4} = \mathbf{k_{x1}} - \mathbf{k_{y2}} = \frac{2\pi}{\lambda}(\sin\theta_1\hat{\mathbf{x}} + \sin\theta_2\hat{\mathbf{y}} + (\cos\theta_2 - \cos\theta_1)\hat{\mathbf{z}}) = 2\pi\left(\frac{1}{p_x}\hat{\mathbf{x}} + \frac{1}{p_y}\hat{\mathbf{y}}\right) + \frac{2\pi}{\lambda}(\cos\theta_2 - \cos\theta_1)\hat{\mathbf{z}} \quad (4\text{-}6)$$

The resulting sensitivity vector has a diagonal in-plane component that is independent of λ under ideal circumstances (perfect alignment), and the out-of-plane component is pointing down in the Z direction as $\theta_2 > \theta_1$ makes $cos\theta_2 - cos\theta_1 < 0$. The out-of-plane component, however, is not independent of λ, independently of the alignment. The sensitivity out-of-plane has a phase to displacement ratio equivalent to $1.42\ rad/\mu m$, or one fringe for every $2.92\mu m$ of displacement in the Z direction.

On Figure 4-8(a), an isometric view shows the combination of wavevectors k_{x1} and k_{y2} to give form to the sensitivity vector labelled as k_4. Figure 4-8(b) shows a top view of this vectors, where the diagonal in-plane component is evident. Figure 4-8(c) shows that k_4 has an out-of-plane component pointing downwards.

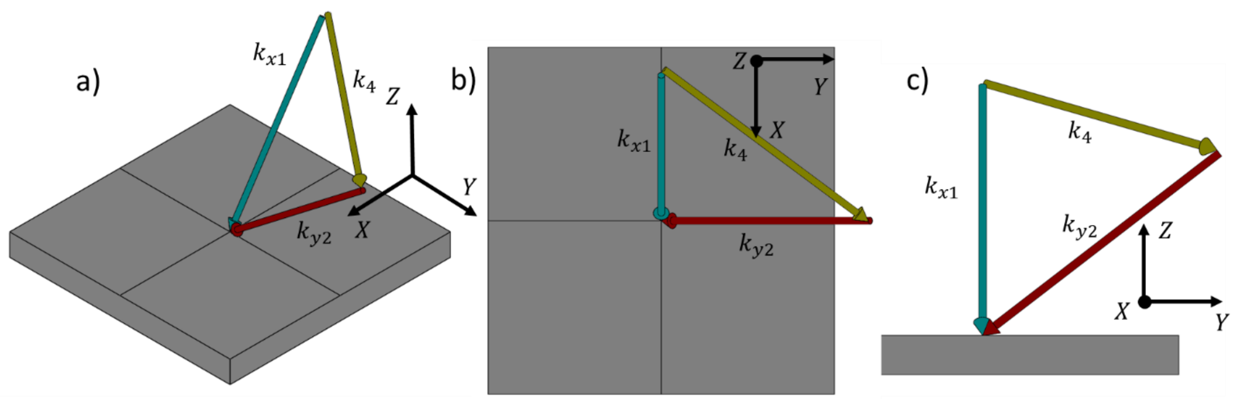

Figure 4-8.(a) Isometric view showing the incident wavevectors and the combined sensitivity vector k_4 (yellow). b) Top view sowing the diagonal in-plane component of k_4. (c) Front view showing the out-of-plane component of k_4, which points downwards in Z.

The sensitivities for the other 3 remaining axes are provided below

$$\mathbf{K_{y2\rightarrow x2}} = \mathbf{K_3} = 2\pi\left(\frac{1}{p_x}\hat{\mathbf{x}} - \frac{1}{p_y}\hat{\mathbf{y}}\right) + \frac{2\pi}{\lambda}(\cos\theta_1 - \cos\theta_2)\hat{\mathbf{z}} \quad (4\text{-}7)$$

$$\mathbf{K_{x1\rightarrow y1}} = \mathbf{K_5} = 2\pi\left(\frac{1}{p_x}\hat{\mathbf{x}} - \frac{1}{p_y}\hat{\mathbf{y}}\right) + \frac{2\pi}{\lambda}(\cos\theta_2 - \cos\theta_1)\hat{\mathbf{z}} \quad (4\text{-}8)$$

$$\mathbf{K_{y1\to x2} = K_6 = 2\pi\left(\frac{1}{p_x}\hat{x} + \frac{1}{p_y}\hat{y}\right) + \frac{2\pi}{\lambda}(\cos\theta_1 - \cos\theta_2)\hat{z}} \tag{4-9}$$

Notice that the sensitivity vectors k_3 and k_6 have their out-of-plane component pointing upwards in Z as $cos\theta_1 > cos\theta_2$. On the other hand, similar to k_4, k_5 points downwards in Z. The geometry can be worked out by analyzing the phase stepping direction and the incidence angles of the incident wavevectors, and was also confirmed experimentally with a known displacement as it will be discussed in Chapter 6.

Figure 4-9(a) shows an isometric view of all of the 6 sensitivity arrangements, with labels on the composed sensitivity vectors. Figure 4-9(b) shows a top view of the vector configurations. Notice that, based on Figure 4-9(a), Figure 4-9(b) and Figure 4-9(c), k_3 and k_5 point in the same diagonal direction but k_3 has positive sensitivity in the Z direction while k_5 has negative sensitivity in Z. Similarly, k_4 and k_6 share the diagonal direction but point in opposite directions - k_4 points down while k_6 points up, in the Z axis. Vectors with directions and indication of out-of-plane sensitivity direction.

By combining the beams in different ways it is possible to obtain 6 different measurements. This important feature opens the possibility for checking the measurement as there is redundant data. In addition, the redundant data can be used for averaging, which can increase the accuracy, reduce the noise and increment the quality of the measurement.

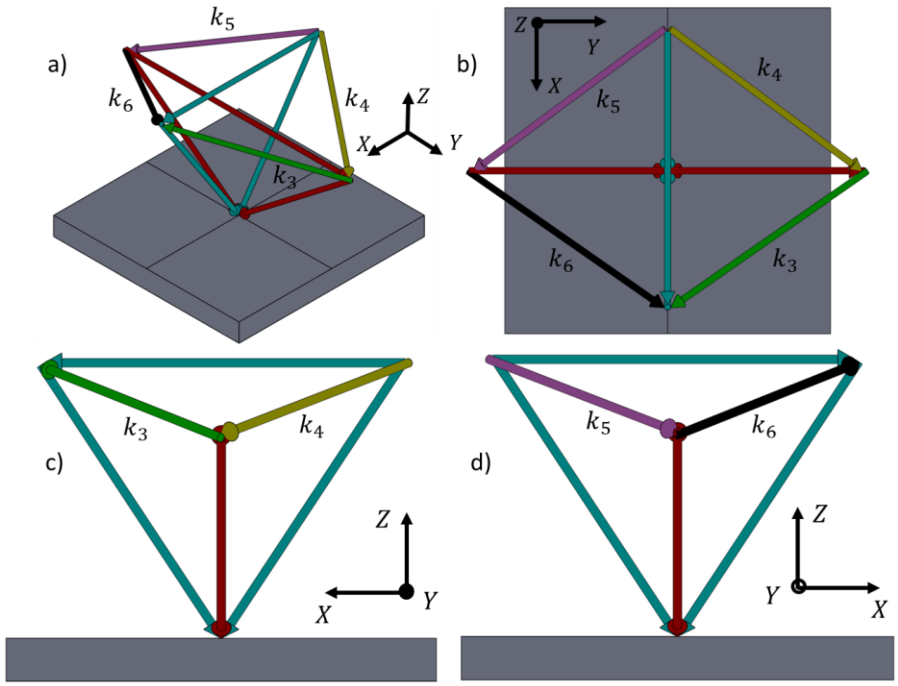

Figure 4-9.(a) Isometric view showing all the out-of-plane and in-plane arrangements. b) Top view showing the diagonal directions of the composed vectors. (c) Frontal view showing the Z directions of k_3 and k_4. (d) Lateral view showing the Z directions of k_5 and k_6.

For all the six different measurements, the phase stepping is always done moving one of the PZTs attached to the grating structure. A detailed view on the design and assembly of a portable device using the concept described above is presented in the next chapter.

Chapter 5: Design and Construction

Based on the arrangement proposed on Chapter 4, a device was designed that is capable of taking measurements in an automatized way. The next sections of this chapter present some preliminary but important steps and features of the design, such as the laser, lens system and diffraction grating assembly concept. Later in the chapter, a detailed view of these concepts is shown integrated into the design. Finally the construction steps are briefly presented.

5.1 The laser system

The laser used in the system is a laser diode, single transverse mode, operating with a nominal wavelength $\lambda = 660$nm when at a temperature of 25°C. The nominal current is 170mA for a power output of 120mW. The characterization of coherence, effect of current and temperature is important. Before going into details of the mount design, it is necessary to provide some information about the laser's characteristics.

5.1.1 Coherence length and interval

A Michelson interferometer was used to measure the coherence length and the coherence interval. The laser beam was split into two beams with a cubic beam splitter and two mirrors, one of which was mounted on a micrometer stage. By varying the position of the mirror, one beam experienced a path length change and the interference pattern seen at the screen changed. The fringes observed are due to the mirror surface small curvatures, and the contrast of these fringes can be related to the coherence through a measure of contrast. Figure 5-1(a) shows the Michelson arrangement used to observe the interference between the beams. In Figure 5-1(b), the contrast of the fringes is high. This measurement was made while the path length difference between both beams was almost zero, i.e., within the coherence length. Figure 5-1(c) shows the same interference pattern but outside the coherence region. The effect of low coherence in the modulation of fringes, or simply visibility, is very clear.

Figure 5-2 shows a plot of the contrast as a function of the mirror displacement. The coherence interval, i.e., the path length difference to which two beams from the same source recover the phase correlation (temporal coherence), was measured to be $\mathrm{H} \cong 12.6$mm and the coherence length measured at FWHM was estimated at $\mathrm{l_c} = 1.25$mm. Notice that these values are twice the spacing shown in the graph since path length difference introduced by the moving mirror is $\delta_{pl} = 2\Delta_{pl}$. These measurements are in accordance with previous results obtained by Schajer et.al. [33] for the same type of laser.

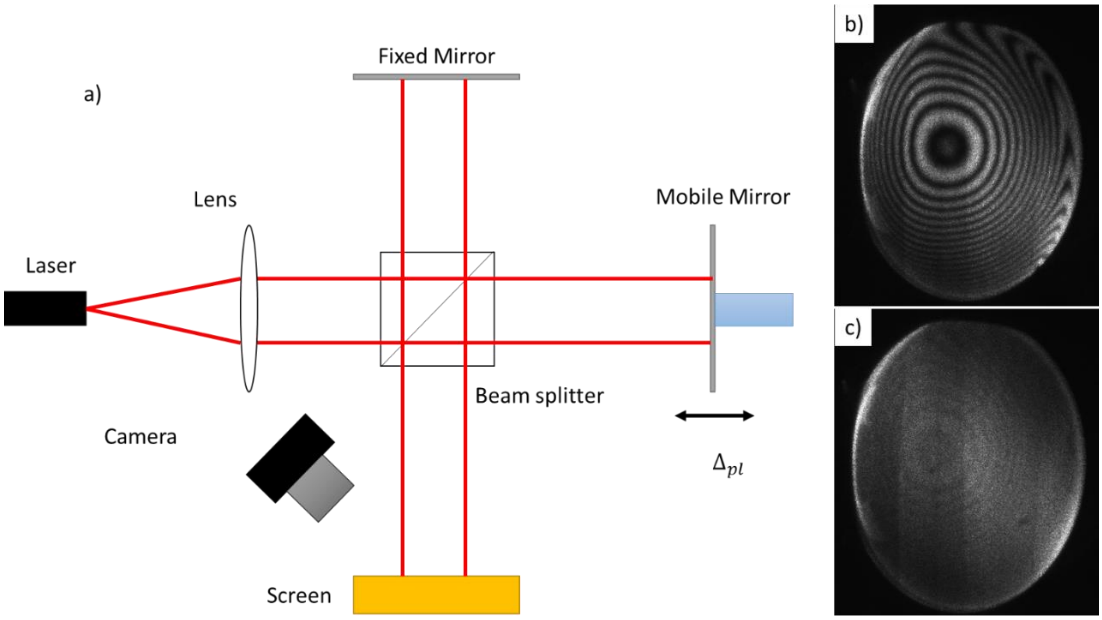

Figure 5-1.(a) Michelson arrangement used for measuring the coherence.(b) High contrast fringe pattern of interference within coherence limits. (c) Low contrast fringe pattern due to interference outside the coherence limits.

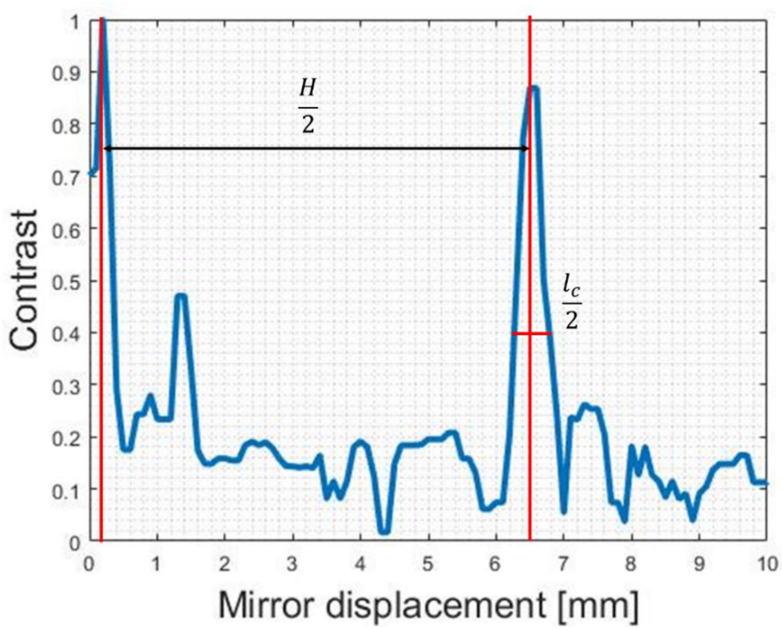

Figure 5-2. Plot of contrast vs mirror displacement. The coherence intervals are visible and the coherence length can be estimated at FWHM.

5.1.2 Coherence and current relation

Drive current has a very high influence on laser behavior, as it can be seen by the plot of visibility vs. current on Figure 5-3. As the current of the laser is changed, peaks of high visibility corresponding to high coherence alternate with points of low visibility or coherence. This feature is important because it shows that there are some specific currents and temperatures at which the laser operates with high coherence. The current is kept constant at 120mA using a low noise driver and the laser outputs approximately 60mW of power.

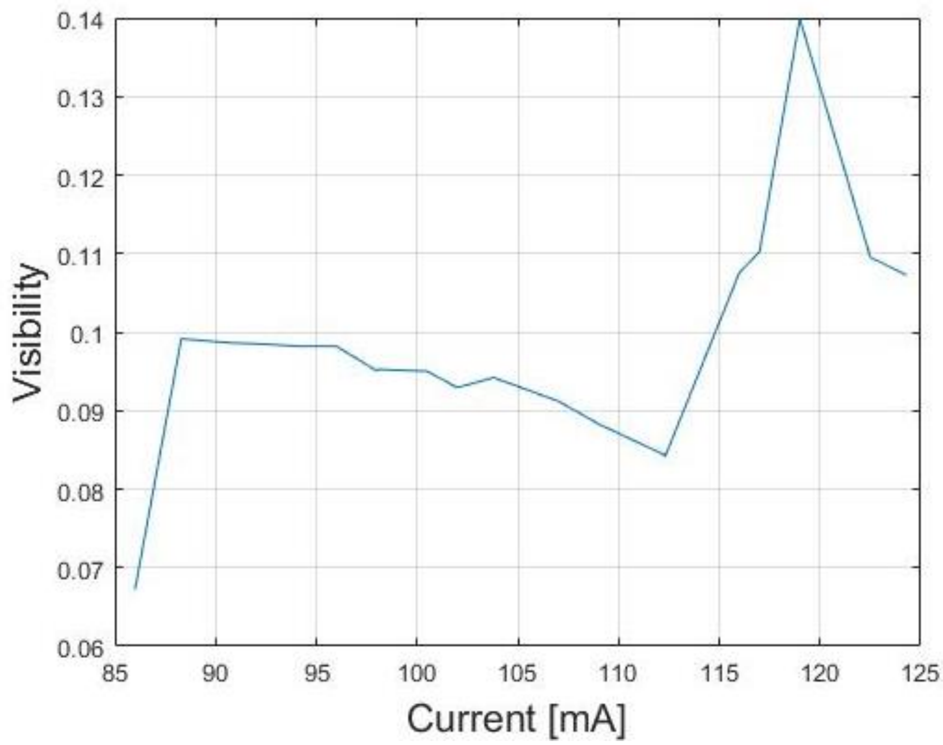

Figure 5-3. Visibility distribution as a function of current. The temperature in the room at the time of the measurement was 22.1°C. There was no temperature control. A peak of visibility was found at a current of approximately 120mA.

The temperature is another important parameter for the stability of the laser. Changes of temperature over time can cause mode hopping of the laser, which causes instability and reduces de coherence drastically. A PID controller integrated with a thermoelectric cooler are used to keep the laser at a constant temperature. More details about the temperature control system will be given in later sections.

5.1.3 Beam divergence and lens system

The divergence angle of the beam is dependent on the cavity geometry. The cavity in this type of laser diode is rectangular and the divergence of the beam in the axis parallel to the shortest dimension of the cavity cross section is considerably higher than in the other direction. Therefore, the beam has an elliptical distribution of power.

Despite the elliptical distribution, the laser mount has a fixed circular aperture and the beam a circular shape. In the case of the proposed system, the laser divergence after the aperture was measured to be 30°. This divergence is not enough to give a good measurement area size. A lens system was then designed to expand the beam further and subsequently collimate it.

A double concave lens of focal length $f_1 = -240$mm was chosen to expand the beam. A second lens was then used to collimate the beam. The collimation lens is a double convex lens of diameter of 65mm and a focal length $f_2 = 70$mm. Matrix optics was used to determine the lenses position and the distances for a stipulated measurement area of diameter 45mm. Figure 5-4 shows schematics of the laser's ray tracing with the lenses and some relevant dimensions.

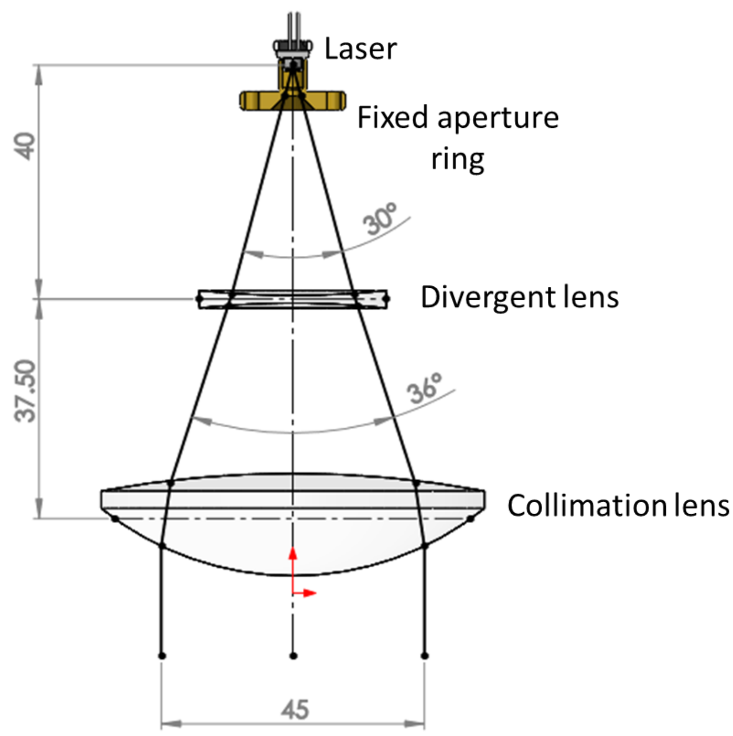

Figure 5-4. Lens assembly used to expand and collimate the laser beam.

5.2 Diffraction grating assembly

To split the incoming beam, the diffraction gratings $\mathrm{g_x}$ and $\mathrm{g_y}$, with line spacing $\mathrm{p_x}$ and $\mathrm{p_y}$, are assembled one on top of the other as shown schematically on Figure 5-5. The gratings used are of the transmission type, with an efficiency that is wavelength dependent. Figure 5-6 shows a graphic with the efficiencies of both gratings. The efficiency plot for the $\mathrm{g_x}$ is shown in pink color and the one for $\mathrm{g_y}$ is shown in green color. For the nominal wavelength of 660nm, the absolute efficiencies, i.e., including all orders of diffraction, are approximately 27% and 15% for $\mathrm{g_x}$ and $\mathrm{g_y}$, respectively. The efficiency refers to the portion of the incident light that is diffracted, with the remaining being transmitted.

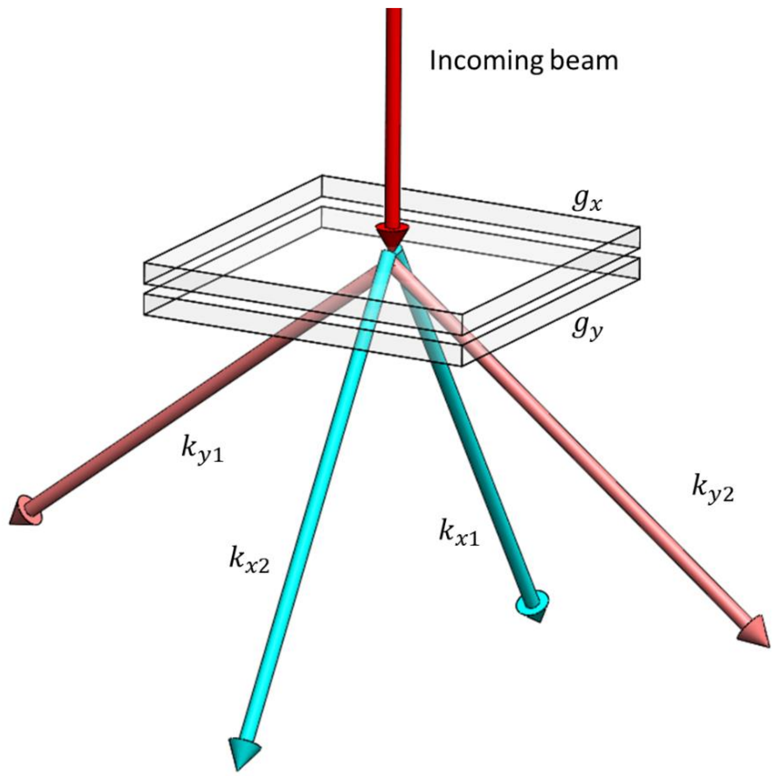

Figure 5-5. Diffraction gratings $\mathrm{g_x}$ and $\mathrm{g_y}$ stacked on top of the other to split the beams into 4 main beams. The secondary beams and the reminiscent beam that Is transmitted through both gratings are not shown for simplicity.

The efficiencies of $\mathrm{g_x}$ and $\mathrm{g_y}$ are then $\mathrm{e_x} = 0.27$ and $\mathrm{e_y} = 0.15$ respectively. The incoming light has a normalized intensity $\mathrm{I_{inc}} = 1$. Assume that the gratings are assembled one on top of the other, like on Figure 5-5 with g_x facing the incoming light before g_y. The transmitted and diffracted intensities after g_x are then

$$\mathbf{I_{t_{g_x}} = I_{inc}(1 - e_x) = 0.73} \tag{5-1}$$

$$\mathbf{I_{dif_{g_x}} = \frac{I_{inc}e_x}{2} = 0.135} \tag{5-2}$$

Equation 5-2 represents the relative intensity of one of the first orders of diffraction, and that explains the ½ factor. Based on Equation 5-1, the incoming beam intensity on g_y is $I_{t_{g_x}}$. The transmitted and diffracted ratios after g_y are

$$\mathbf{I_{t_{g_y}} = I_{t_{g_x}}(1 - e_y) = 0.6205} \tag{5-3}$$

$$\mathbf{I_{dif_{g_y}} = \frac{I_{t_{g_x}}e_y}{2} = 0.05475} \tag{5-4}$$

Notice that $I_{dif_{g_y}}$ corresponds to the final relative intensity of the beams in the Y direction, which correspond to the wavevectors k_{y1} and k_{y2}, presented in Chapter 4. On the other hand, $I_{dif_{g_x}}$ suffers a second diffraction effect. The relative intensities of k_{x1} and k_{x2} are

$$\mathbf{I_{dif_{g_xg_y}} = I_{dif_{g_x}}(1 - e_y) = 0.11475} \tag{5-5}$$

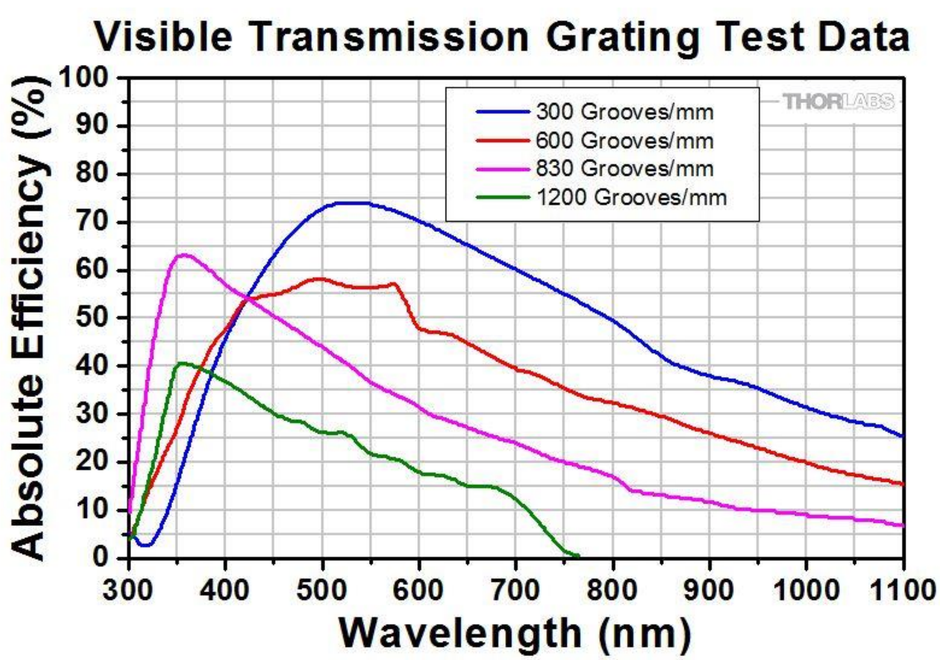

Figure 5-6. Absolute efficiency of gratings as a function of wavelength and line density. (Data from Thor Labs).

It can be shown that the order in which the gratings are arranged does not influence the final relative intensities of the beams. There are also secondary beams formed due to the diffraction of $I_{dif_{gx}}$ at g_y. Notice that $I_{dif_{gxgy}}$ is the transmitted part of $I_{dif_{gx}}$ through g_y. Although there are secondary beams, their intensities are very small – on the order of $\frac{e_x e_y}{4} \cong 0.01$. The total efficiency of this grating system is

$$\mathbf{e = e_x(1 - ey) + e_y(1 - e_x) = 0.339} \tag{5-6}$$

Around 34% - not considering any reflection effect at the boundaries of the gratings, which reduces more the efficiency - of the light generated by the laser is used for interference and measurements. The remaining 66% are either lost on secondary beams or as transmitted light. Despite the modest efficiency, the output of the laser is powerful enough so that there is sufficient light for the measurements.

For the crossed terms, i.e., when beam k_{x1} interferes with k_{y1} for example, the intensities of the beams do not match. The contrast function can be used to analyze the impact of that on the final interference pattern. The maximum and minimum intensities, based on Equation 2-7

$$\mathbf{I_{max} = I_{k_{x1}} + I_{k_{y1}} + 2\sqrt{I_{k_{x1}} I_{k_{y1}}} \cong 0.328} \tag{5-7}$$

$$\mathbf{I_{min} = I_{k_{x1}} + I_{k_{y1}} - 2\sqrt{I_{k_{x1}} I_{k_{y1}}} \cong 0.011} \tag{5-8}$$

$$\boldsymbol{\gamma_{max}} = \frac{\mathbf{(I_{max} - I_{min})}}{\mathbf{(I_{max} + I_{min})}} \cong \mathbf{0.935} \tag{5-9}$$

Equation 5-9, known as the contrast equation, indicates that the theoretical maximum contrast when the intensities are different as in this case, is lowered from 1 to 0.935, which should not cause a big impact on the modulation, and therefore the speckles should modulate without big problems.

5.3 Design description

5.3.1 Laser mount: lens system, temperature control apparatus

The laser is a very small component, and a proper mount was designed to integrate the laser with the thermocooler plate, and to integrate with the lens system.

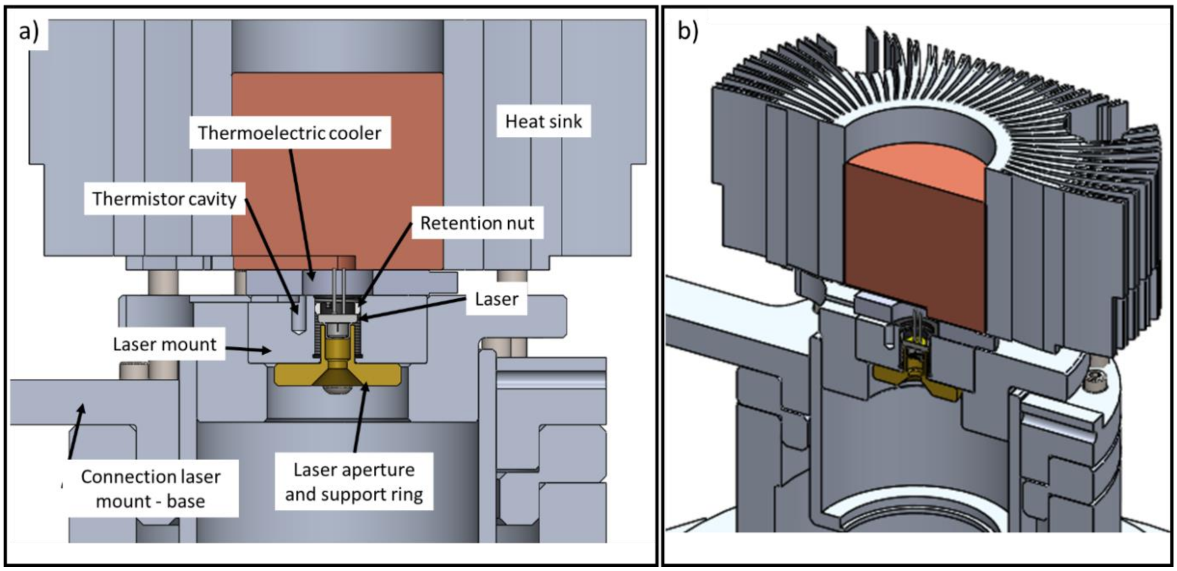

Figure 5-7.(a) Frontal view of a cut showing the disposition of components such as the laser, the thermocooler plate and heat sink. (b) Isometric view of the assembly.

The thermocooler plate, an electronic device based on the Peltier effect, is controlled by a PID controller capable of offering up to 1.5A of current. The current passes through the terminals, warming up on side of the plate and cooling down the other side, allowing heat transfer. The maximum power dissipation of the plate is 9W when operating at 6V and 1.5A. The PID controller allows the current to invert polarity, so the thermocooler can be used both to cool or to heat up the laser and maintain the desired temperature. The heat sink on top is used to dissipate the heat of the hot side of the thermocooler, when cooling the laser, or to transfer heat from the ambient to the laser, when warming up the assembly. All parts surrounding the laser were designed to be made of aluminum and increase the thermal contact with the laser.

The lenses are assembled as shown in Figure 5-8. There is possibility of moving both the divergent lens and the laser vertically to adjust final beam diameter and to assure good collimation.

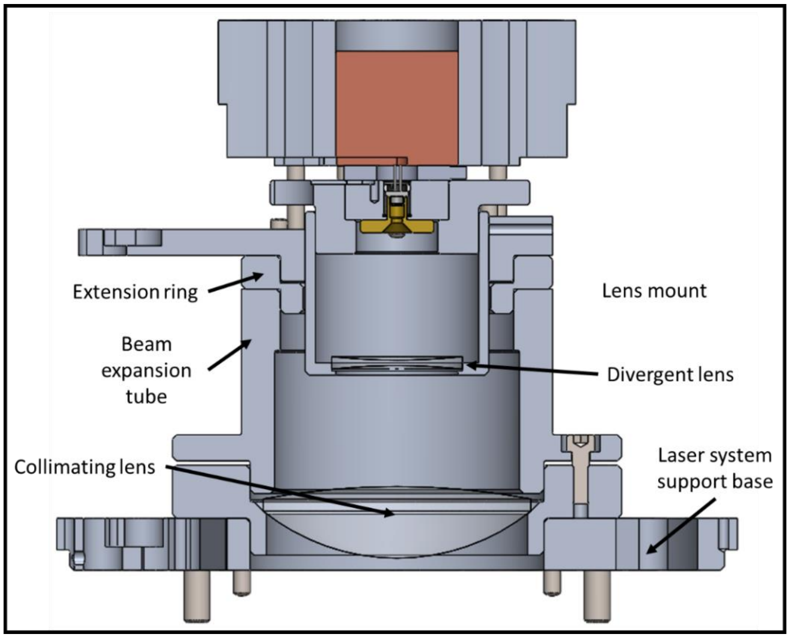

Figure 5-8. Cross section view showing the lenses and the supporting parts.

5.3.2 Diffraction grating stage

The diffraction grating mount was designed as a flexible structure. The use of two PZT made it possible to translate both gratings in the X and Y directions, to obtain the necessary phase shift. The grating stage was designed as one single piece with an inner compliant structure within an outer compliant mechanism as shown in Figure 5-9.

By stepping the PZT set for the X direction, for example, the whole structure translates carrying the gratings with it. The translation of g_y in the X direction does not introduce any phase shift to the beams k_{y1} and k_{y2}. The same is valid for translating g_x in the Y direction. When using the crossed beams, i.e., when interfering k_{yi} with k_{xi}, it was chosen that the phase shift would only happen in g_y since the motion required there is smaller - p_y is smaller than p_x. The amount of motion is a fraction of p_x or p_y, the line spacings of g_x and g_y. The calibration of the PZTs is done by a correlation method [38].

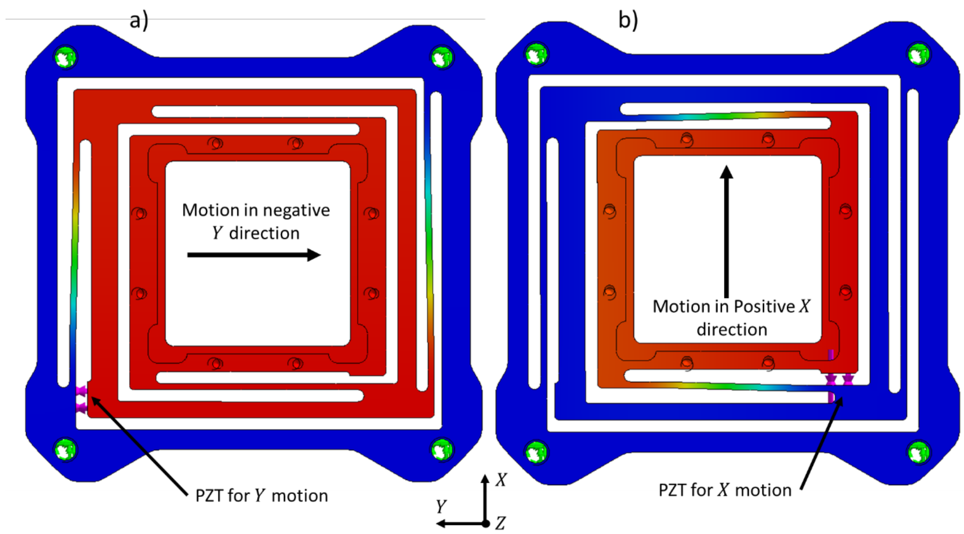

Figure 5-9.(a) Simulation of the translation of flexure in the negative Y direction with indication of the PZT position. (b) Translation of the inner structure in the positive X direction with indication of the PZT position. The scale of motion is exaggerated for easier visualization.

Figure 5-10 in the left shows an isometric view of the grating assembly. In the right of Figure 5-10, the plate holding the gratings together is visible.

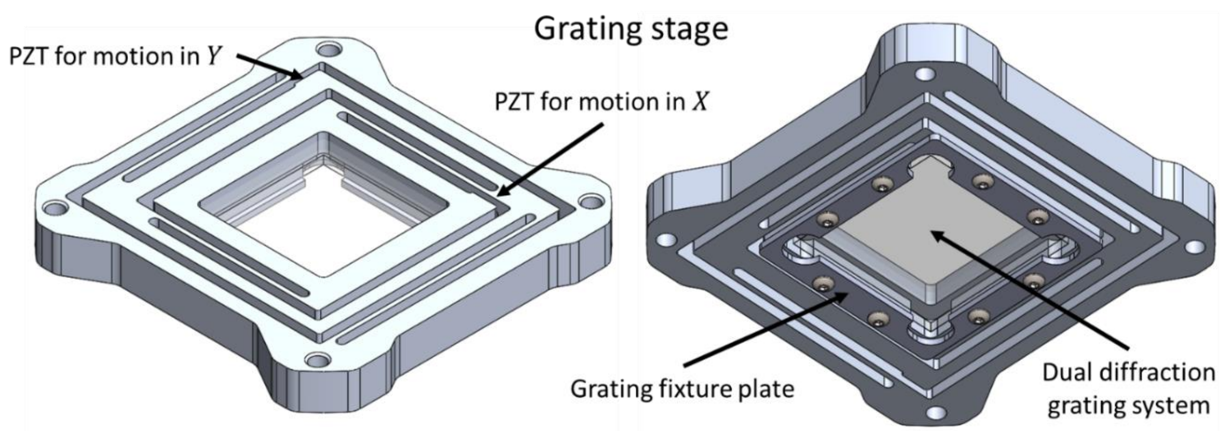

a) b)

Figure 5-10.(a) Top isometric view of grating stage with indication of the PZTs position. (b) Bottom Isometric view of the grating stage with diffraction grating position indicated.

The grating stage is assembled on the laser system supporting base and has 4 sets of screws for tuning up the grating inclination as depicted on Figure 5-11. It can be shown that the grating angle influences the diffraction angles and this feature can be used to tune up the beams to get the interferometer to operate within coherence limits [33].

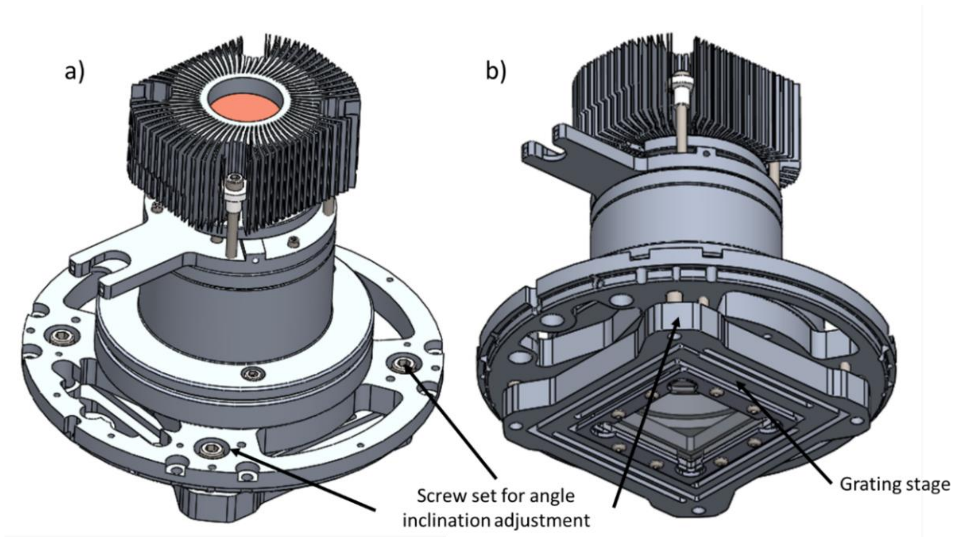

Figure 5-11.(a) Top isometric view of the laser system with the grating stage attached at the bottom. Some of the screw sets for alignment are indicated. (b) Bottom view of the laser system with the grating stage attached as indicated.

5.3.3 Mirror configuration

To direct the diffracted beams at the surface, sets of mirrors in a parallel geometry can be used as it is depicted in Figure 5-12.

The grating g_x has larger line spacing and therefore the diffracted beams present sharper angles. The configuration with two simple mirrors parallel to each other is sufficiently compact. On the other hand, grating g_y diffracts the beams with larger angle and the configuration with parallel beams becomes very big as can be seen on Figure 5-12 in the right.

The large size is also driven by the measurement area to which the interferometer was designed for. An alternate configuration was then implemented, with the addition of one mirror in each side of the in-plane arrange in Y. The camera originally intended to be used - PROSILICA GC1290 - was also replaced by a smaller USB camera, utilizing the same CCD model – the Point Grey Chameleon3. Both the new mirror arrangement and the new camera allowed a drastic size reduction. The proposed configuration is show in Figure 5-13.

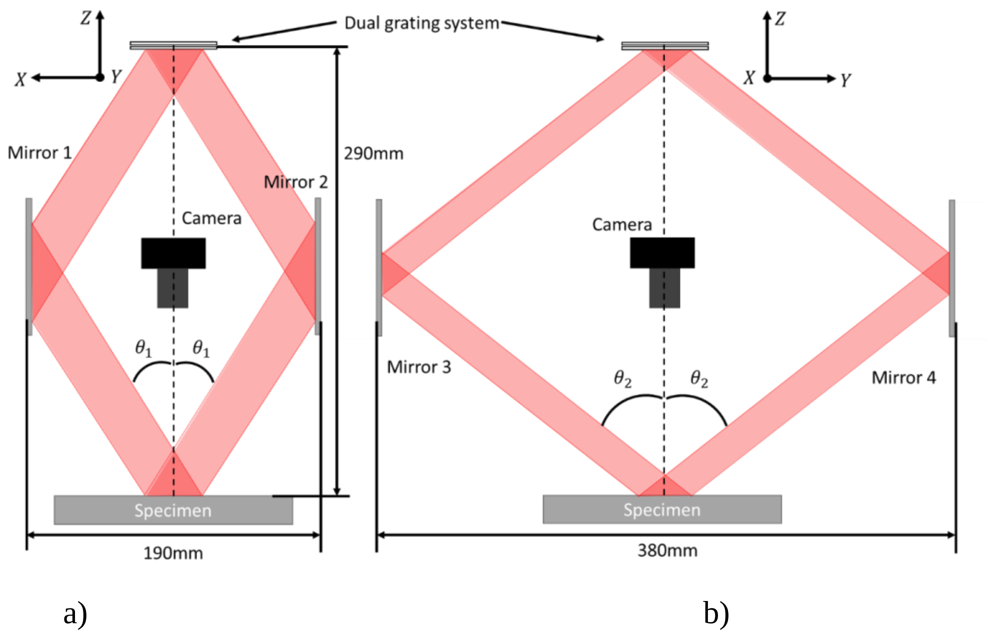

Figure 5-12.(a) Schematics of mirror arrangement for in-plane axis with sensitivity in the X direction. (b) Schematics of parallel geometry of mirrors for the in-plane arrangement in the Y direction.

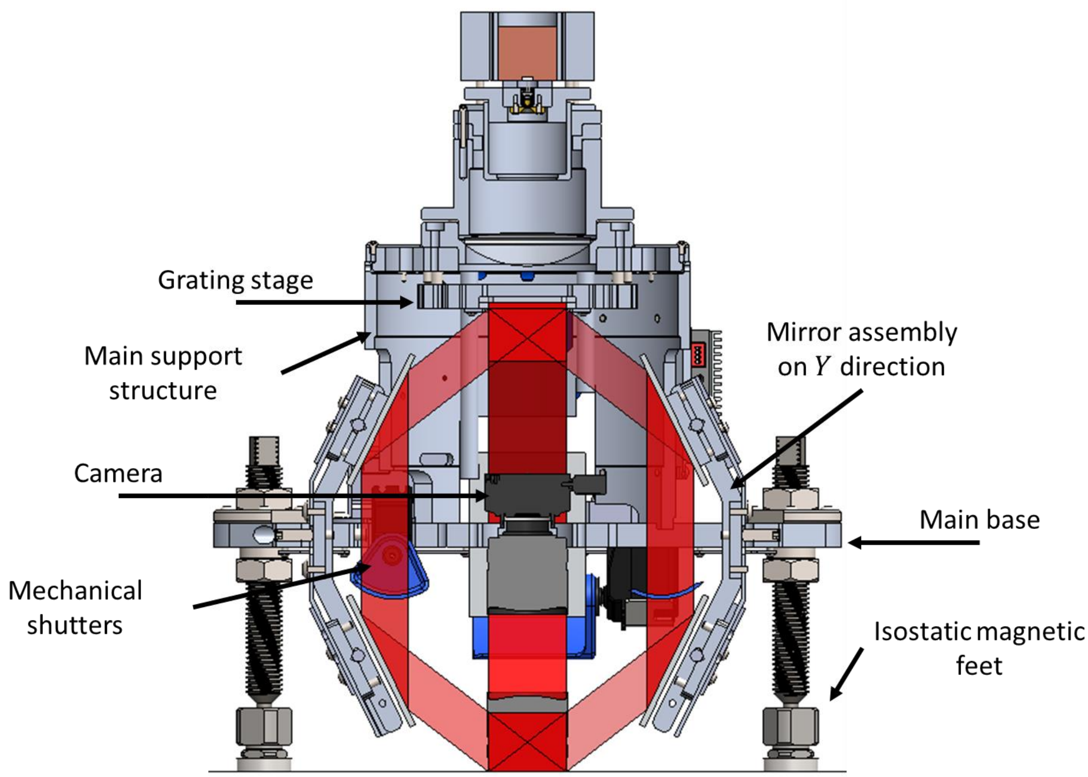

Figure 5-13. View in cut showing the beam arrangement on the Y direction. The magnetic feet, mechanical shutters, camera and grating stage are indicated.

The mirror system shown above, with the additional mirror, is capable of folding the light beams in a more compact region. The mirror configuration for the X axis is as shown schematically on Figure 5-12 in the left. The main base of the system is also shown as a cross section on Figure 5-13.

The mechanical shutters are just polymeric components that are rotated through servo-actuators in and out of the way to block or let the beam pass. The shutters can be controlled independently so all the six different beam combinations are possible, with only two shutters opened at a time.

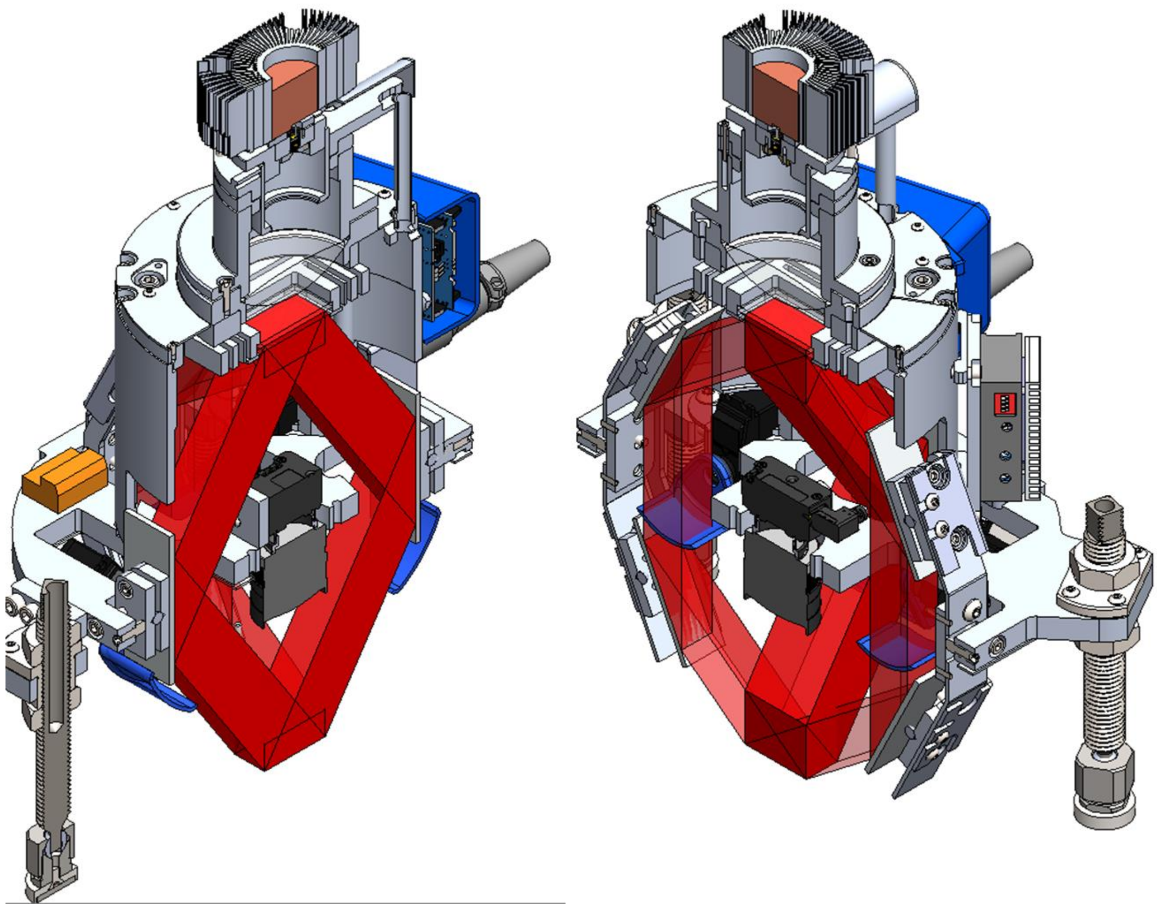

a) b)

Figure 5-14.(a) Cut view in perspective of X axis configuration. The geometry is simpler with only two parallel mirrors. (b) Cut view in perspective of Y configuration. There is one additional mirror to each side to fold the beam and reduce size.

The magnetic feet are capable of exerting 120N of force in the normal direction. The magnets are neodymium rare earth magnets. The threaded rod allows the base height and therefore the system's height to be adjusted so a variety of samples can fit in the measurement area.

Figure 5-14 shows two views in cut of both X and Y axes. On Figure 5-15(a), an isometric view of the whole system with the Arduino and the main connectors indicated. The electrical connections involve power for the laser driver, for the thermocooler, for the servo-actuators and for the PZTs. The camera and Arduino run with independent USB cables. Figure 5-15(b) shows the temperature controller and one of the four servo-actuators – which is responsible for moving one of the shutters - is indicated.

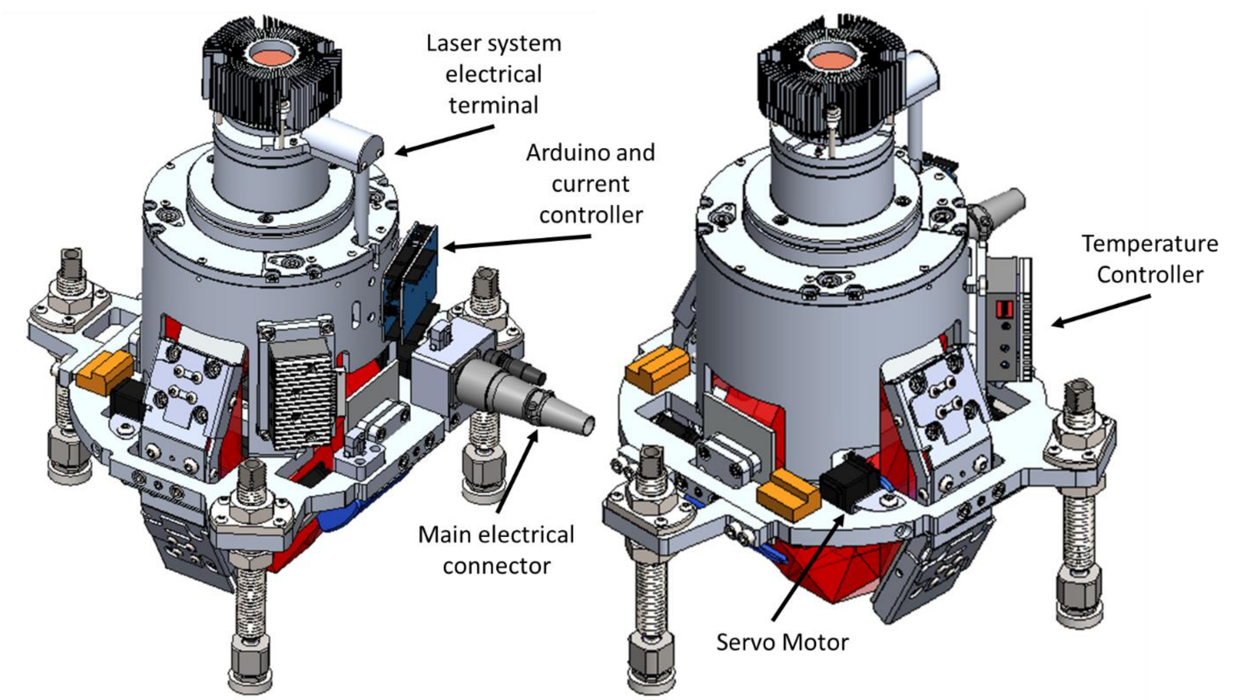

a) b)

Figure 5-15.(a) Isometric view of the external part of the system, with current controller position and main connectors indicated. (b) Isometric view showing the temperature controller and one of the servo-actuators responsible for moving the shutters.

5.4 Construction and fabrication of main components

The fabrication of all the components, except the commercially available components, was mainly done by the author in the student machine shop in the Mechanical Engineering Department at UBC. The design was developed so that many components could be fabricated using the waterjet cutting machine, thereby saving time and allowing more complex and functional parts to be made.

The following pictures show important components such as the main base, the support tube and the laser system base support while on fabrication. Processes like turning and milling were used in almost all of the components. In the components cut by waterjet, the main post cut work was related to positioning and fixing features like reference and bottoming holes.

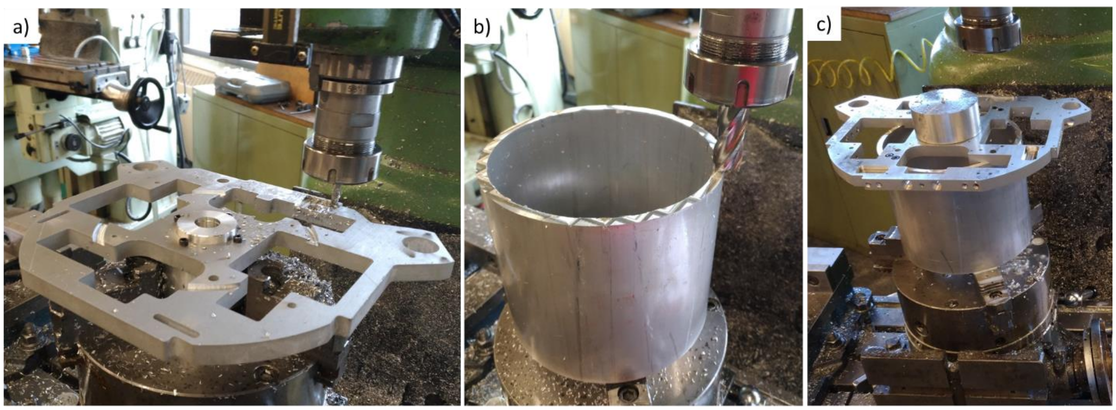

Figure 5-16.(a) Main base while in the milling machine for drilling of reference holes, reference slots and centering features. (b) Main support tube, responsible for connecting the laser system to the main base. (c) Machining of reference and centering features was executed with the main base and the support tube connected.

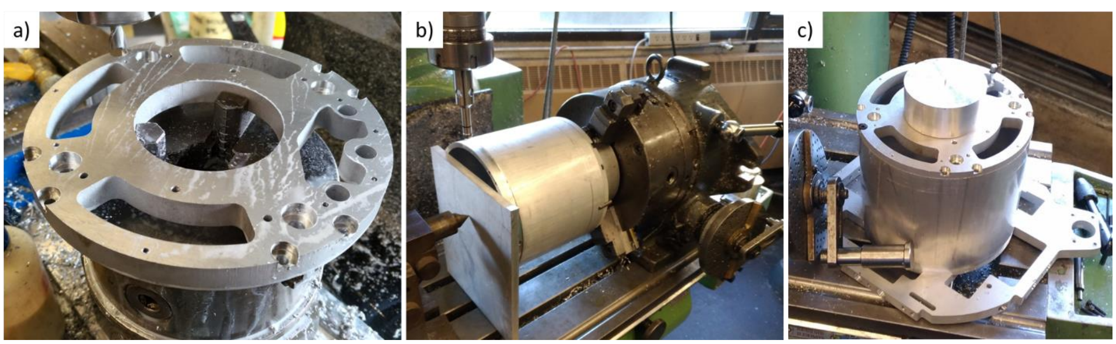

Figure 5-17.(a) Milling step of the laser system base. The use of a rotary device allowed the machining of all holes and features referenced to the center of the piece. (b) Preparations for milling of side slots on the main support tube. (c) Connection between the three main components of the assembly: Main base (bottom), main support tube (middle) and laser system base (top).

As shown on Figure 5-16(c), some components were machined while in the assembly to guarantee good alignment and referencing for the assembly step.

Figure 5-18 shows most of the components alongside the main assembly, prior to the final assembly process.

The grating assembly is shown on the left in Figure 5-19. The gratings are assembled in the grating stage and the PZTs are in placed with the wiring on profess. The assembly of the grating stage on the laser system base is shown on the right.

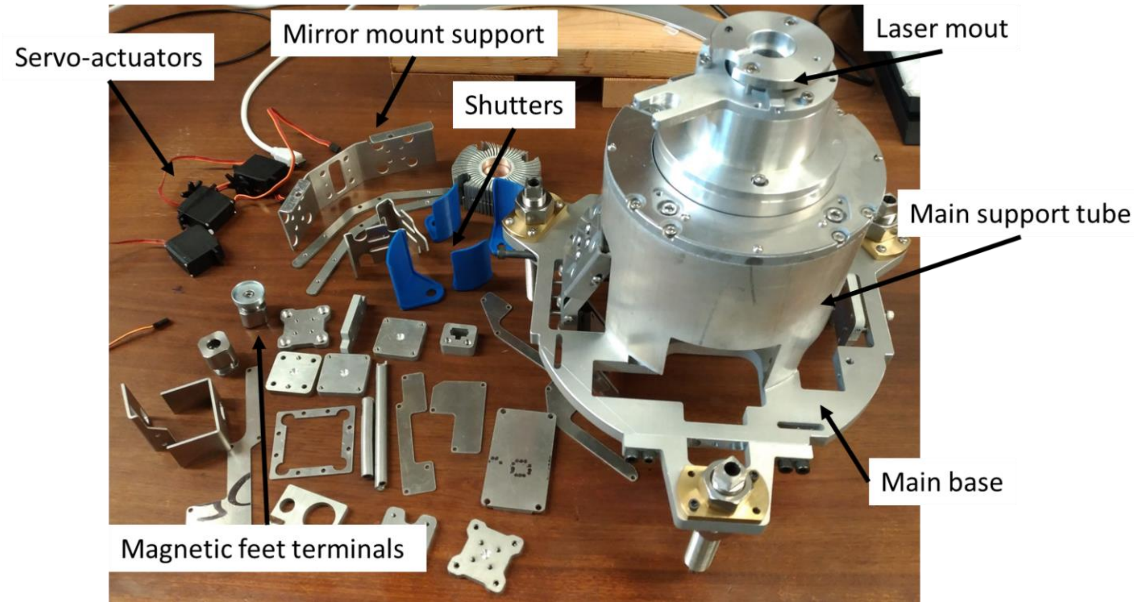

Figure 5-18. Most of components alongside the main assembly. A few key components are indicated with black arrows.

After the full assembly, work on adjusting the position of the mirrors was performed using the spherical joints designed for the mirror supports. The positioning of the lenses was performed systematically to prevent collimation problems. The wiring of all the components as done so as to avoid having loose wires in the assembly. Key elements such as the laser and PZTs received shielded wires to minimize electromagnetic interference and noise irradiation.

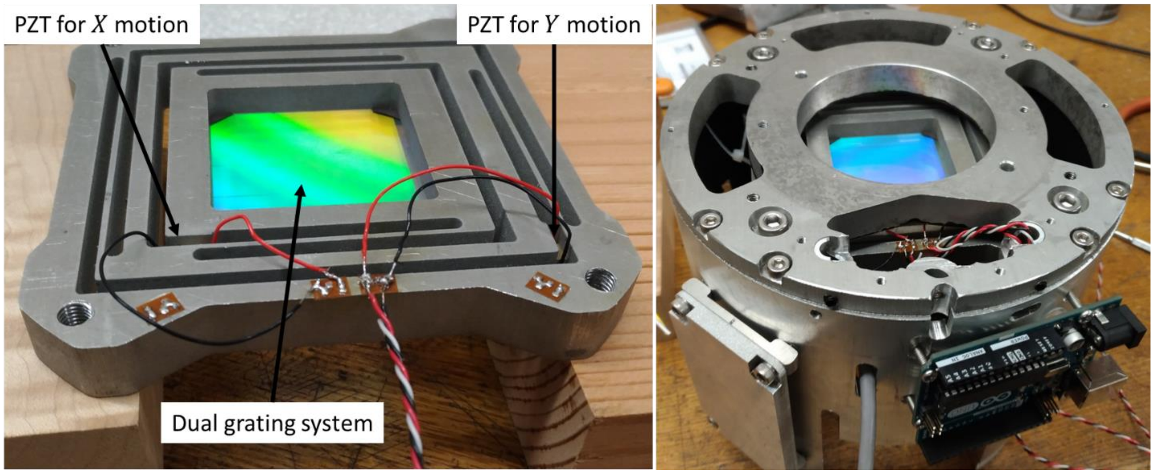

Figure 5-19.Left: Grating assembly with the PZTs position indicated and the dual diffraction grating assembly visible in the center. Right: Grating stage assembled into the laser system base.

A box was built to fit all the main electronics, such as DAQ boards, power supply, and PZT amplifiers, which were built especially for this device. Figure 5-20 shows the Arduino board with the current controller and the electrical box with electronics components inside.

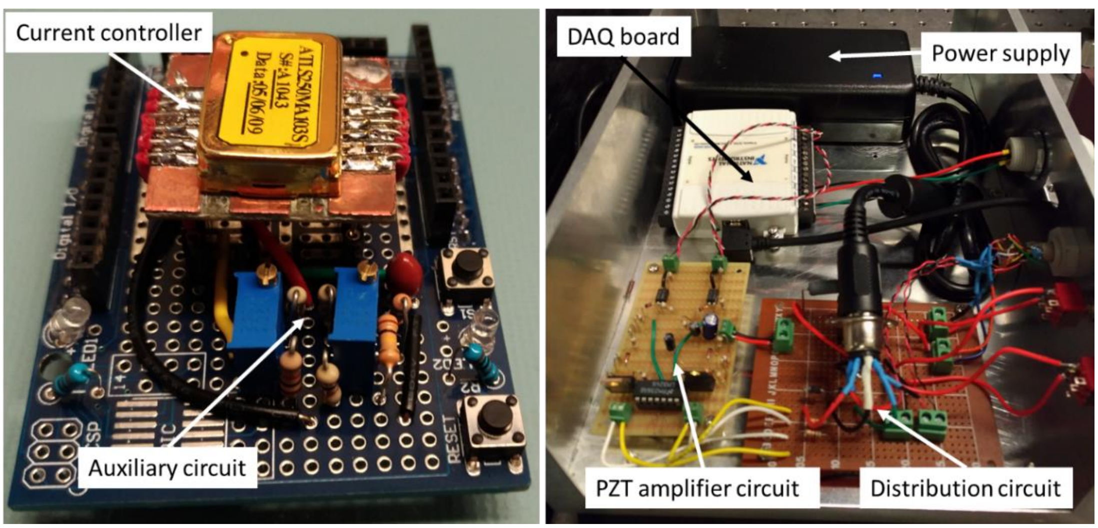

Figure 5-20. Left: Arduino based circuit for current driver. Right: Electronic box with amplifier, power supply, DAQ board and distribution board.

Finally, the actual assemble device is shown on Figure 5-21.

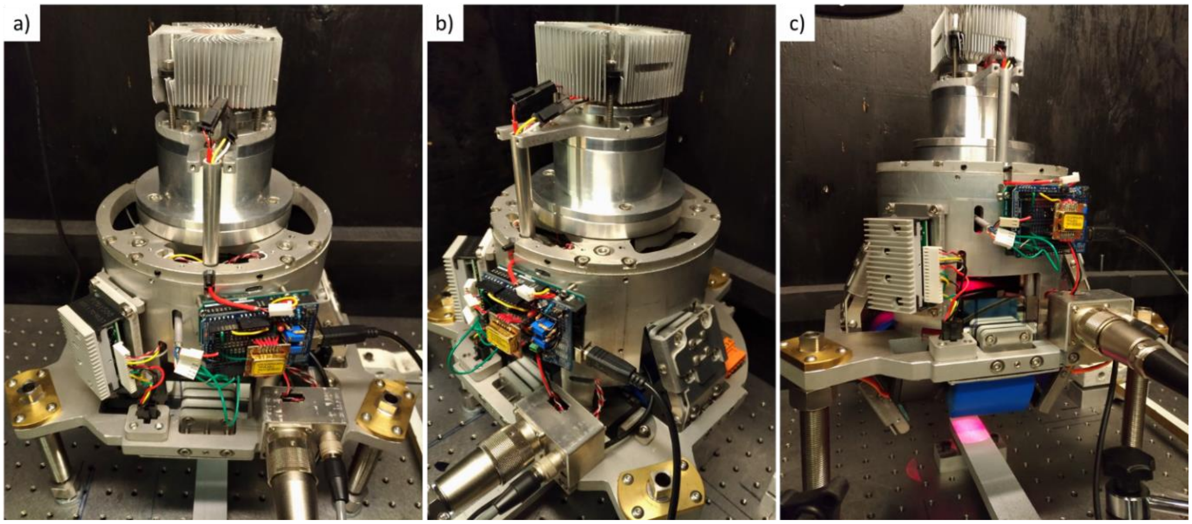

Figure 5-21.(a) Frontal view of full assembly. (b) Lateral view of assembly showing mirror mounts and current driver. (c) View of a sample under the system for a displacement measurement.

The next chapter will present results obtained with controlled samples and the measurement of 3D displacement in a cantilever beam under bending.

Chapter 6: System testing and 3D displacement measurements

This chapter describes the calibration procedure for the prototype interferometer using a controlled sample. During initial calibration, a geometrical problem was discovered in the Y axis. This issue is discussed in details and its implications on the measurement quality is further explored.

Temperature and current control of the laser is presented as a method to overcome the problem. A comparison between X and Y axes shows that it is possible, with an equivalent geometrical configuration, to overcome the problem independently of temperature control.

A sample under 3D deformation, bending in two axes, is used to demonstrate the capabilities of the system for measuring 3D displacements. A method for identifying defective pixels is used to improve overall measurement quality. Data averaging by the least squares method is used to obtain the three displacement components from the six different measurements available. The measurement results are validated by comparison with finite element analysis.

6.1 Geometrical problem in the Y axis

In Chapter 5:, it was stated that the arrangement in the Y axis was modified with the addition of one extra mirror in each side, so that the beam could be folded into a more compact geometry.

After construction and assembly, it was discovered that the extra mirror had the unanticipated effect of introducing a significant path length difference across the measurement area. Thus, the extra mirror caused the time fronts from one side to arrive at the surface substantially inclined relative to the time fronts of the other side of the arrangement.

Figure 6-1 shows the comparison between the wavefronts and time fronts propagation for a parallel mirror geometry and for the proposed configuration. Figure 6-1(a) shows that the time fronts exit the diffraction grating with horizontal orientation and pass unaltered by the mirror, reaching the surface parallel with time fronts from the other side. The geometry of this configuration is a parallelogram. Figure 6-1(b) shows that the wavefronts exit the grating with angle θ_2 and arrive at the surface with angle θ_2. The time fronts, however, exit parallel to the grating but unlike in Figure 6-1(a), they arrive with a different angle, thereby introducing a path length difference δ_{pl} between a1 and a2, for example.

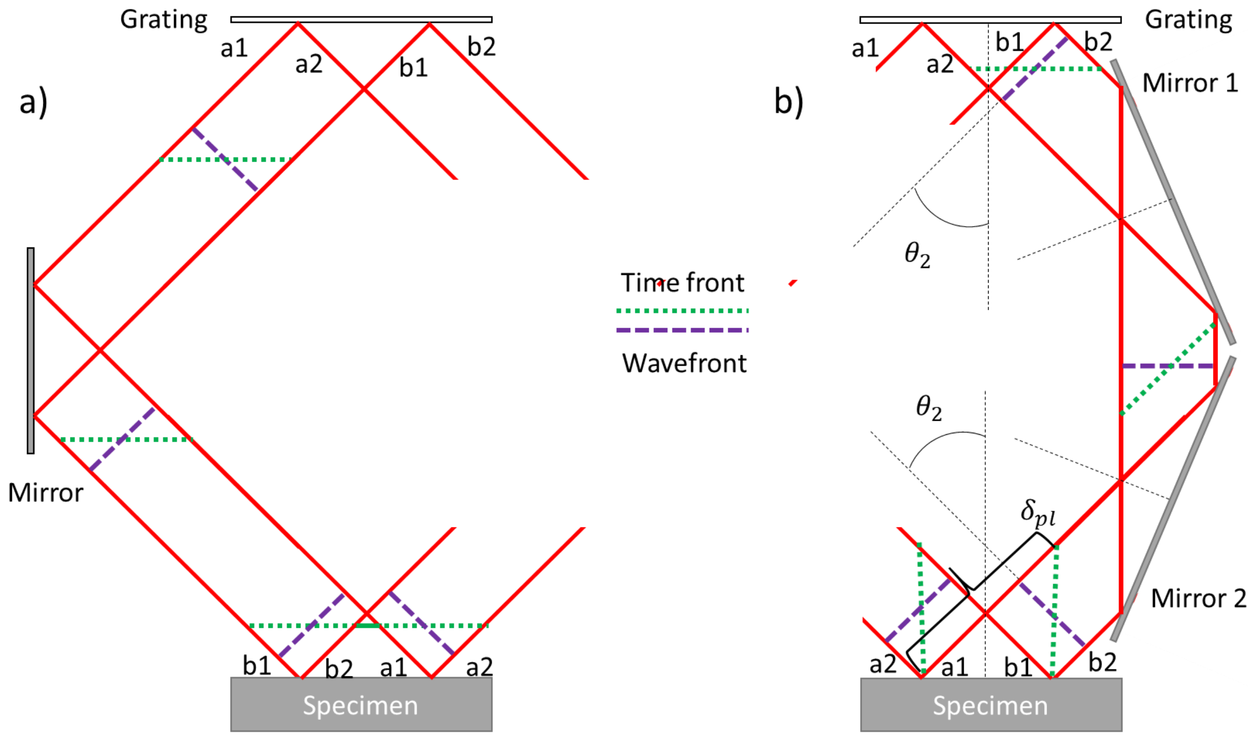

Figure 6-1. (a) Parallelogram geometry used on the *X* direction arrangement. The time fronts exit the grating and arrive at the surface with the same angle. (b) Geometry with extra mirror showing that the time fronts exit and arrive the surface with different angles, and are not parallel with time fronts from the opposite beam.

The path length difference is dependent of the position within the illumination area. At the center, the path length difference δ_{pl} is zero. For a measurement area of width 30mm, the path length difference ranges from -42mm in one side to 42mm in the other side. The coherence interval H for this laser is 12.6mm, thus there should be six to seven coherence bands visible within the measurement area.

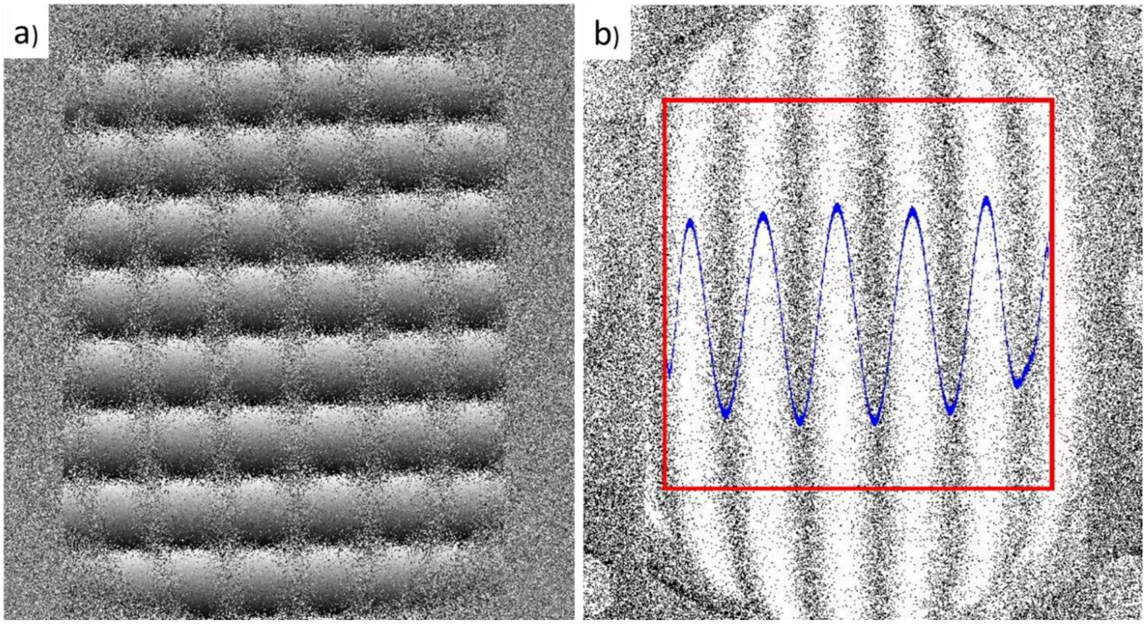

Figure 6-2. (a) Phase map of measurement in the Y axis. The coherence band effect on the noise is shown. (b) Visibility map of measurement in the Yaxis with the geometric problem. The six coherence bands are in agreement with the prediction for this measurement area width. The blue lines are column average visibility for points within the red rectangle. A curve close to the bottom means V=0 and close to the top V=0.5

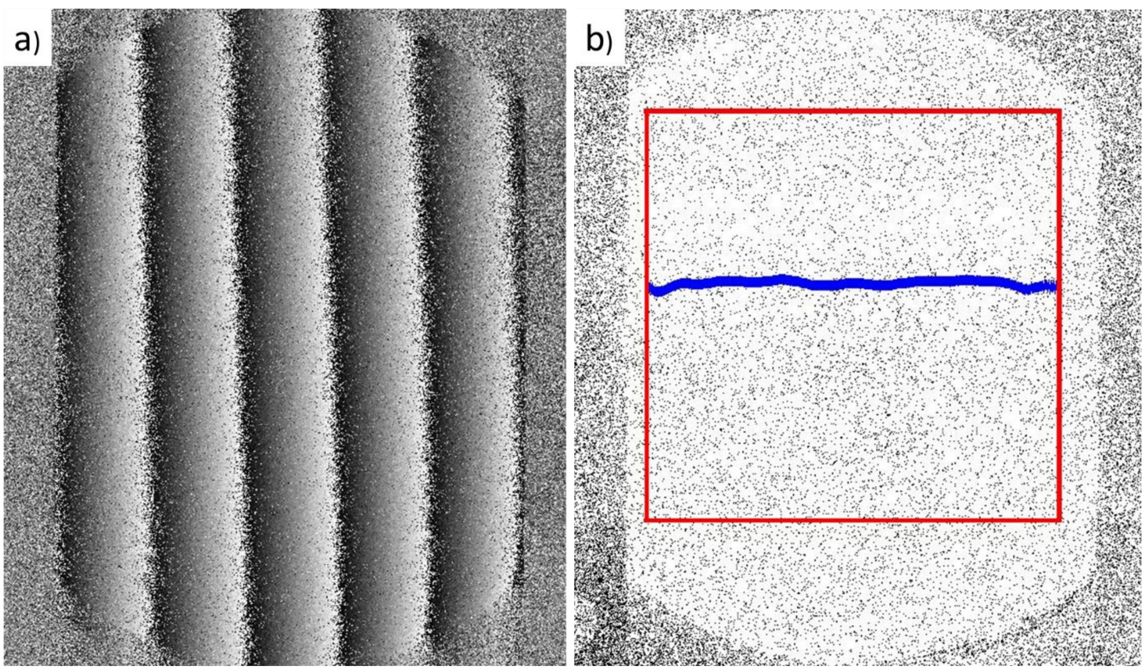

Figure 6-3. (a) Phase map obtained in the X direction. The noise level is reduced since the geometry corrects for the light source coherence limitations. (b) Visibility map in the X direction. Th distribution is constant throughout the region of interest.

While the problem compromises the measurement quality in one of the axis of the system, it however serves as a good example of how the geometry is important in an ESPI interferometer using a laser diode as light source. The parallelogram geometry of the X axis demonstrates the effectiveness of geometrical control over the coherence limitations of the laser source.

Figure 6-2(a) shows a phase map acquired in the Y axis. Figure 6-2(b) shows the visibility map where the expected six coherence bands can be seen. Figure 6-3(a) shows a result for the same measurement, in the X axis, where there is the desired parallel geometry. The measurement direction is perpendicular to Y so the fringes are vertical. The adverse effect of the coherence bands in the measurement in Figure 6-2(a) is clear while in Figure 6-3(a) the quality is consistently good. Figure 6-3(b) shows the visibility map of the X axis measurement.

6.2 Temperature and current control

A practical way of overcoming coherence and geometric problems is by using active temperature and current control. In Chapter 5:, it was shown in Figure 5-3 that the laser diode used in this system operates with high coherence at a current of approximately 120mA. The laser driver was then set to provide a drive current of 120mA.

The temperature was also controlled using an active controller. A thermistor was placed next to the laser diode to monitor the temperature and provide feedback the thermo-controller.

Figure 6-4(a) shows a phase map of a Y axis measurement with the thermocooler switched off. The temperature of the laser was measured to be 20.2°C. The blue lines in the visibility map shown in Figure 6-4(b) represent the column average of the visibility within the rectangular region of interest. The scale for visibility is zero at the bottom of the rectangle, rising to 0.5 at the top. Figure 6-4 (c) shows the phase map for a temperature of 23.8°C. This temperature is midway between the ambient and the optimal temperature which was determined experimentally to be 26.8°C. The measurement has the more evenly spread noise compared with Figure 6-4(a), but is not ideal. Figure 6-4 (d) shows the visibility map of the laser at 23.8°C. The coherence length and visibility are reduced. Figure 6-4(e) shows the phase map when the temperature is 26.2°C. This is approaching the optimal temperature. Notice that the coherence bands have increased in width (Figure 6-4(f)), meaning that the coherence length is increased. Figure 6-4 (g) shows the phase map at the optimal temperature of 26.8°C. The coherence bands are no longer evident. Figure

6-4(h) shows the corresponding visibility map at 26.8°C. The coherence length has increased to the point where the coherence in the minimum regions rises to be almost equal to the coherence in the maximum regions.

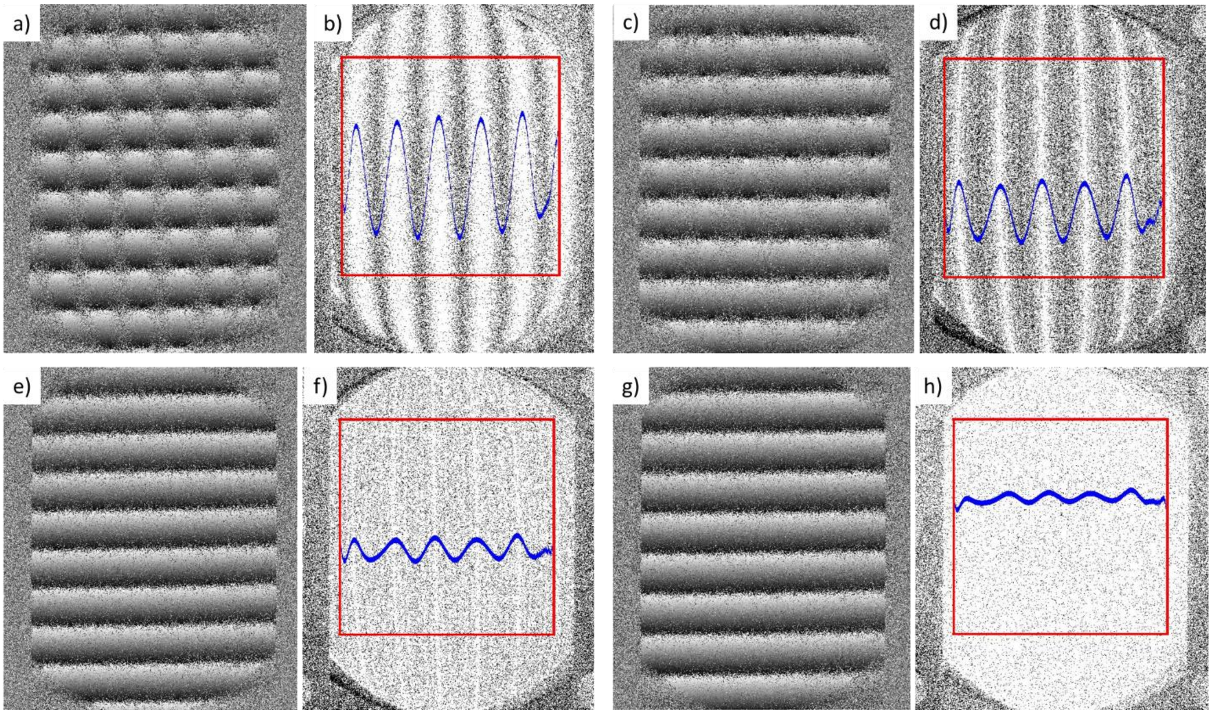

Figure 6-4. Effect of temperature control to achieve more uniform visibility.

(a) Phase map measured at 20.2°C. (b) Visibility map measured at 20.2°C. Coherence fringes are very clear. (c) Phase map taken at 23.8°C. the noise levels are spread out as the coherence length changed. (d) Visibility map at 23.8°C with the reduced coherence length. (e) Phase map at 26.2°C, approaching the optima temperature. The noise levels are reduced. (f) Visibility map at 26.2°C. The visibility starts to become homogeneous and the coherence bands are less evident. (g) Phase map at optimal temperature of 26.8°C. The noise level is low and uniform across the measurement region. (h) Visibility map showing a practically constant visibility of the order of V=0.3. The gap in visibility in between the coherence bands is very low.

The temperature control allied with current control was shown to improve the coherence of the laser, and therefore this approach can be considered an alternative method to allow the use of a simpler laser diode as a light source for ESPI measurements.

6.3 Controlled sample for system calibration

Calibration of the system was performed using a simple mechanism to introduce known displacements. Both magnitude and direction are known so the sensitivity directions and magnitudes can also be determined.

Small misalignments on the mirrors can introduce residual sensitivity in directions other than the main direction, causing deviations in the sensitivity vectors introduced on **Error! Reference source not found.**, sections 4.4.1) - 4.4.3). The next sections describe the apparatus used for the calibration and the methods used for estimating the actual sensitivities of each axis.

6.3.1 Experimental apparatus

A robust mechanism was designed to produce known displacements both in-plane and out-of-plane. The device comprises a rigid bar that rotates on a spherical joint at one end and slides on two smaller spheres at the opposite end. The measurement is performed on the top surface of the bar, with the measurement region centered on the point of rotation.

The in-plane displacement is applied at $L_1 = 273.6 \pm 0.1$ mm from the rotating pivot and is measured with a dial gage. Similarly, the displacement in the out-of-plane direction is applied at $L_2 = 300.2 \pm 0.1$ mm of rotation point and measured with a second dial gage.

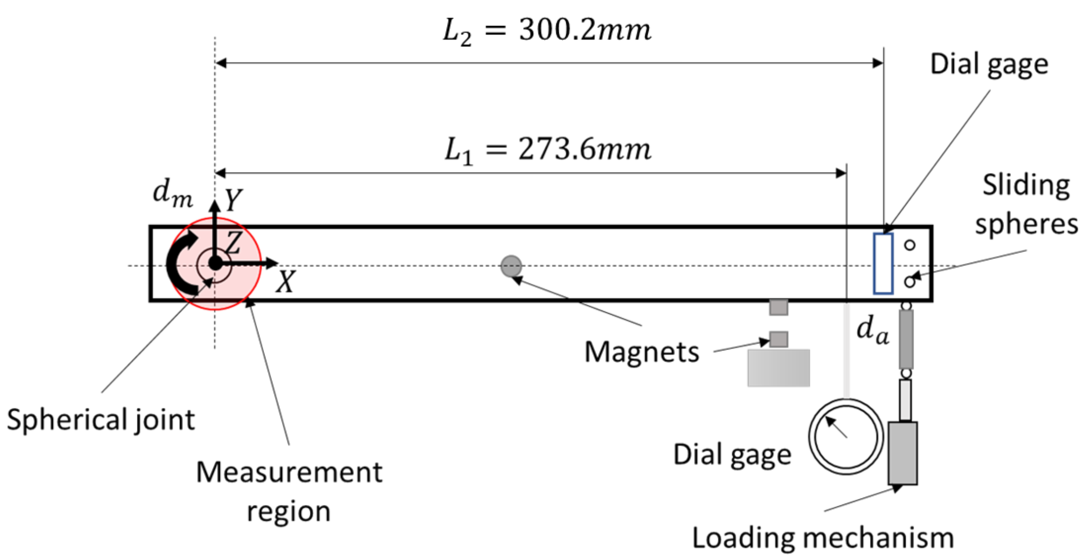

Figure 6-5. Schematics of the mechanical apparatus used for calibration. It consists of a rigid bar that rotates on a spherical joint both in-plane and out-of-plane. The dial gages, as indicated, are used to quantify the displacements applied by the loading mechanisms. The measurement area is indicated in red.

The bar is held down on the table by two magnets, one attached to the beam and one attached to the table, as seen in a top view on Figure 6-5. Similarly, a second pair of magnets is used to provide a restoring force in the in-plane direction. The bar is made of aluminum with a thickness of 12.7mm so that the bending under self weight is negligible. The total length of the beam is 340mm and the width is 30mm.

The uncertainties involved in the applied displacement are dependent on the measurement of the distances and on the accuracy of the dial gages. The distances of the points of applied displacements to the rotating joint were measured using digital calipers with resolution of 0.01mm. The width of the beam was also measured with using a digital caliper. The resolution of the dial gages is 1 thousandth of an inch (0.0254mm). The dial gages are analogic devices so the uncertainty involved in the measurement is taken to be one half of the resolution.

Figure 6-5 shows schematics of the quantities involved. The relation between the applied displacement and the displacement at the region of interest is

$$\mathbf{d_m} = \frac{\mathbf{d_a L_m}}{\mathbf{L_i}} \tag{6-1}$$

where d_a is the displacement applied and measured at the dial gage, L_m is the length of the measurement region of interest, centered at the rotation pivot, and L_i is the distance from the point of application of d_a to the center of the region of interest. L_i can be either for the in-plane or out-of-plane load application. The uncertainties of d_a and L are $\Delta d_a = \pm 0.0127$mm and $\Delta L_i = \pm 0.1$mm. In the case of L_m, it is more practical to define the uncertainty based on the scale of the camera. The region of interest for analysis is a rectangle of X by Y pixels. Knowing that the width of the region of interest to be $h = 30.4 \pm 0.1$mm, and observing that there are 682 ± 1 pixel within this range, we have that the uncertainty in the pixel size and the pixel size are

$$\boldsymbol{\Delta P_s} = \sqrt{\left(\frac{\partial \boldsymbol{P_s}}{\partial \boldsymbol{N_p}} \boldsymbol{\Delta N_p}\right)^{\mathbf{2}} + \left(\frac{\partial \boldsymbol{P_s}}{\partial \boldsymbol{W}} \boldsymbol{\Delta h}\right)^{\mathbf{2}}} = \mathbf{0.00015}\boldsymbol{mm} \tag{6-2}$$

$$\mathbf{P_s} = \frac{\mathbf{W}}{\mathbf{N_p}} = \mathbf{0.04454 \pm 0.00015mm} \tag{6-3}$$

Therefore, knowing that the length of L_m in pixels is $n_p = 700$,

$$\boldsymbol{\Delta L_m = \sqrt{\left(\frac{\partial L_m}{\partial P_s}\Delta P_s\right)^2 + \left(\frac{\partial L_m}{\partial n_p}\Delta n_p\right)^2} = 0.12\ mm} \tag{6-4}$$

$$\boldsymbol{L_m = P_s.n_p = 31.2 \pm 0.1mm} \tag{6-5}$$

Finally, the uncertainty of d_m is

$$\boldsymbol{\Delta d_m = \sqrt{\left(\frac{\partial d_m}{\partial d_a}\Delta d_a\right)^2 + \left(\frac{\partial d_m}{\partial L}\Delta L\right)^2 + \left(\frac{\partial d_m}{\partial L_m}\Delta L_m\right)^2} = 0.0017mm} \tag{6-6}$$

The in-plane displacement is seen as a rotation in the XY plane around the Z axis. The out-of-plane displacement applied is seen as a rotation in the XZ plane around the Y axis. The equations above can be used both for in-plane and out-of-plane displacements.

It can be shown that in the case of the out-of-plane rotation, there is a constant displacement in the X direction due to the rotation of the bar with respect of the center of the spherical joint. This displacement is coupled with the out-of-plane displacement. However, it should not cause any relative phase change from one point to another within the measurement region since it is constant across the measurement region. Thus, the phase measured with the 4 composed axes, in-plane and out-of-plane sensitivity, is expected to be only due to out-of-plane motion.

In practice, several measurements are taken, so the uncertainty in the average is reduced. For N_m measurements

$$\boldsymbol{\overline{d_m} = \frac{\overline{d_a} L_m}{L_i} \pm \overline{\Delta d_m}} \tag{6-7}$$

$$\boldsymbol{\overline{\Delta d_m} = \frac{\Delta d_m}{\sqrt{N_m}}} \tag{6-8}$$

where $\overline{d_m}$ is the average of all the measurements and $\overline{\Delta d_m}$ is the uncertainty on the average.

6.3.2 Calibration procedure

A calibration procedure was performed using the least squares method to compute the components of the six sensitivity vectors. Ideally, the relation between displacements and phases is as

$$\boldsymbol{[K_m]\{d_i\} = \{\Delta\Theta_m\}} \tag{6-9}$$

where $[K_m]$ is a matrix composed of all the sensitivity vectors, $\{d_i\}$ is the displacement vector and $\{\Delta\Theta_m\}$ is a vector with six phases. Equation 6-9 is valid for all the pixels within the measuring area, and is an operation done pixel by pixel.

Using Equations 4-5 through 4-9 and expanding Equation 6-9, we have

$$\begin{bmatrix} \mathbf{K_x} & \mathbf{0} & \mathbf{0} \\ \mathbf{0} & \mathbf{K_y} & \mathbf{0} \\ \mathbf{K_{3_x}} & \mathbf{K_{3_y}} & \mathbf{K_{3_z}} \\ \mathbf{K_{4_x}} & \mathbf{K_{4_y}} & \mathbf{K_{4_z}} \\ \mathbf{K_{5_x}} & \mathbf{K_{5_y}} & \mathbf{K_{5_z}} \\ \mathbf{K_{6_x}} & \mathbf{K_{6_y}} & \mathbf{K_{6_z}} \end{bmatrix} \begin{Bmatrix} \mathbf{d_x} \\ \mathbf{d_y} \\ \mathbf{d_z} \end{Bmatrix} = \begin{Bmatrix} \mathbf{\Delta\Theta_x} \\ \mathbf{\Delta\Theta_y} \\ \mathbf{\Delta\Theta_3} \\ \mathbf{\Delta\Theta_4} \\ \mathbf{\Delta\Theta_5} \\ \mathbf{\Delta\Theta_6} \end{Bmatrix} \quad (6\text{-}10)$$

In the ideal case, the beams are perfectly aligned and the elements contained in $[K]$ are and given by Equations 4-5 - 4-9. In practice, small misalignments that start at the laser output, propagate through the lenses, diffraction gratings and mirrors, cause the beams to have incidence angles that need to be measured or estimated. An alternative method for calibrating the sensitivity vectors is to use a sample with known displacements and then, by the least squares method, determine the components of the sensitivity vectors using the data available.

To implement the least squares method, Equation 6-9 is modified to a pixel wise form. This creates an equation for every pixel as a function of the known displacements and the known phases, to determine the value of the sensitivity vector components.

$$\begin{bmatrix} \mathbf{d_{y_1}} & \mathbf{d_{x_1}} & \mathbf{1} \\ \vdots & \vdots & \vdots \\ \vdots & \vdots & \vdots \\ \mathbf{d_{y_N}} & \mathbf{d_{x_N}} & \mathbf{1} \end{bmatrix} \begin{Bmatrix} \mathbf{K_{r_y}} \\ \mathbf{K_{r_x}} \\ \boldsymbol{\vartheta} \end{Bmatrix} = \begin{Bmatrix} \mathbf{\Delta\Theta_1} \\ \vdots \\ \vdots \\ \mathbf{\Delta\Theta_N} \end{Bmatrix} \quad (6\text{-}11)$$

where, for example, d_{y_1} is the displacement applied in the Y direction and seen in the pixel number one of the image. N is the total number of pixels in the image of dimensions m (rows) $\times$ n (columns). The value 1 in the third column of the displacement matrix is used to define the offset, if any, of phase ϑ in the point of zero displacement, which happens at the center of the spherical joint as seen in Figure 6-5. K_{r_x} and K_{r_y} are the real in-plane sensitivity components, which are to be determined by the least squares method, and $\Delta\Theta_1$ to $\Delta\Theta_N$ are the phases of the pixels.

The mechanical device shown in Figure 6-5 was used to apply known displacements, or rotations, to the sample. The rotation is dependent on the displacement d_a, applied at the loading mechanism, and on the distance spherical joint to the point of load application, L_i. The applied angle is

$$\boldsymbol{\alpha_{1-5} = \mathrm{atan}\left(\frac{d_{a_{1-5}}}{L_1}\right)} \tag{6-12}$$

For small angles, the relation can be simplified to

$$\boldsymbol{\alpha_{1-5} \cong \frac{d_{a_{1-5}}}{L_i}} \tag{6-13}$$

where L_i refers to the distance used for in-plane or out-of-plane displacement application. A total of 5 discrete displacements d_{a_i} were applied, ranging from 0 to 0.127mm in increments of 0.0254mm, limited by dial gage resolution. The rotation applied was counterclockwise for both in-plane and out-of-plane arrangements. Based on the rotation angles and on the pixel size, it is possible to attribute a value of expected displacement for every pixel in the image, related to its position relative to the center, where the displacement is zero. Figure 6-6 shows schematics of the rotation and the displacements generated in the X and in the Y directions.

The center of the image set to displacement zero and fixed as the origin. In the MATLAB, software used for processing in this research, the indexing of pixels is done from left to right, top to bottom, so the pixel (1,1) is at the top left corner. The region of interest set to the measurements is 700 (r) × 600(c) with the columns aligned with the X axis. The relation on Equation 6-14 was used in the software

$$\boldsymbol{P_s \begin{bmatrix} \alpha_1(350 - i_1) & \alpha_1(j_1 - 300) & 1 \\ \vdots & \vdots & 1 \\ \alpha_2(350 - i_{N+1}) & \alpha_2(j_{N+1} - 300) & 1 \\ \vdots & \vdots & \vdots \\ \vdots & \vdots & \vdots \\ \alpha_5(350 - i_{5N}) & \alpha_5(j_{5N} - 300) & 1 \end{bmatrix} \begin{Bmatrix} K_{r_y} \\ K_{r_x} \\ \vartheta \end{Bmatrix} = \begin{Bmatrix} \Delta\Theta_1 \\ \vdots \\ \vdots \\ \Delta\Theta_{5N} \end{Bmatrix}} \tag{6-14}$$

where P_s is the pixel size given by Equation 6-3. The sub index 5N seen in the Equation 6-14 means that a total of 5 different measurements were used, with different rotations, at the same time for the least squares procedure. The angle α was also measured five times, so the uncertainty in the measurement follows the trend of Equation 6-8.

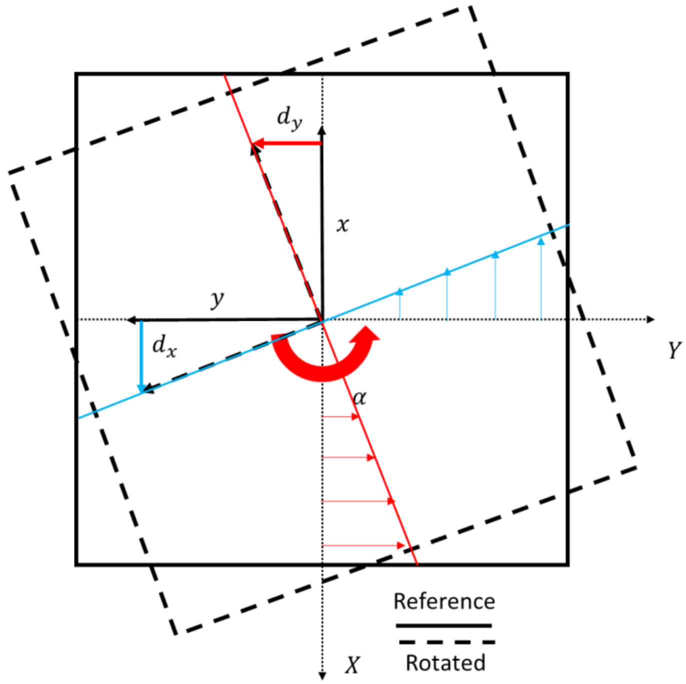

Figure 6-6. Pure rotation produces the same displacement pattern in both X and Y directions. For very small rotations, like in the case of rotations measurable by ESPI, the displacements d_y are essentially constant in any line parallel to Y, with the magnitude represented as a red line with arrows at the center. The same applies to the X direction, with the displacements shown in blue. The dashed square is a rotated version of the solid line square.

One measurement was added after the last one to create a pixel wise displacement matrix $5N \times 3$. Also notice that the values of α change according to the measurement index. The values of phase are obtained from measurements performed using the system. A total of 5 measurements for each axis, including 5 loading steps per measurement, were performed. The phases shown in Equation 6-14 are the averaged phase of the 5 different measurements.

The procedure is similar for the out-of-plane measurements. The only difference is that the displacements applied, d_z, are not linked with d_x and d_y. In that case, $d_y = 0$ and d_x is a constant displacement across the measurement area, and produces no fringes.

A sample that is not perfect can introduce out-of-plane rotations around the X axis as well. For the purpose of finding the sensitivity vectors in Z, it can be shown that the rotation around X do not interfere with the calculation. As stated previously, a rotation in a different plane than the principal produces a rotation of fringes. While the rotation around the X axis tilts the fringe map, it does not alter the slope of the ramp of displacements due to rotation in XY plane, around the Y axis.

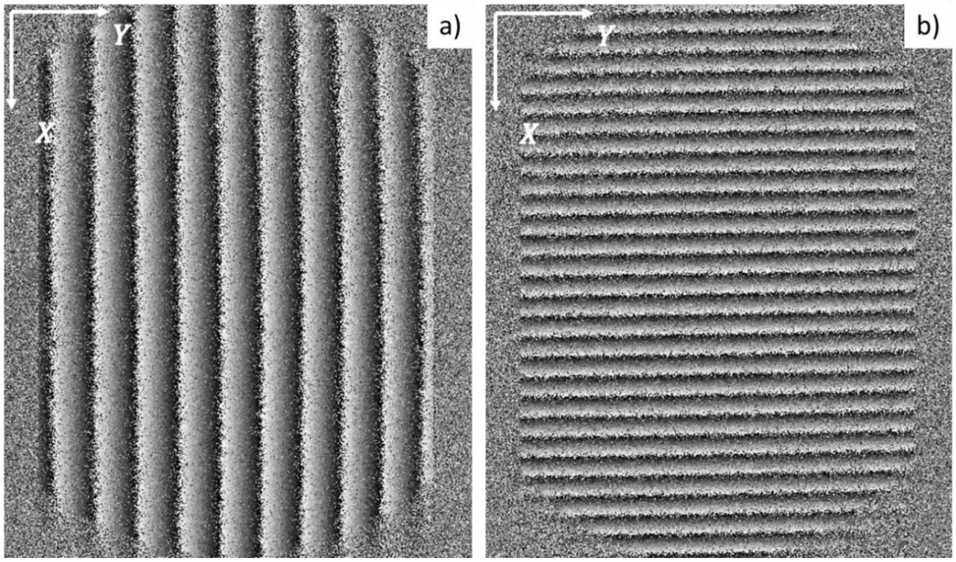

Figure 6-7. (a) In-plane measurement in the Xdirection. The rotation produces vertical fringes. The angle of rotation is $\alpha = 0.0106°$. (b) In-plane measurement in the Y direction. The sensitivity in this direction is larger and also the length of the region of interest is larger, producing considerably more fringes. For every two fringes, there is a relative displacement of 1.2µm in (a) in X direction. On (b), a relative displacement of 0.833µm in Y produces 2 fringes.

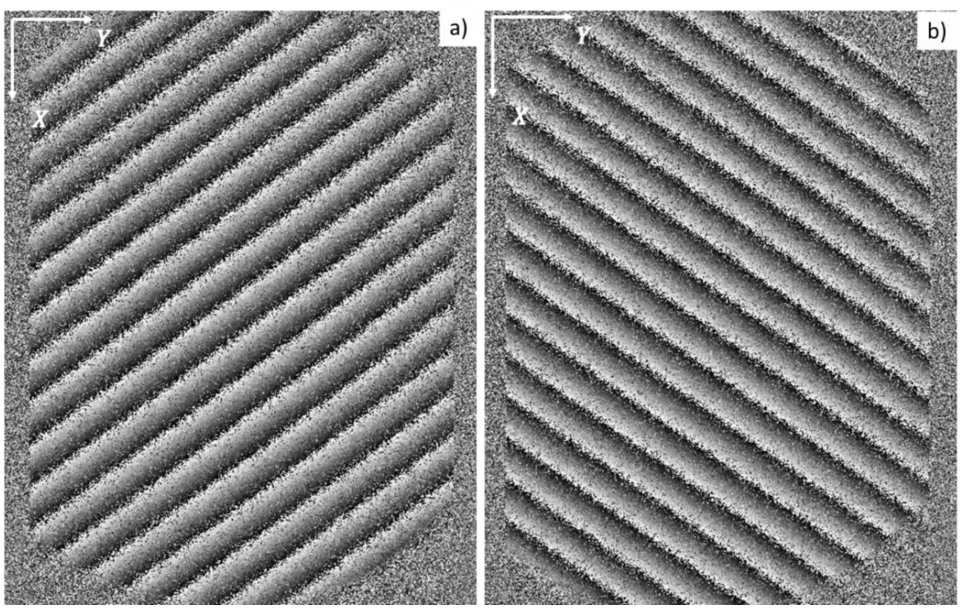

Figure 6-8. (a) In-plane measurement with diagonal sensitivity (K_3). (b) In-plane measurement with diagonal sensitivity (K_4). Both K_3 and K_4 point in the positive X direction, but K_3 points in the negative direction of Y while K_4 points to the positive Y. As the displacements are the same, the fringes rotate from (a) to (b).

Figure 6-7(a) shows a phase map acquired with sensitivity mostly in X for a level of rotation $\alpha_2 = -0.0106°$ in-plane. On Figure 6-7(b), the phase map with the sensitivity vector in the Y direction for the same level of rotation.

Figure 6-8(a) shows, for the same rotation, a phase map obtained with the sensitivity vector K_3. The fringes are inclined since the vector has a sensitivity in the diagonal and, for a pure rotation, d_x = d_y. The inclination angle is not 45° because the components of K_3 in X and Y are different. On Figure 6-8 (b), for the same rotation as before, the phase map is obtained with K_4. The orientation of the fringes has changed, as expected.

Before presenting the least square procedure, the simplified version of Equation 6-11 is

$$[\mathbf{D_a}]\{\mathbf{K_r}\} = \{\mathbf{\Delta\Theta}\} \tag{6-15}$$

where $[D_a]$ is a $5N \times 3$ matrix, $\{K_r\}$ is a 3×1 vector and $\{\Delta\Theta\}$ is a $5N \times 1$ vector.

In the least squares method, the central idea is to use all the data available to obtain the quantities of interest, in this case, the sensitivity components. Multiplying both sides by the transpose of $[D_a]$ the equation becomes

$$[\mathbf{D_a^T}][\mathbf{D_a}]\{\mathbf{K_r}\} = [\mathbf{D_a^T}]\{\mathbf{\Delta\Theta}\} \tag{6-16}$$

$[D_a^T][D_a]$ is a 3×3 matrix. By taking the inverse of $[D_a^T][D_a]$ and multiplying in both sides, the vector $\{K_r\}$ is isolated

$$\{\mathbf{K_r}\} = ([\mathbf{D_a^T}][\mathbf{D_a}])^{-1}[\mathbf{D_a^T}]\{\mathbf{\Delta\Theta}\} = [\mathbf{Q}]\{\mathbf{\Delta\Theta}\} \tag{6-17}$$

where $[Q]$ is a $3 \times 5N$ matrix. The vector $\{K_r\}$ contains the values of sensitivity in the X and Y direction. Equation 6-17 can be used for any of the axes and produce the values of the in-plane sensitivity components.

Table 0-1 shows the values of in-plane sensitivity calculated by the least squares method and the difference of the expected value, in percent.

In Table 0-1 shows that some of the axes are somewhat far from the expected values. The main issues are the number of angles to be adjusted in the interferometer assembly and the lack of a convenient way to measure them accurately. The adjustment of axis 4, for example, depends on the angles of 3 mirrors, each mirror having rotational degrees of freedom in two axes, the diffraction grating inclination itself, which can rotate in 3 axis, the laser centering in respect with the lenses and the lenses alignment with respect to the grating. The systematic alignment performed aimed to have all the incoming beams centered in the image, which introduced different incidence angles due to all alignment factors involved. It is interesting to notice that the residual components in $\mathrm{K_x}$ and $\mathrm{K_y}$ are small. In addition, the percent difference, excluding $\mathrm{K_{4_z}}$, are within $\pm$ 10%, with higher values for the out-of-plane components that are smaller compared to the in-plane components.

Table 0-1. Table showing values of the measure sensitivity vector components in comparison with the expected values.

Vector	X_m.[rad/μm]	X_c[rad/μm]	% dif.	Y_m[rad/μm]	Y_c.[rad/μm]	% dif.	Z_m.[rad/μm]	Z_m.[rad/μm]	% dif.
K_x	10.586	10.44	1.42	0.147	0	-	0.203	0	-
K_Y	-0.188	0	-5.50	14.254	15.08	-5.50	0.302	0	-
K_3	5.366	5.22	2.87	-7.2389	- 7.54	-3.98	1.964	2.16	-9.26
K_4	5.223	5.21	0.2	7.385	7.54	-1.99	-1.766	-2.16	18.06
K_5	5.422	5.22	3.83	-6.920	-7.54	-8.22	-2.107	-2.16	2.31
K_6	5.204	5.22	-0.38	7.091	7.54	-5.97	2.350	2.16	8.80

6.4 Measurement of deformation in a cantilever beam

The calibration device was useful for investigating the sensitivity components and their directions. A different sample was used to verify the functionality of the interferometer.

A slender beam made of brass, with length of 415$\pm$0.5 mm and a square cross section 12.70 $\times$12.70 mm, is clamped in one end. The free end was displaced by known amounts by the use of micrometer screws and spheres. The beam was loaded both in-plane and out-of-plane separately, and then with the displacements combined. The measurement results, obtained by the least squares method, is then compared to an analytical solution and FEA simulation.

6.4.1 Experimental apparatus

Figure 6-9 shows schematics of the apparatus. The beam is clamped by two thick supports, making a tight fit with the beam. The center of the measurement region was chosen to be at 40mm from the boundary between the beam and fixture. Thus, the incident light beams are not blocked by the clamping mechanism.

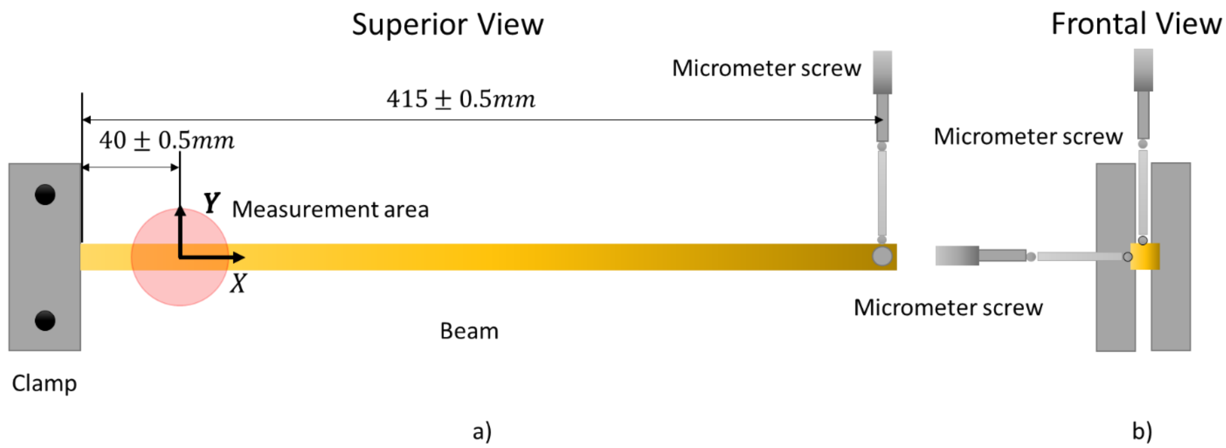

Figure 6-9. Schematics of a slender beam for in-plane and out-of-plane displacement. (a) Top view of apparatus. The length of the beam is much larger than its width and thickness. Displacements are applied by micrometer screws. (b) Frontal view showing the second micrometer screw used for out-of-plane displacements.

The free end of the beam is fitted with two small spheres positioned at 375 mm from the measurement area. One of the spheres is attached to the side of the beam, so a micrometer screw pushes the beam sideways to produce an in-plane displacement at the bending region. The second sphere was positioned on top of the beam, at same distance from the clamping boundary. A second micrometer is used to load the beam from the top, thus producing an out-of-plane displacement. The resolution of the micrometers is 0.01mm. This displacement-controlled arrangement is used so that the displacements in the measurement area do not depend on the material properties. The displacements seen on the beam at the measuring region are proportional to the displacements applied at the free end and the relation is known to be cubic.

Figure 6-10 shows a photograph of the actual apparatus. The loading mechanism is composed of the spheres, the micrometer screw and the rod that connects the micrometer to the beam. The rod is necessary to reduce effects of friction. Small misalignments in the micrometer screw cause the screw to rotate of the center of the sphere. The result is that the sphere wanders around, causing undesirable displacements and affecting the measurement. There is also an effect of hysteresis that is minimized when using the rod. The rod is free to rotate and can only exert a normal force in the beam. Any sideways force causes the rod to rotate, releasing the pressure right away and thus avoiding secondary displacements.

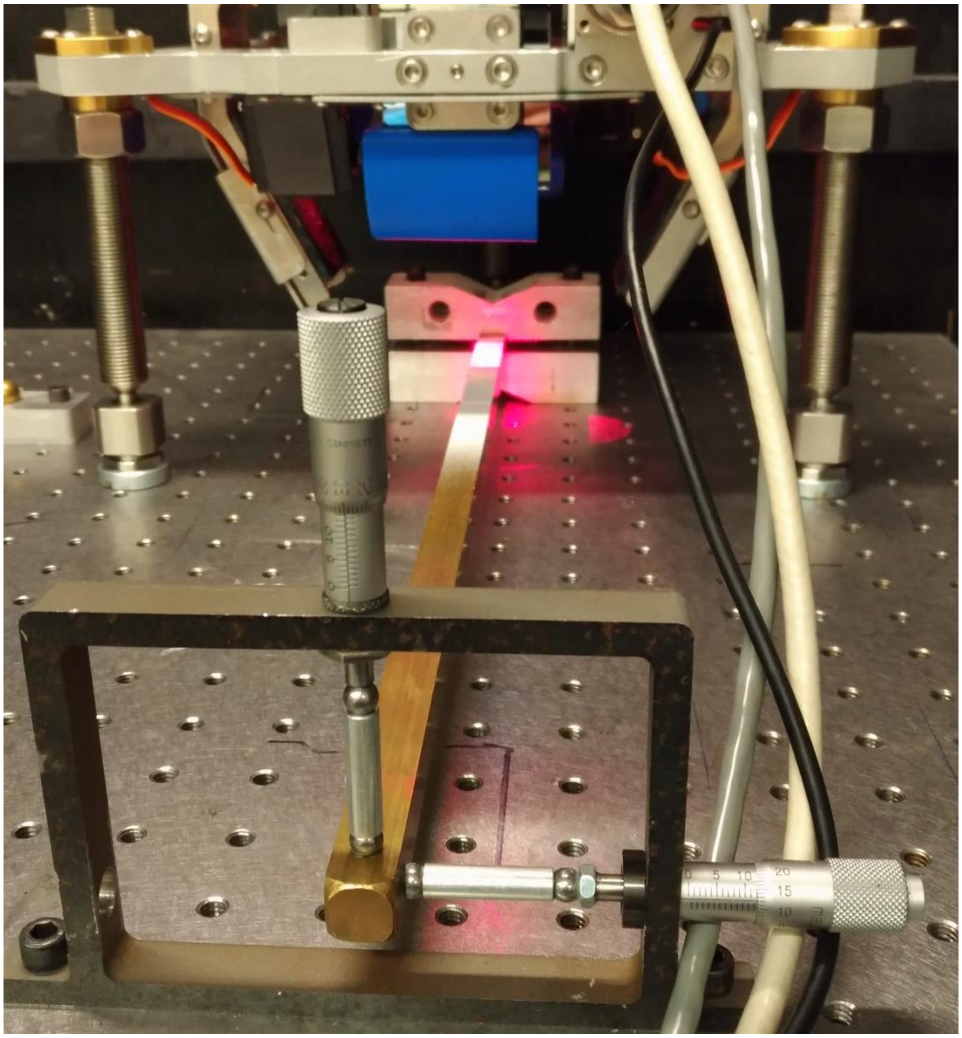

Figure 6-10. Photograph of the actual beam used for 3D displacement measurements. The micrometer screws for loading the sample are see near the bottom. The measurement area is illuminated by the laser near the top.

The displacements applied on the beam can be classified onto three different categories: in-plane motion with loading and unloading cycle; out-of-plane motion with loading and unloading; both in-plane and out-of-plane motions applied at the same time. The beam, which is deformed in the elastic domain, is expected to obey the superposition principle. Measuring in-plane and out-of-plane separately and adding the results should yield the same results as obtained when loading in-plane and out-of-plane at the same time.

A total of 5 measurements for each category of displacement was taken, with 5 steps for loading and 5 steps for unloading.

6.4.2 Analytical solution – a comparison

The bending of the proposed beam is described by the elastic bending theory. As the beam is very long compared to its cross-section dimensions, it is possible to neglect shear effects. The Euler-Bernoulli bending equation is used to determine the bending shape

$$\frac{\mathbf{EI\partial^2 w(x)}}{\mathbf{\partial x^2}} = \mathbf{M(x)} \tag{6-18}$$

The solution of the equation for a long slender beam with one end fixed is []

$$\mathbf{w(x)} = \frac{\mathbf{Px^2(3L-x)}}{\mathbf{6EI}} \tag{6-19}$$

At the end of the beam, the displacement is simply

$$\mathbf{w(L)} = \frac{\mathbf{PL^3}}{\mathbf{3EI}} \tag{6-20}$$

It is possible to have $\mathrm{w(x)}$ as a function of $\mathrm{W(L)}$, which is the displacement applied, and x. Dividing both sides of 6-19 by $\mathrm{w(L)}$

$$\frac{\mathbf{w(x)}}{\mathbf{w(L)}} = \frac{\mathbf{x^2(3L-x)}}{\mathbf{2L^3}} \tag{6-21}$$

The displacements along the beam are then a function of the applied displacement $\mathrm{w(L)}$ at the free end of the beam. This enables a comparison of the measured deformations with the analytical model without the knowing specifics about the material properties or force applied. Equation 6-21 is for an out-of-plane displacement of the beam in the Z direction. The same equation can be used for displacement in the Y direction, for $\mathrm{v(x)}$ which is the in-plane bending.

The beam used in this study was measured with the center of the region of interest 40mm away from the clamping boundary. The pixel size had to be corrected since the beam's surface is at a difference height compared to the calibration device. The new pixel size is $P_s = 0.0444$mm. The region of interest is 904 (r) x 260 (c) pixels, so the length in mm in the longer dimension is $L_m = 40.1 \pm 0.1$. These values need to be known when comparing Equation 6-21 with the experimental data on section 6.4.5.

6.4.3 Validation with FEA simulations

A COSMOS finite element model was implemented to simulate the beam under bending and validate the measurements.

The required simulation is not dependent on the material properties, except one. The Poisson's ratio has to be known. The Poisson ratio used was $\nu = 0.318$. The Poisson ratio is responsible for transversal displacements in the cross section of the beam. The surface of the beam that is under tension experiences a width reduction. The surface under compression in the longitudinal direction experiences a width increase. The analytical model presented here is based in the assumption that the cross sections are not affected by the bending. The Analytical model is used mostly to check the validity of the finite element simulations.

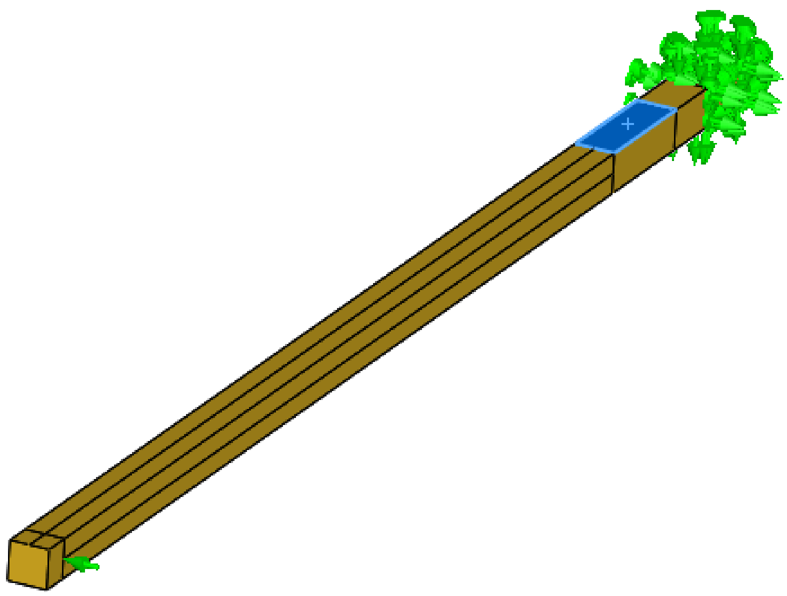

Figure 6-11. FEA model with fixed boundary conditions on right upper side and displacement applied on left bottom side.

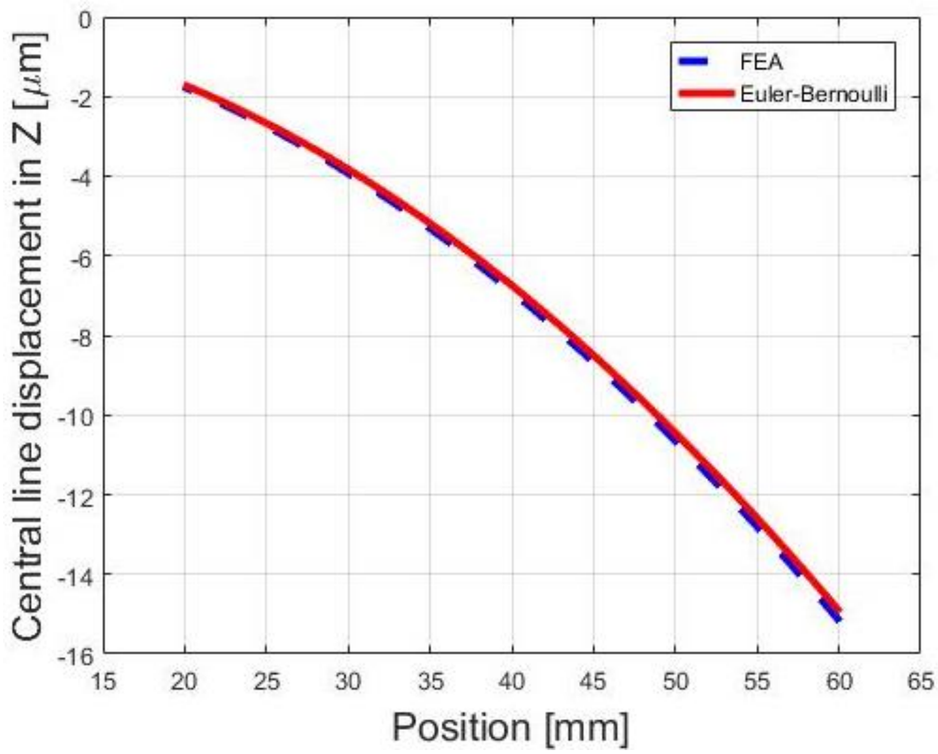

Figure 6-12. Comparison between Euler-Bernoulli and FEA results for out-of-plane displacement.

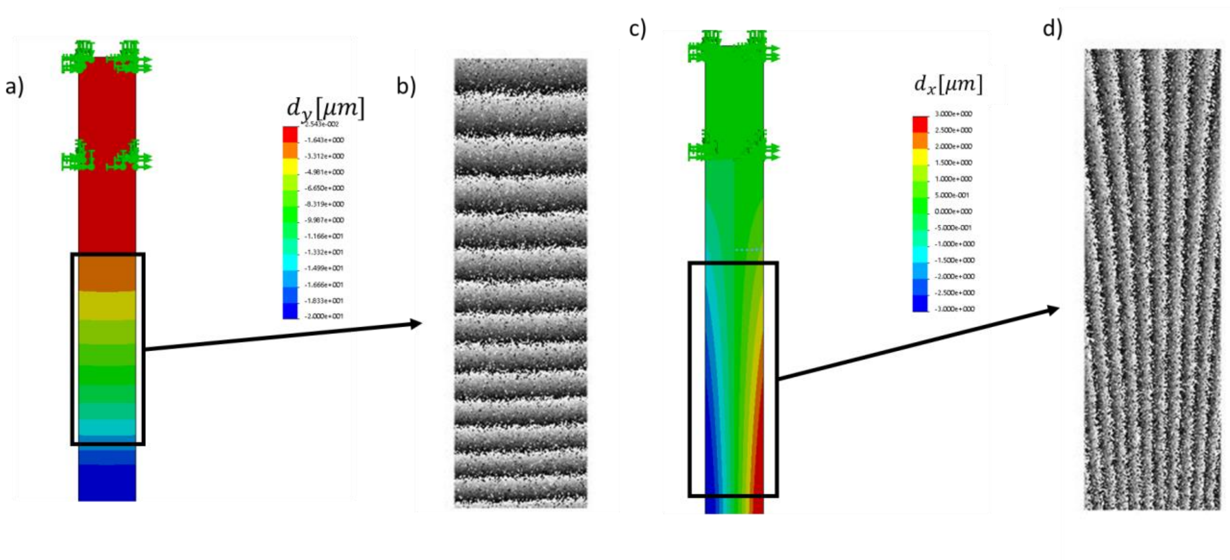

Figure 6-13. Visual comparison between the shape of deformation on FEA and the phase maps for in-plane X and Y displacements. (a) FEA displacement in the Y direction (horizontal). Colors represent positions of equal displacement. (b) Phase map of deformation in the Y direction. Fringes represent sets of points with equal displacement. (c) FEA displacement map on X direction (vertical). (d) Phase map on X direction. The black rectangle in (a) and (b) represents the region of interest used for the ESPI measurements.

Figure 6-11 illustrates the model and the boundary conditions used. The displacement field was obtained for all the three Cartesian components within the region of interest. The simulated value agrees well with the result from the Euler-Bernoulli solution. In Section 6.4.5**Error! Reference source not found.**, the experimental results are compared with simulated results by finite element analysis.

6.4.4 Data averaging – Least squares method

Several measurements were performed to verify the repeatability of the interferometer. In addition, the multiple measurements can be used for averaging and thus reducing the uncertainty. The use of all the data from the six axes is also investigated in this section.

The method of least squares is used in a slightly different way to obtain three displacement components separately. The displacements now are the unknowns instead of the sensitivity vector coordinates. The sensitivity vectors are known and the redundant data can be used for averaging. Recalling Equation 6-22, the relation can be modified replacing $[\mathrm{K}]$ by $[\mathrm{K_m}]$ which is the new sensitivity matrix. The multiplication of both sides of the equation by the transpose of $[\mathrm{K_m}]$ and subsequente multiplication by the $([\mathrm{K_m^T}][\mathrm{K_m}])^{-1}$ yields the displacement vector in the left side and the matrix $[\mathrm{Q}]$ times the measured phases in the right side

$$\{\mathbf{d}\} = ([\mathbf{K_m^T}][\mathbf{K_m}])^{-\mathbf{1}}[\mathbf{K_m}]\{\mathbf{\Delta\Theta_m}\} = [\mathbf{Q}]\{\mathbf{\Delta\Theta_m}\} \tag{6-23}$$

The new matrix $[\mathrm{Q}]$ is a 3×6 matrix of constant elements. Equation 6-19 can be used in all of the pixels of a phase map one at a time. The advantage of this method is that it already does the averaging of all the available measurements. The method can also be used in a reduced form, with only three sensitivity vectors, for example. On this study, some of the combinations will be investigated and compared with the case where all the vectors are used. Both results will then be compared to the analytical result and to FEA simulations.

At least three measurements with different sensitivities are necessary to determine a 3D displacement map completely. In the case of this interferometer, several combinations are allowed. The least squares method will be used in a sequence of combinations, thereby allowing the 3D displacement map of a specific measurement to be calculated. Different combinations will be used to investigate the effect of data averaging and the consistency of the results obtained by different axes combinations.

Table 0-2 shows a list of combinations to be used. 2 different combinations of 3 vectors and a third combination encompassing all of the sensitivity vectors. The consistency of the results can will also be evaluated by a comparison with the FEA and analytic solutions.

Table 0-2. Combinations of vectors used for checking the least squares method

Combination			
1	K_x	K_y	K_3
2	K_3	K_4	K_5
3	All		

From 5 available measurements, the first one was picked to be analyzed. To keep the analysis compact, only two loadings will be analyzed. The first loading case is with a 0.2mm displacement applied both in-plane and out of plane at the free end of the beam. For the second loading case the displacement applied is 0.5mm, both in-plane and out-of-plane.

Figure 6-14 shows the comparisons of the displacements in the x direction, i.e., along the longitudinal axis of the beam for the measurement described above for the first loading case. The colors represent the motion of the beam surface in the longitudinal direction (vertical in the figure).

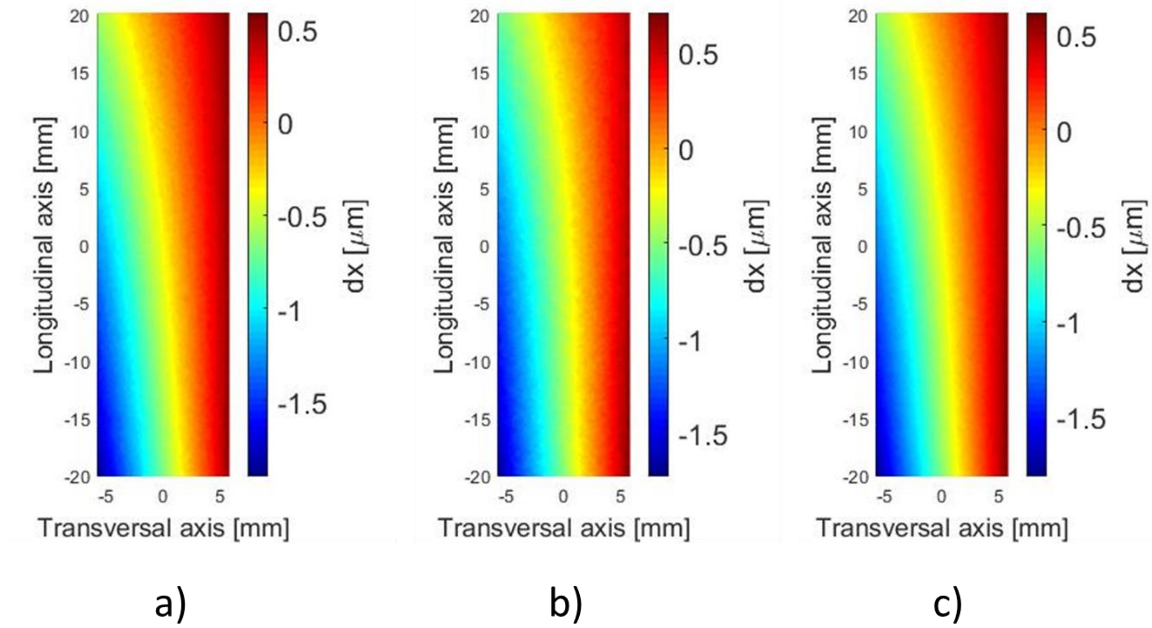

Figure 6-14. In-plane motion in the X direction calculated with three different sensitivity vector combinations. (a) Combination of $\mathbf{K_x}$, $\mathbf{K_y}$ and $\mathbf{K_3}$. (b) Combination of $\mathbf{K_3}$, $\mathbf{K_4}$ and $\mathbf{K_5}$. (c) Combination of all available sensitivity vectors.

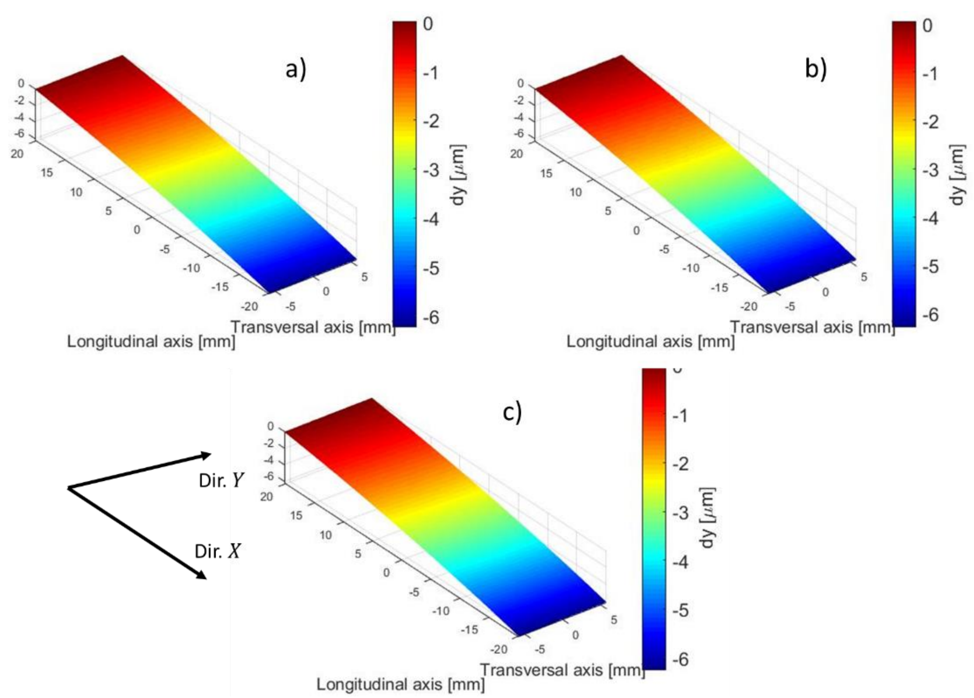

Figure 6-15. Displacements in the Y direction (see coordinates on Figure). The height of the curves is proportional to the displacement in the Y direction. (a) Combination of $\mathbf{K_x}$, $\mathbf{K_y}$ and $\mathbf{K_3}$. (b) Combination of $\mathbf{K_3}$, $\mathbf{K_4}$ and $\mathbf{K_5}$. (c) Combination of all available sensitivity vectors.

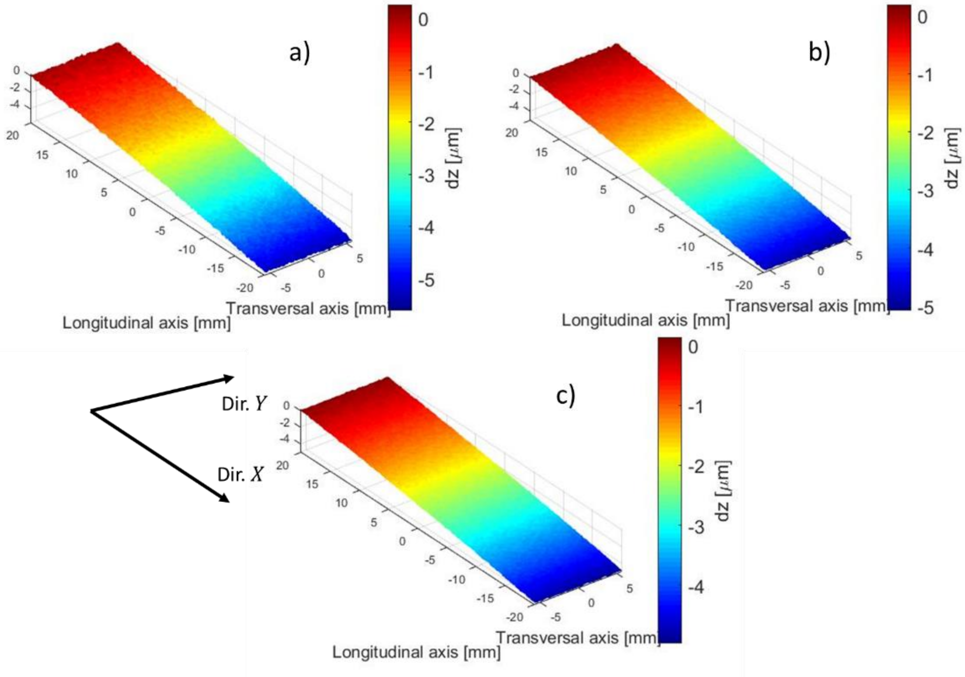

Figure 6-16. Displacements in the Z direction (orthogonal to Y and X). The height of the curves is proportional to the displacement in the Z direction. (a) Combination of K_x, K_y and K_3. (b) Combination of K_3, K_4 and K_5. (c) Combination of all available sensitivity vectors.

Figure 6-15 Figure 6-16 show the displacements in Y and in Z. All the measurements are consistent with each other. This can be attested by looking on Figure 6-17 the differences between the combination with all the six sensitivity vectors and the other two combinations of vectors.

The difference in Figure 6-17(e) represents the difference between combination 3 and combination 1 (see Table 0-2) is slightly higher.

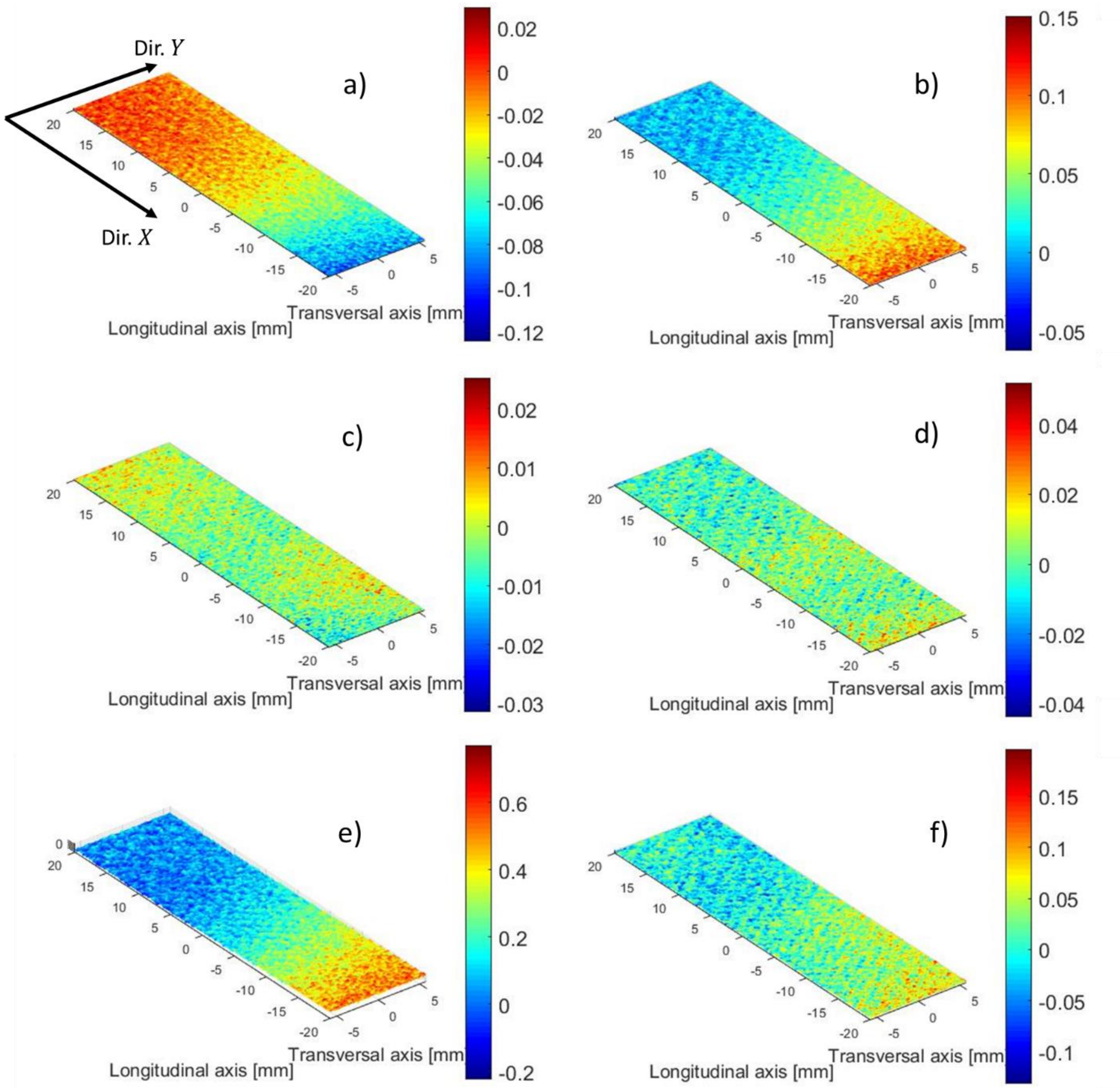

Figure 6-17. Difference between combination 3 (c3) with combination 1 (c1) and combination 3 with combination 2 (c2). (a) Difference between c3 and c1 for displacements in X. (b) Difference between c3 and c2 for displacements in X. (c) Difference in Y direction between c3 and c1. (d) Difference in the Y direction between c3 and c2. (e) Difference in the Z direction between c3 and c1. (f) Difference in the Z direction between c3 and c2.

For the second loading case, the displacements in the X, Y and Z directions are also shown in Figure 6-18. In-plane motion in the X direction calculated with three different sensitivity vector combinations for second loading case (0.5mm applied displacement). (a) Combination of $\mathbf{K_x}$, $\mathbf{K_y}$

K3. (b) Combination of **K3**, **K4** and **K5**. (c) Combination of all available sensitivity vectors. Figure 6-18, Figure 6-19 and Figure 6-20, respectively. There are unwrapping errors close to X=-20mm in the measurements of d_x (Figure 6-19) and d_z (Figure 6-20). The differences between the combination of vectors 3 (c3) with combination of vectors 1 (c1) and c3 with the combinations of vectors 2 (c2) is shown on Figure 6-21.

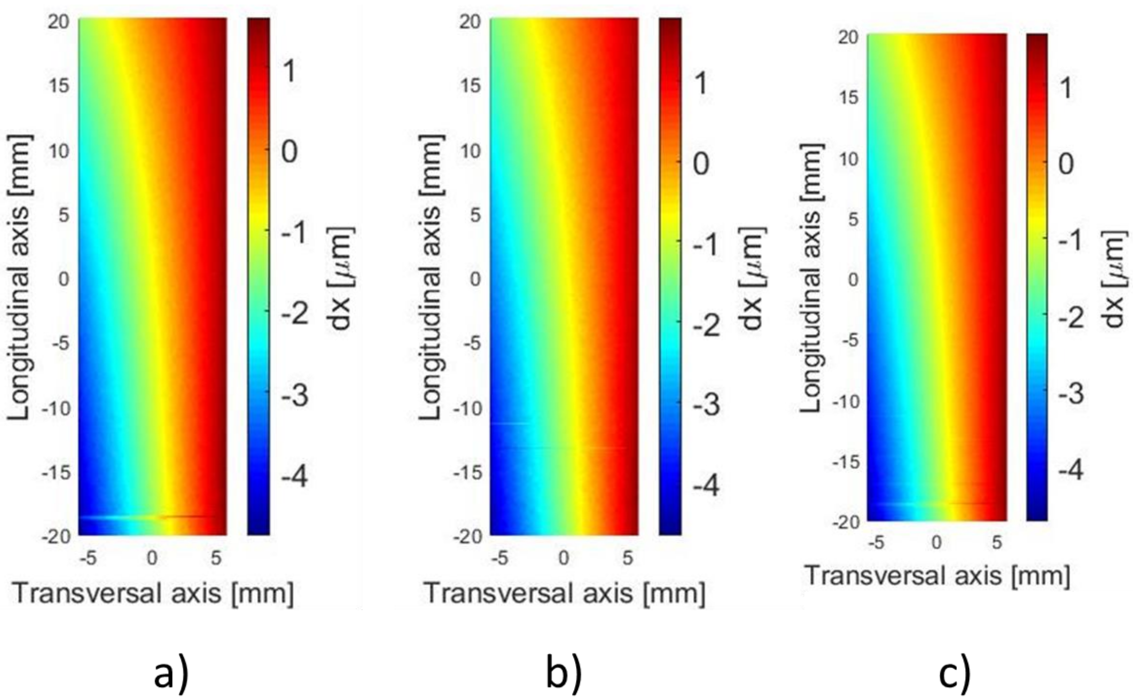

Figure 6-18. In-plane motion in the X direction calculated with three different sensitivity vector combinations for second loading case (0.5mm applied displacement). (a) Combination of K_x, K_y and K_3. (b) Combination of K_3, K_4 and K_5. (c) Combination of all available sensitivity vectors.

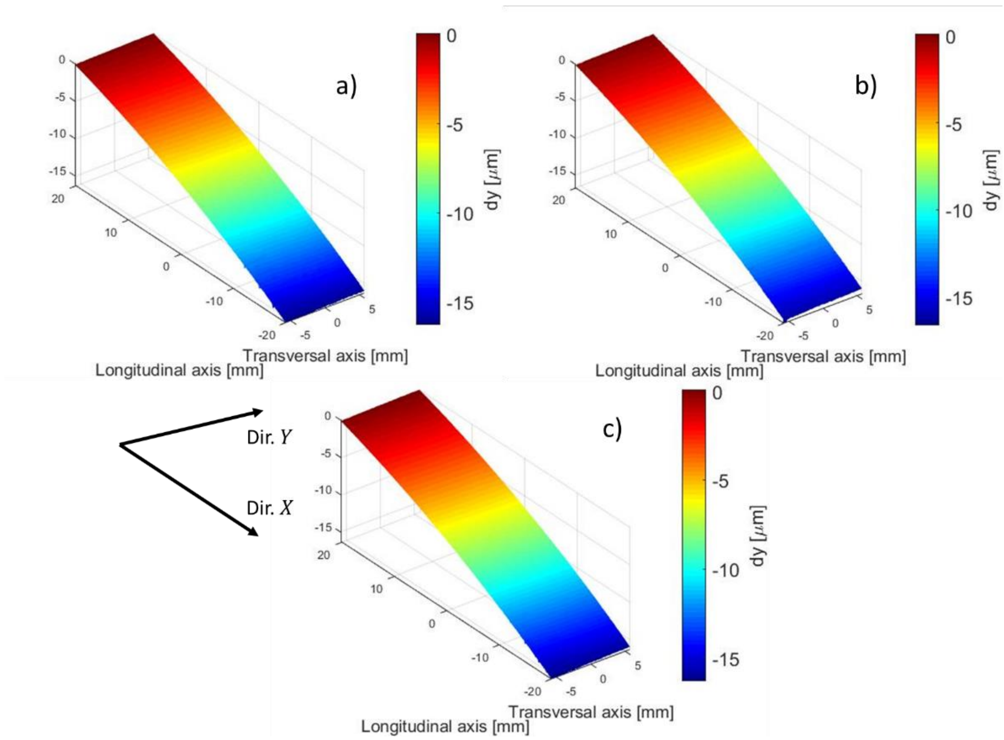

Figure 6-19. Displacements in the Y direction (see coordinates on Figure) for second loading case. The height of the curves is proportional to the displacement in the Y direction. (a) c1. (b) c2. (c) c3

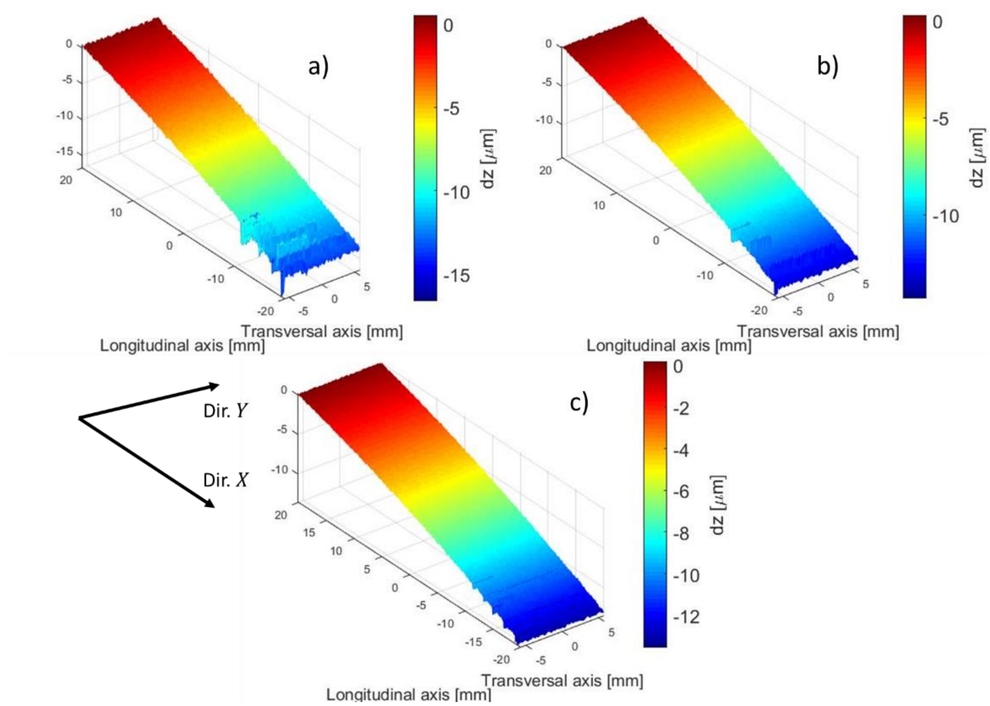

Figure 6-20. Displacements in the Z direction (orthogonal to Y and X) for second loading case. The height of the curves is proportional to the displacement in the Z direction. (a) c1. (b) c2. (c) c3.

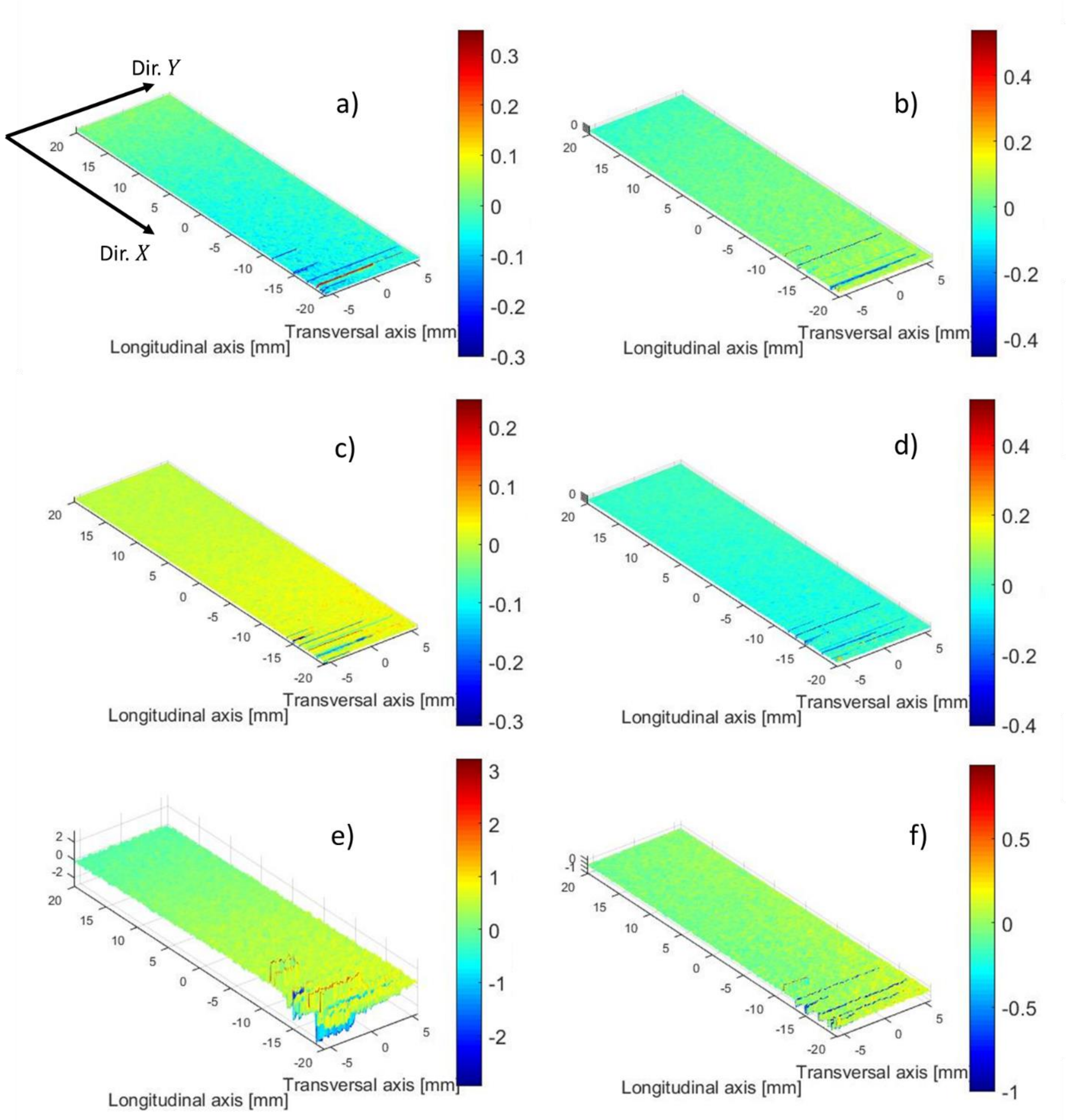

Figure 6-21. Difference between combination 3 (c3) with combination 1 (c1) and combination 3 with combination 2 (c2) for the second loading case (0.5mm applied displacement). (a) Difference between c3 and c1 for displacements in X. (b) Difference between c3 and c2 for displacements in X. (c) Difference in Y direction between c3 and c1. (d) Difference in the Y direction between c3 and c2. (e) Difference in the Z direction between c3 and c1. (f) Difference in the Z direction between c3 and c2.

As expected, the results show good agreement between the measurements with different sensitivity combinations. There is no significant influence of different sensitivities in the axes, specially the out-of-plane axes $\mathbf{K_3}$ to $\mathbf{K_6}$. The calibration process was capable of equaling the measurements by compensating for deviations. There is however, a higher difference when it comes to the combination of vectors 1, which includes $\mathbf{K_x}$, $\mathbf{K_y}$ and $\mathbf{K_3}$. In order to investigate it further, a different measurement was picked and both combinations 1 and 3 are compared again. The measurement picked is the 3rd measurement performed with composed in-plane and out-of-plane displacements.

Figure 6-22(a) shows again the plot seen on Figure 6-17(e), a difference between the combination 3 result with the combination 1 result for an out-of-plane displacement $\mathbf{d_z}$ and load of 0.2mm. Figure 6-22(b) shows the same results for the measurement 3. The apparent systematic error seen in Figure 6-22figurexx(a) is not visible in Figure 6-22(b).

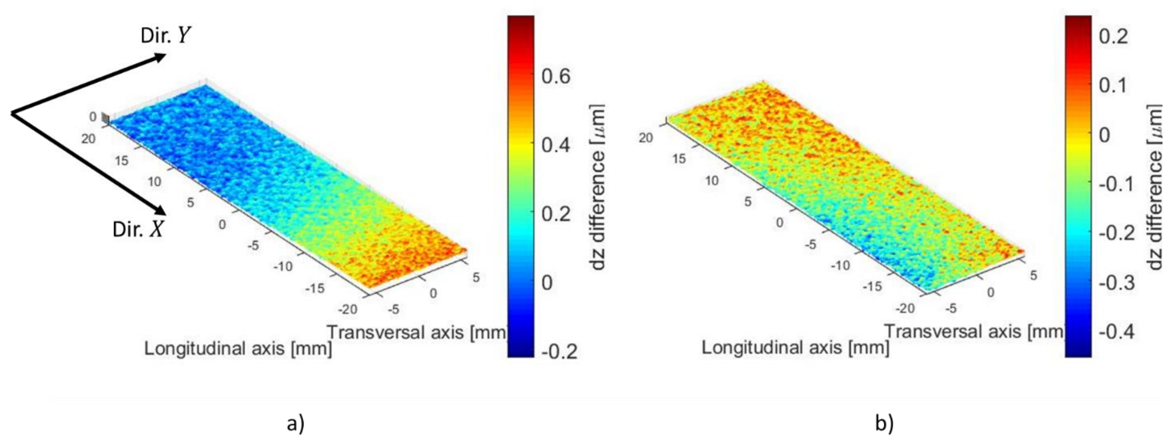

Figure 6-22. (a) Difference on $\mathbf{d_z}$ between c3 and c1 for measurement 1 and for the loading case 1 (0.2mm displacement applied on beam). (b) Difference on $\mathbf{d_z}$ between c3 and c1 for measurement 3 with loading case 1. The inclination seen on (a), which appears to be systematic, disappears on measurement.

The important point is that the least squares method allows to use the sensitivity arrangement that is more suitable for an specific application. There might be cases where it is not necessary or not even possible to use all the six axes for a complete 3D measurement. In that case, it is desirable that any 3 of the six axes can be used to obtain the 3D displacement map. The comparison showed very good agreement between the three combinations of sensitivity vector.

6.4.5 Validation

The analytical solution and the finite element model presented on sections 6.4.2 and 6.4.3 agreed very well. On this section, the FEA solution is used to validate the results from the measurements. The 5 measurements were used to generate an arithmetic average. The load steps 5 (0.5mm) was picked as one example.

The comparisons will follow the sequence

- In-plane case compared to Finite Element Analysis (FEA);
- Out-of-plane case compared to FEA;
- Composed loading compared FEA;

6.1.a.1 In-plane

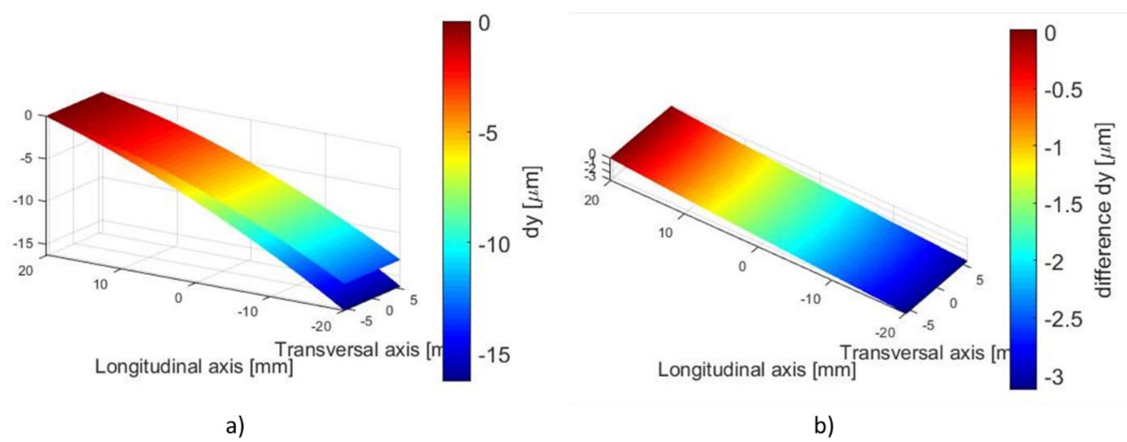

Figure 6.1.a.1-1. (a) Displacement field d_y calculated by FEA (top) and measured by ESPI (bottom). The measured values are around 3μm in difference compared to the simulated case. The Y direction is in-plane direction perpendicular to the longitudinal axis of the beam. (b) Difference (measured minus calculated) between calculated and measured displacements The difference is zero at X=20mm because the reference point is on the 20mm line.

Figure 6.1.a.1-1(a) shows that, in the **Y** direction, there is an error of around **3μm** for a total displacement of 15**μm**. The plots meet at zero since the offset was removed. The measurement in ESPI is relative so differences that are offsets have no meaning. The difference of 3**μm** represents an error of 20%, which is considerable. Figure 6.1.a.1-1(b) shows that the error

follows a linear trend. The difference between the measured displacements and the simulated is linearly dependent of position in the longitudinal axis. This suggests that there could be a residual rotation being measured together with the bending of the beam. One of the possible reasons for this residual rotation is imperfection of the clamp, so the beam can move or slip inside the clamping channel.

For the case of displacement in the **X** direction, the displacements are plotted in a different way. Due to limitations on software, it was not possible to generate a 3D map of deformations to be compared directly to the measured data. Thus, three lines were picked and the displacements were measured on those lines and compared with the displacement of an equivalent line in the solution of FEA. Figure 6.1.a.1-3 shows the plots of FEA and the plots for the measured data. As the measured data is referenced for a zero displacement at the clamp, the zero displacement line (red), corresponding to the neutral line, matches perfectly with the measured data. The results seen on the lower and upper curves present differences when compared to the FEA curves. Figure 6.1.a.1-2 shows schematics of the lines picked. The central line and 2 lines, one on each side, 3.2mm away from the neutral line

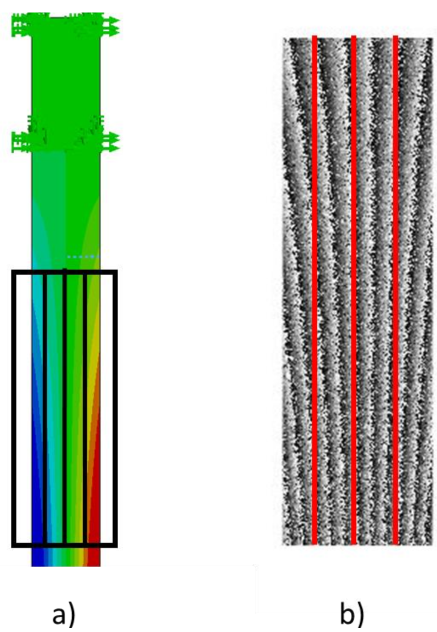

Figure 6.1.a.1-2 (a) schematics of the position of the lines used to generate the curves for comparison with the displacement map in the X direction duet to in-plane deformation.

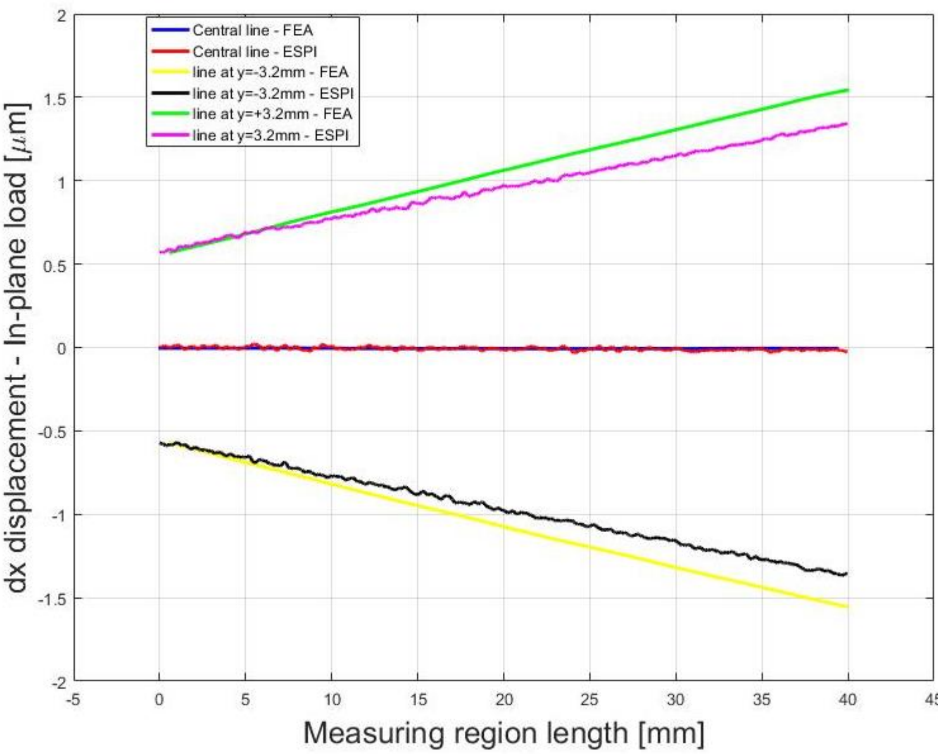

Figure 6.1.a.1-3. Contour plots for the displacement in the X direction due to a load in the Y in-plane direction. The two lines at the center rest in the neutral axis and therefore the displacement is zero. The green and magenta lines (top) are from points 3.2mm away in the from the neutral line in the Y direction. The ESPI value is slightly smaller. At the bottom, the lines from the symmetric position ($Y = -3.2mm$). The ESPI line is also smaller in magnitude.

6.4.5.1 Out of plane

The out-of-plane measurements in the case of out-of-plane loading showed very nice agreement with the expected results from finite element simulation. The error range is smaller then one micrometer for a total displacement of 15 micrometers. Figure 6.1.a.1-4(a) shows the two surfaces, measured and simulated, in the same plot. They overlap with very small differences, as can be seen on Figure 6.1.a.1-4(b). The differences are of less than 6%. This result also suggests that the clamp has better stiffness for out-of-plane bending of the beam.

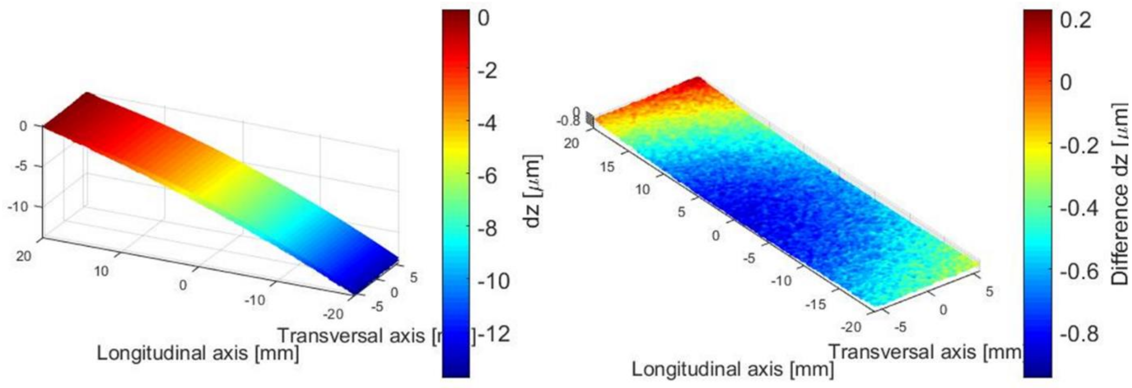

a) b)

Figure 6.1.a.1-4. (a) out-of-plane comparison between finite element calculation and the measurement. Both FEA and measurement data overlap. (b) The differences are very small compared to the level of displacement measured.

6.4.5.2 Combined loading

The combination of loads showed to be challenging from the point of view of comparison between the simulated displacements and the measured displacements. There are effects on the measurement that can be explained by factors such as the sample not behaving as expected, or the geometry of the sensitivity arrangements not being fully well determined.

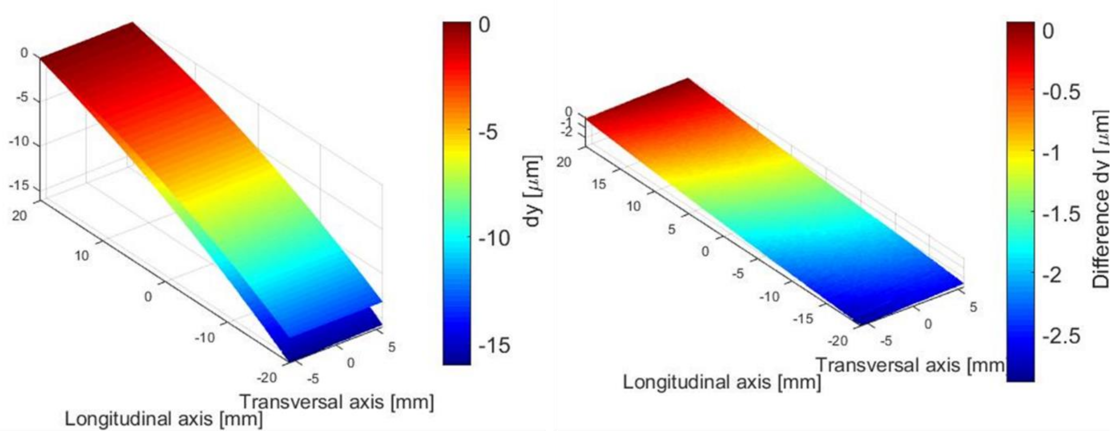

a) b)

Figure 6.1.a.1-5. (a) Displacements in the Y direction. The measured displacement is larger, and therefore is shown at the bottom. (b) Differences range from 0 to -2.5 micrometers.

Figure 6-28 shows that there is an error between the measured displacements and the expected values. The difference is in the range 0 to 3 micrometers for a total displacement of 15 micrometers. In the displacements on **X** direction, where the magnitudes are smaller, the effect is more evident.

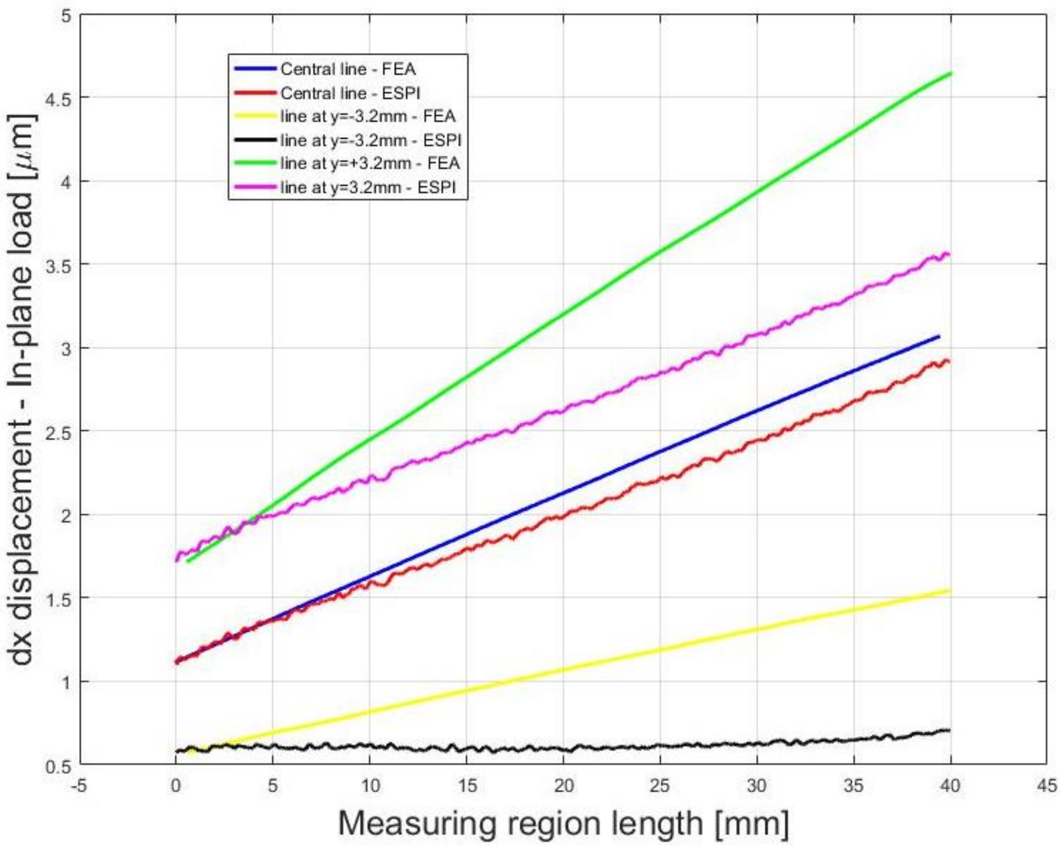

Figure 6.1.a.1-6. Contour lines for the displacements in the X direction. The results do not agree with the simulations. Further investigation is here needed.

While the in-plane measurement presents errors in the order of 20%, the out-of-plane measurements show very good agreement. The errors are of the order of 2 % to 6 %. Figure 6.1.a.1-7(a) shows the two surfaces, simulated and measured, in the same plot with almost perfect overlap. Figure 6.1.a.1-7(b) shows the error between the simulated and the measured. Again, the out-of-plane results have very good agreement with the simulations, which further suggests that the clamp used is very stiff for the out-of-plane loading while allowing rotation or movement of the beam in the in-plane directions.

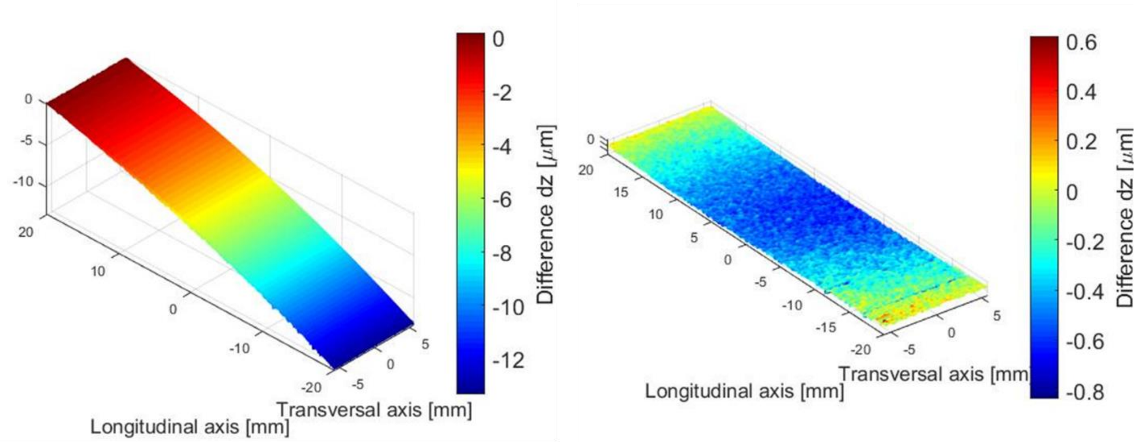

a) b)

Figure 6.1.a.1-7 (a) Out-of-plane displacements overlap with the simulation results. (b) Errors vary from 0.6 to -0.8 micrometers in a range of measurement of 15 micrometers.

The results demonstrated the ability of measuring displacements in the in-plane and the out-of-plane directions. The in-plane results suffer from larger deviations when compared to the simulation results. One possibility is that the sample is deforming in a different way than expected. A second possibility is that the calibration process did not achieve the level of accuracy necessary for the sensitivity component estimation. A better calibration device would have to be used to correct for this problem.

The next chapter summarizes the important points of this study. A brief discussion on the important questions that were raised and answer is given. Suggestions for future work are given at the end.

Chapter 7: Discussion, concluding remarks and future work

7.1 Multi-axial arrangement for 3D displacement measurements

The main focus of this study was to investigate the possibility of transforming a dual-axis arrangement, i.e., with sensitivity in two main directions, into a multi-axial arrangement capable of the measuring all three Cartesian components of displacement.

The usual approach for 3D measurements is to use several independent out-of-plane arrangements and then combine all the measurements to obtain a 3D deformation map. Alternatively, complex combinations of in-plane and out-of-plane sensitivity directions can be used and obtain the complete displacement map. These approaches, while well stablished, require large number of components. They are complex assemblies and demand sophisticated lasers to work.

The arrangement proposed and demonstrated in this study uses straightforward elements such as a laser diode and a diffraction grating together with geometric control to obtain the 3D displacement maps. In Chapter 4 it was shown that the use of two in-plane configurations with different sensitivities opens the possibility for the creation of extra four sensitivity arrangements. The extra arrangements, or axes, allow the measurement of the out-of-plane component of displacement.

The use of the diffraction grating made it possible to split the beam with reduced complexity and at the same time, facilitated the geometric control for improved performance of the laser diode as a light source for ESPI.

In Chapter 6: it was demonstrated that the redundant measurements can also be used for data averaging. The least squares method was used to obtain the information about the 3D deformation of the surface. Moreover, it was demonstrated that it is possible to use several different combinations of sensitivity vectors and obtain the same results. The use of more axes, however, provides a smoother and less prone to noise measurement.

The prototype system was found to give good measurement repeatability. Figure 7-1 shows the standard deviation of the 5 measurements for the in-plane loading of 0.5mm at the load application. Figure 7-1(a) shows the standard deviation of all measurements for the displacement component d_x. The deviations are standard deviation is smaller than 0.05μm in almost the whole measurement region. Figure 7-1(b) and Figure 7-1(c) show the standard deviations for d_y and d_z. In the case of d_y, the deviations are larger close to the base since the displacement are smaller and the measurement noisier. The deviations are smaller 0.2µm. For d_z, there is an unwrapping error that introduces high variations, but almost the totality of the points have deviations smaller than 0.1µm.

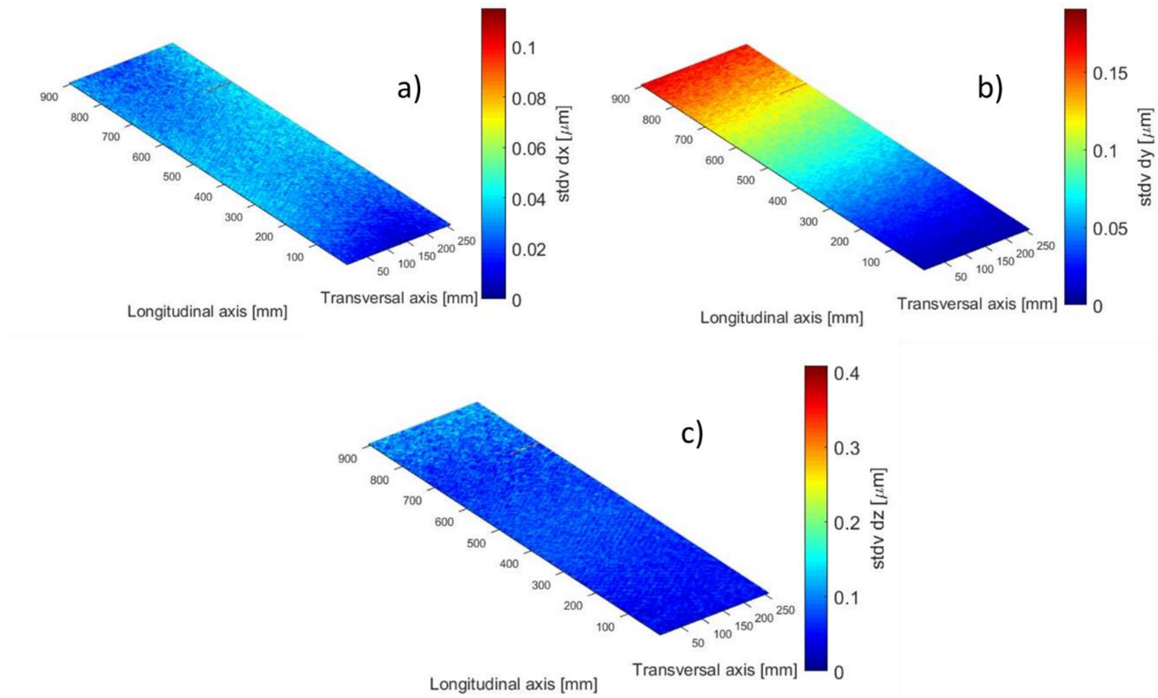

Figure 7-1. (a) Standard deviation for d_x in the in-plane loading case. (b) Standard deviation of d_y in the in-plane loading case. (c) Standard deviation of d_z in the in-plane loading case.

On Figure 7-2 and Figure 7-3, the same analysis is performed for the out-of-plane and the combined loading cases. The deviations are always contained within 0.3µm and the measurements can be considered to be repeatable.

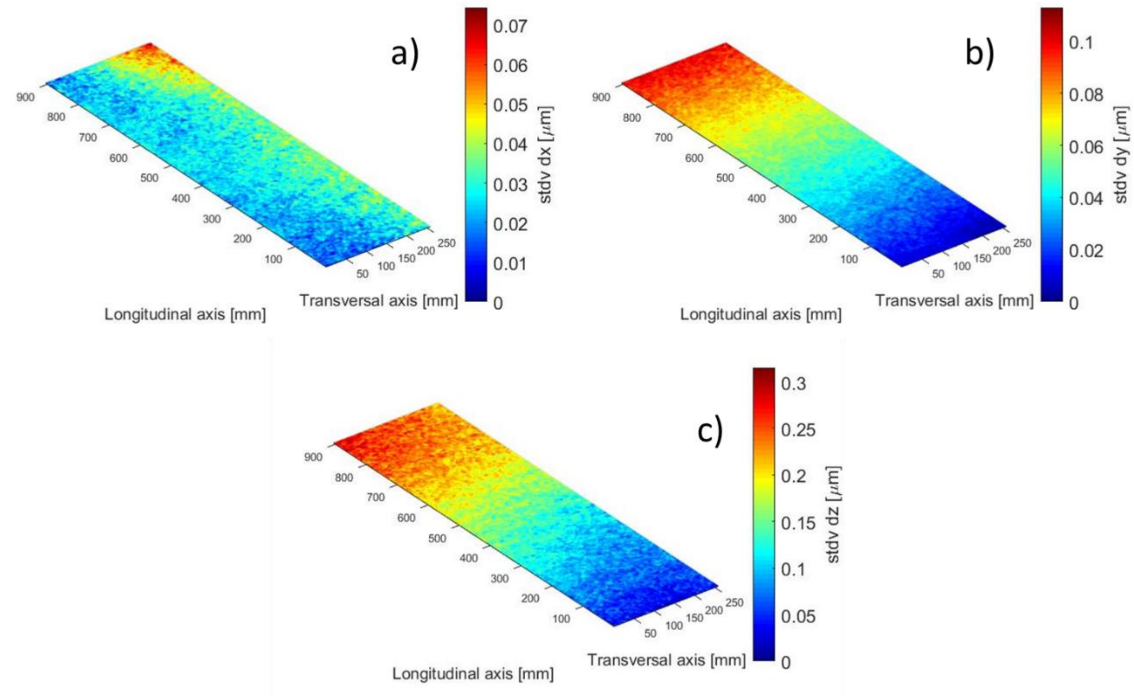

Figure 7-2. (a) Standard deviation for d_x in the out-of-plane loading case. (b) Standard deviation of d_y in the out-of-plane loading case. (c) Standard deviation of d_z in the out-of-plane loading case.

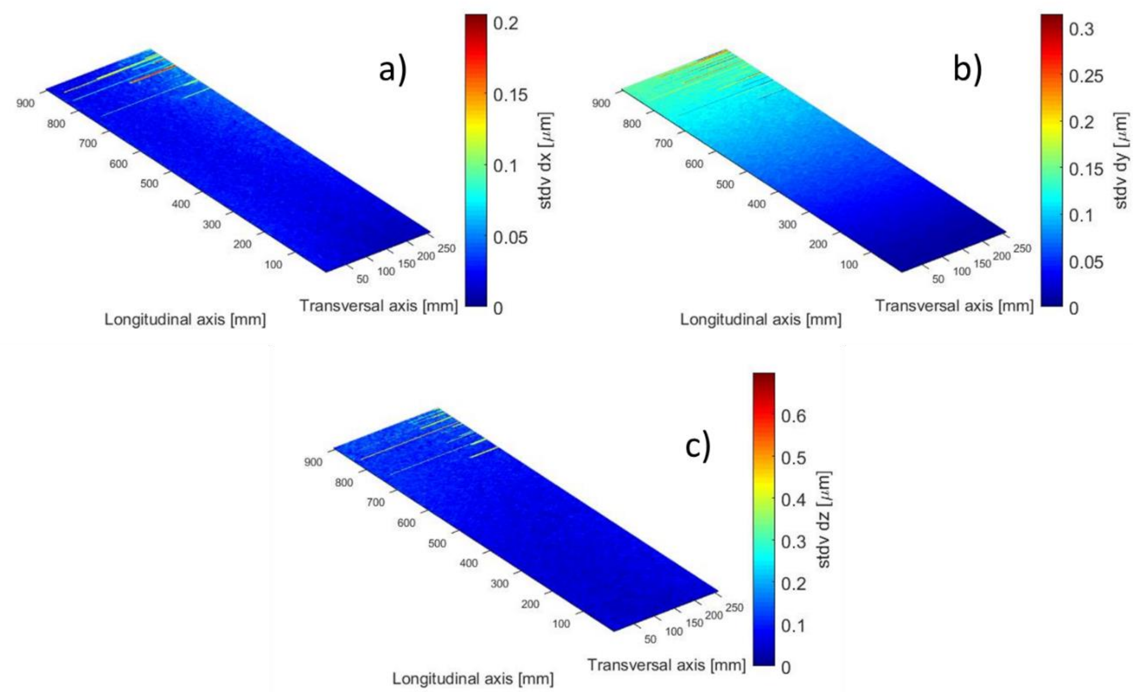

Figure 7-3. (a) Standard deviation for d_x in the combined loading case. (b) Standard deviation of d_y in the combined loading case. (c) Standard deviation of d_z in the combined loading case.

In Chapter 6:, the comparison of the measurement results with those obtained using finite element analysis showed that the out-of-plane component could be measured and reliably and that results agreed well with the simulation/theoretical expectations. The in-plane showed results with bigger errors.

There are two main possible causes for the behavior observed:

- The sample is not behaving in the same way as expected in the simulation. It is likely that effects as friction, imperfect clamping of the beam at the fixed end, misalignments on the spheres used to apply the load, dimensional inaccuracies on the sample could cause such differences in the measurement, that in the worst cases, reached 3µm. Another plausible explanation is that the positioning of the system is not accurate enough and therefore the displacements measured do not compare with the expected simulation results due to the observed region being different than the simulated.
- The calibration process was not sufficient to determine the sensitivity components to the degree of accuracy that is necessary. The calibration sample used depended on many factors such as construction, loading mechanisms and the uncertainties in the measuring devices were high for the application of calibrating an interferometer.

The first assumption was tested by measuring the beam under bending, with the illumination region shifted to the boundary between the beam and the clamp. A perfect clamp would not allow any movement in this boundary, and therefore the phase should not change as a function of load. The measurements showed the contrary. Figure 7-4 shows that the phase is varying with load at the boundary, which indicates the sample is moving inside the clamp, and this may explain the differences in the measurements compared to the finite element simulations.

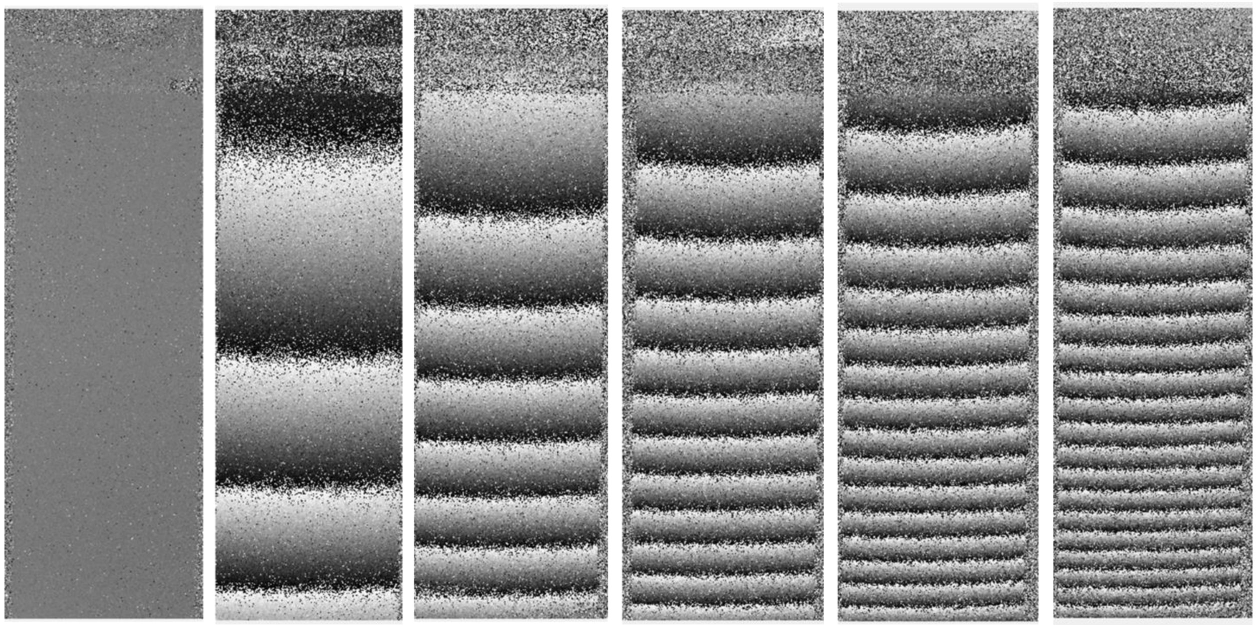

Figure 7-4. Sequence of phase maps representing sequential load steps. On the upper portion, the boundary can be seen. It is possible to notice that the phase at the boundary changes – represented by the change in color - as the load is increased. This characteristic is of a rotation, which means the beam is rotating and moving inside the clamp.

7.2 The laser

One of the most important points of this study is to demonstrate that it possible to obtain high quality measurements using a laser diode as a light source. Furthermore, there are controls that can affect the ability of measuring a good phase map using a laser diode.

- Geometry: by controlling the geometry, the coherence problem that is characteristic of laser diodes is reduced significantly. Both the use of a diffraction grating as a splitting element and the appropriate use of a parallelogram geometry are key factors to eliminate the path length differences in an ESPI interferometer.
- An alternative to improve measurement quality is to maintain control over the temperature and current of the laser. It was demonstrated in Chapter 6:, section 6.2, that even in the presence of the large path length difference in the Y axis, the monitoring and control of the temperature enable the acquisition of high visibility phase maps.

In Chapter 2:, section 2.4, it is stated that diode lasers have very limited coherence due to the existence of several longitudinal modes within their light output. This characteristic has two main consequences: the coherence length is reduced, and at regular intervals, the coherence repeats. It was also demonstrated that by reducing the number of modes that can oscillate within the cavity, the coherence increases but the coherence interval does not. One possible explanation for the effect of temperature control over the laser is that it changes the properties of the gain medium so as to favor one particular mode while inhibiting all others. Changes in the cavity length could also explain such interesting behavior. The temperature ranges for which the laser can operate with high coherence can be found by searching. It was demonstrated in Chapter 6: that the change in coherence is gradual. The same cannot be said about the current, which has a much sharper effect on the coherence.

7.3 Sensitivity Analysis

The system developed has 6 different sensitivity axes. The in-plane axes provide direct measurement of the X and Y displacement components. The remaining axes are on the diagonals, with sensitivity both in X and in Y, and in the out-of-plane direction Z. The sensitivity out-of-plane is very reduced compared to the sensitivity in-plane. As a matter of fact, in a magnitude scale from 0 to 15, the sensitivity in Y is 15, the sensitivity in X is 10 and the sensitivities in the Z direction are of the order of 2. The reason for that is the fact that the out-of-plane sensitivity component derives from the cosine difference of two angles, $\theta_1 = 33.25°$ and $\theta_2 = 52.4°$. The in-plane arrangements depend on the sum of sines of the angles. Furthermore, the out-of-plane sensitivity is fully dependent of the laser wavelength.

Measurements shown on Chapter 6: demonstrated that the system is capable of measuring displacements ranging from a few microns to several microns. More specifically, the out-of-plane arrangements can handle more deformation than the in-plane arrangements due to fringe resolution limits in the more sensitive axes. At high deformations, above 20μm, decorrelation of speckles take’s place and, independent of the sensitivity or number of fringes, the measurement becomes noisy and hard to resolve.

7.4 Noise

It was demonstrated that the main source of noise in an ESPI interferometer is the lack of visibility, which relates directly to the lack of coherence. A second source of noise is related to inaccuracies on the phase stepping. The four-step method, however, is very robust and can handle the phase stepping problem very well. The phase angles should ideally be 90°. The calibration process, however, uses the speckles themselves to determine the voltages necessary for the PZTs to move the gratings. Small vibrations of the environment and natural variations due to the calibration process make the phase to be within 90° $\pm$10°. The four-step method is very robust and can accommodate these variations.

Uneven illumination of the surface is a third factor that contributes to increase the noise levels. In the case of the laser used, the light intensity distribution is elliptical due to the diode's construction. There are some devices that can be used to correct for this effect but were not used in the system to maintain the simplicity. Nonetheless, the uneven illumination showed not to be a major problem of this system.

The geometrical problem that was found in the Y axis can be considered the biggest source of noise if the system is to be used without the appropriate temperature control. Ambient light is also a factor that can contribute to increased noise levels since theoretically, the light adds to the average intensity of the speckle pattern and therefore reduces the visibility – which is the ration of modulated intensity and average intensity. The geometry of the system, however, prevents most of the light from the ambient to reach the surface, and therefore this effect can be neglected.

7.5 Phase stepping

The phase stepping done by translating the diffraction gratings showed to be very convenient. The use of only two PZTs allowed the phase stepping for all the six combinations of sensitivities. In a standard configuration, with 4 PZTs per mirror and with at least 3 PZT equipped mirrors, the number of actuators would have been 12.

The grating stage that was designed showed to be very practical. While holding the two gratings in a compact way it enabled the independent phase stepping with a pure translation mechanism. The single piece construction reduced the number of variables in the phase stepping.

7.6 Suggestions for Future Work

During the design and construction of this equipment, a few issues were found that need to be resolved.

The most important is the geometrical problem found in the Y axis. One way of correcting the problem is to replace the double mirror mount with a parallel mirror mount.

- Correction of geometry: Figure 7-5 shows a parallel mirror geometry that could be used to correct the geometrical problem in the Y axis. The inclined mirrors are replaced with two parallel meirrors to reflect the light three times. The fact that the geometry is parallel eliminates the path length differences and thus ends the problem of coherence bands in the surface. Furthermore, the geometry is also compact when compared to the original concept, exemplified by the dashed lines.

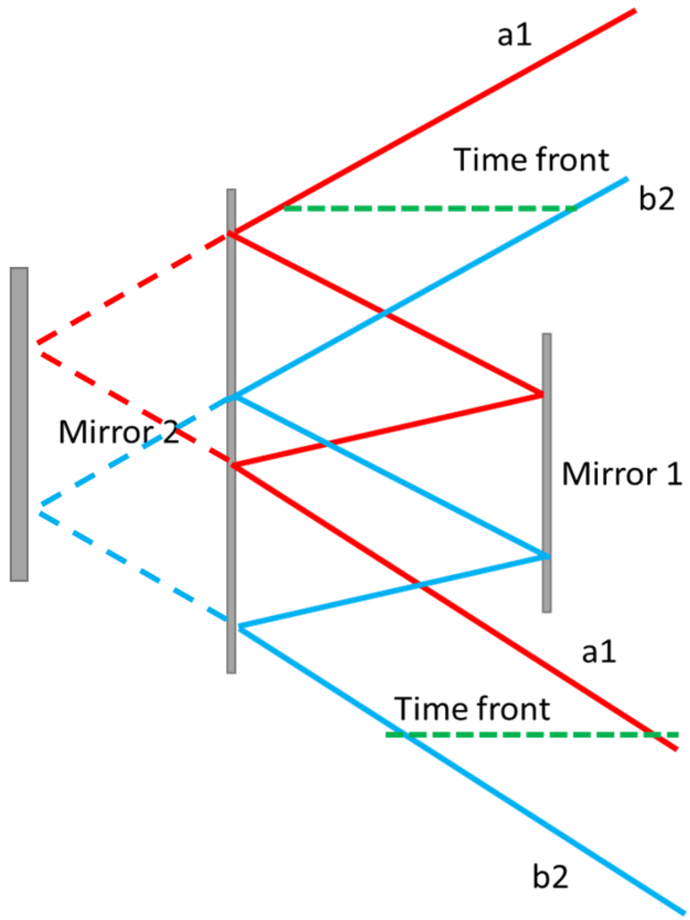

Figure 7-5. Example of parallel geometry that corrects the path length problem while maintain the compactness.

- Better calibration device

As it was stated on Chapter 6, the calibration device used is not ideal. A better calibration device could improve the sensitivity component estimates to give more confidence on the measurement results.

- Improve design for alignment

Mechanical issues with the mirror alignment were also significant problems. The lack of sensitivity in the mirror mounts and the difficulties in the construction have to be addressed in the future. A better design with micrometer screws is desirable for this application. The lens mounts are also a very important factor for the alignment.

- Reduce thermal mass of laser supports

The thermal stability of the laser is well under control, but the laser head system has very big thermal mass. At some times, when the room temperature is too far from the desired operation temperature, it takes a long time for the laser to be ready to operate. A better design would seek to isolate the laser from the lower, bulky aluminum components for a fast and easier temperature control.

- Electrical and electronic improvements

The electrical part also require improvements. The system of shutters demonstrated to be efficient, but the Arduino behavior was not satisfactory. The shutter design showed to be practical, but the connection with the servo motors caused some problems and sometimes the shutters would detach. A better mount is necessary.

- Range of height and sample sizes

The system also has limited rage of height in which it can operate. Part of it is due to the lens with fixed focus. The mirror mount also limits the range of heights and sizes of samples that can be measured.

- Miniaturization

The size of the whole equipment depended on the diffraction grating size and the measurement area requirements. The high sensitivity in the Y direction implies in larger angles, and therefore it takes more space. The camera and lens used also contribute for the overall size of the equipment.

The components were also made larger to facilitate the manufacturing. The manufacturing was performed mainly by the author of this work.

There are opportunities for reducing the size of the equipment and making it more suitable for field work.

- Dynamic loads

Use of a faster camera and investigation on the applications of the multi-axis interferometer for dynamic load measurement. The current configuration is only set for static measurements.

References

[1] R. R. Cordero, M. François, I. Lira, and C. Vial-Edwards, "Whole-field analysis of uniaxial tensile tests by Moiré interferometry," *Opt. Lasers Eng.*, vol. 43, no. 9, pp. 919–936, 2005.

[2] G. S. Schajer and M. Steinzig, "Dual-axis hole-drilling ESPI residual stress measurements," *J. Eng. Mater. Technol.*, vol. 132, no. 1, p. 11007, 2010.

[3] M. R. Viotti, R. Sutério, A. Albertazzi, and G. H. Kaufmann, "Residual stress measurement using a radial in-plane speckle interferometer and laser annealing: Preliminary results," *Opt. Lasers Eng.*, vol. 42, no. 1, pp. 71–84, 2004.

[4] D. Chandra, J. Purbolaksono, Y. Nukman, H. L. Liew, S. Ramesh, and M. Hamdi, "Fatigue crack growth of a corner crack in a square prismatic bar under combined cyclic torsion-tension loading," *Int. J. Fatigue*, vol. 64, pp. 67–73, 2014.

[5] F. Chen, W. D. Luo, M. Dale, A. Petniunas, P. Harwood, and G. M. Brown, "High-speed ESPI and related techniques: Overview and its application in the automotive industry," *Opt. Lasers Eng.*, vol. 40, no. 5–6, pp. 459–485, 2003.

[6] P. Aswendt, C. D. Schmidt, D. Zielke, and S. Schubert, "ESPI solution for non-contacting MEMS-on-wafer testing," *Opt. Lasers Eng.*, vol. 40, no. 5–6, pp. 501–515, 2003.

[7] V. Moreno, C. Vázquez-Vázquez, M. Gallas, and J. Crespo, "Speckle shearing pattern interferometry to assess mechanical strain in the human mandible jaw bone under physiological stress,"*Proc. of SPIE*, vol. 8001, p. 800131, 2011.

[8] R. Shahar, P. Zaslansky, M. Barak, A. A. Friesem, J. D. Currey, and S. Weiner, "Anisotropic Poisson's ratio and compression modulus of cortical bone determined by speckle interferometry," *J. Biomech.*, vol. 40, no. 2, pp. 252–264, 2007.

[9] K. Ramesh, *Digital Photoelasticity: Advanced Techniques and Applications*. Berlin: Springer, 2000.

[10] G. S. Schajer and P. S. Whitehead, “Strain Gages,” in *Pratical Residual Stress Measurement Methods*, G. S. Schajer, Ed. John Wiley & Sons, 2013, pp. 31–32.

[11] B. Han and D. Post, “Geométric Moiré,” in *Handbook of Experimental Solid Mechanics*, Sharpe., W. N. Sharpe, Ed. New York: Springer, 2008, pp. 601–626.

[12] D. Post and B. Han, “Moiré Interferometry,” in *Handbook of Experimental Solid Mechanics*, Sharpe., W. N. Sharpe, Ed. New York: Springer, 2008, pp. 630–652.

[13] D. Gabor, “A New microscopic principle,” *Nature*, vol. 161, no. 4098. pp. 777–778, 1948.

[14] T. Kreis, *Handbook of Holographic Interferometry - Optical and Digital Methods*, 1st ed. Wenheim, Ge: Wiley-VCH, 2005.

[15] J. A. Leendertz, “Interferometric displacement measurement on scattering surfaces utilizing speckle effect,” *J. Phys. E.*, vol. 3, pp. 214–218, 1970.

[16] E. Archbold, J. M. Burch, and A. E. Ennos, “Recording of in-plane surface displacement by double-exposure speckle photography,” *Opt. Acta (Lond).*, vol. 17, no. 12, pp. 883–898, 1970.

[17] K. Creath, “Phase-shifting speckle interferometry,” *App. Opt.*, vol. 24, no. 18, pp. 3053–3058, 1985.

[18] T. Kreis, “2.8 - CCD and CMOS sensors,” in *Handbook of Holographic Interferometry - Optical and Digital Methods*, 1st ed., T. Kreis, Ed. Weinheim: Wiley-VCH, 2005, pp. 65–80.

[19] P. Hariharan, “Two Beam Interferometers: The Mach-Zehnder Interferometry,” in *Basics of Interferometry*, San Diego, 1992, p. 21.

[20] M. R. Viotti, A. G. Albertazzi, and W. Kapp, “Experimental comparison between a portable DSPI device with diffractive optical element and a hole-drilling strain gage combined system,” *Opt. Lasers Eng.*, vol. 46, no. 11, pp. 835–841, 2008.

[21] G. S. Schajer and Y. An, “Residual stress determination using cross-slitting and dual-axis ESPI,” *Exp. Mech.,* Vol. 50, no 1, pp. 169–177, 2010.

[22] Samuel Melamed, “Compact Device for Isotropic Measurements of Residual Stress,” University of British Columbia, 2015.

[23] K. Shibayama and H. Uchiyama, “Measurement of three-dimensional displacements by hologram interferometry,” *App. Opt.,* vol. 10, no. 9, pp 2051-2054, 1971.

[24] A. Martínez, J. A. Rayas, R. Rodríguez-Vera, and H. J. Puga, “Three-dimensional deformation measurement from the combination of in-plane and out-of-plane electronic speckle pattern interferometers,” *App. Opt.*, vol. 43, no. 24, pp. 4652–4658, 2004.

[25] Y. Lianxiang, X. I. E. Xin, Z. H. U. Lianqing, W. U. Sijin, and W. Yonghong, “Review of Electronic Speckle Pattern Interferometry (ESPI) for three-dimensional displacement measurement basic principle of ESPI for displacement measurement,”*Chinese Journal of Mech. Eng.,* vol. 27, no. 1, pp. 1-13, 2014.

[26] B. E. A. Saleh and M. C. Teich, “Electromagnetic Theory of Light,” in *Fundamentals of Photonics*, 2nd ed., B. E. A. Saleh and M. C. Teich, Eds. Hoboken, NJ: John Wiley & Sons, 2007, pp. 150–196.

[27] B. E. A. Saleh and M. C. Teich, “Photon Optics,” in *Fundamentals of Photonics*, 2nd ed., B. E. A. Saleh and M. C. Teich, Eds. Wiley-VCH, 2007, pp. 446–481.

[28] B. E. A. Saleh and M. C. Teich, “Fourier Optics,” in *Fundamentals of Photonics*, 2nd ed., B. E. A. Saleh and M. C. Teich, Eds. Hoboken, NJ: John Wiley & Sons, 2007, pp. 102–149.

[29] Y. I. Nesterets and T. E. Gureyev, “Young ’ s double-slit experiment : noise-resolution duality,” vol. 23, no. 3, pp. 3373–3381, 2015.

[30] C. B. Hitz, J. Ewing, and J. Hecht, *Introduction to Laser technology*, 4th ed. Hoboken, NJ: John Wiley & Sons, 2012.

[31] O. Svelto and D. C. Hanna, *Principles of Lasers*, 5th ed. New York: Springer, 2010.

[32] W. Lauterborn and T. Kurz, “Coherence,” in *Coherent Optics*, 2nd ed., Berlin, 1993, pp. 35–43.

[33] G. S. Schajer, Y. Zhang, and S. Melamed, “In-plane ESPI using an achromatic interferometer with low-coherence laser source,” *Opt. Lasers Eng.*, vol. 67, pp. 116–121, 2015.

[34] J.W.Goodman, “Statistical Properties of Laser Speckle Patterns,” in *Laser Speckle and Related Phenomena*, J. C. Dainty, Ed. New York: Spinger, 1975, pp. 9–75.

[35] M. Steinzig and E. Ponslet, “Residual stress measrement using the hole-drilling method and laser speckle interferometry: Part I,”*Exp. Tech.*, June, pp. 43–46, 2003.

[36] Y. An, Gary S. Schajer, “Pixel quality evaluation and correction procedures in Electronic Speckle Pattern Interferometry,” *Exp. Tech.*, October, pp. 23–29, 2011.

[37] A. Ettemeyer, “Strain measurement by three-dimensional electronic speckle pattern interferometry: potentials, limitations, and applications,” *Opt. Eng.*, vol. 42, no. 5, p. 1257, 2003.

[38] P. J. Georgas and G. S. Schajer, “Modulo-2pi phase determination from individual ESPI images,” *Opt. Lasers Eng.*, vol. 50, no. 8, pp. 1030–1035, 2012.